

Influence of Grain Boundaries and their Composition on the
Deformation Strength of High-purity, Synthetic Forsterite

A DISSERTATION
SUBMITTED TO THE FACULTY OF
UNIVERSITY OF MINNESOTA
BY

Amanda Marie Dillman

IN PARTIAL FULFILLMENT OF THE REQUIREMENTS
FOR THE DEGREE OF
DOCTOR OF PHILOSOPHY

David Kohlstedt

May 2016

Abstract

Grain boundaries are an important feature of the mantle. With recent studies suggesting the majority of the upper mantle deforms by grain boundary sliding (Hirth and Kohlstedt, 2003; Hansen et al., 2013), understanding the role grain boundaries play is key. As grain boundary sliding always requires an accommodation mechanism, directly determining the contribution of grain boundary sliding to total strain on a sample is important for modeling deformation in the mantle. Altering grain boundary composition can change the structure and viscosity of the boundary. Understanding the effects of grain boundary composition is necessary for comparing data sets of different olivine as well as for accurately extrapolating experimental data to represent the mantle.

In Chapter 2, uniaxial deformation experiments on high-purity synthetic forsterite at high temperature and ambient pressure are used to characterize the contribution of grain boundary sliding to strain in diffusion creep. Experiments were conducted in a one-atmosphere deformation rig, which allowed the polished surfaces of the samples to be analyzed with atomic force microscopy. The high temperature necessary for deformation enabled a great deal of thermal grooving, which can dramatically alter the topography of an initially polished surface. A methodology was developed to correct for the effect of thermal grooving and determine the amount of grain boundary sliding as a function of grain size and stress. A comparison is also made between two popular methods for determining grain size: the line intercept method and

the equivalent area circle method. The line intercept method consistently produces larger grain sizes than the equivalent area circle method.

In Chapter 3, triaxial compression experiments on forsterite are used to determine the effect of grain boundary chemistry on deformation strength. High-purity synthetic forsterite was doped with either Ca or Pr and then deformed at high temperature and a confining pressure of 300 MPa. Both impurities made the sample stronger, and the presence of Ca induced abnormal grain growth. This supports the theory that grain boundary composition can have a large effect on deformation strength. The hypothesis that the difference in strength between natural and high-purity synthetic olivines is due to the difference in grain boundary composition is not supported by these results.

In Chapter 4, the results of experiments on forsterite with a small amount of melt are detailed. Two methods of adding melt were used. The first involved adding Pr to forsterite in concentrations greater than can dissolve in the grain boundary, which induced melting as well as enhanced grain growth. Even with a grain size over an order of magnitude greater than the melt-free sample, the melt bearing samples were weaker than the melt free samples. The second method involved synthesizing forsterite with a composition in equilibrium with a synthesized anorthitic melt. Samples were created with melt fractions < 0.01 and then deformed at a temperature of 1300°C and a confining pressure of 300 MPa. The drop in viscosity at very small melt fractions predicted by Takei and Holtzman (2009) was observed, although the drop occurred over

a shorter change in melt fraction than predicted. This result suggests that, at the onset of melting, the mantle will become significantly weaker. In addition, the presence of as little as 0.1% melt in a high purity, synthetic olivine sample brings its deformation strength into agreement with natural samples. This suggests that deformation experiments on natural samples are never entirely melt free.

The results of this study establish the role of grain boundary chemistry on polycrystalline deformation. The presence of large cations in olivine grain boundaries makes diffusion creep slower, which limits the regions of the mantle predicted to deform in diffusion creep and expands the regions predicted to deform in a dislocation accommodated grain boundary sliding or dislocation creep. At the onset of melting, this changes, as the melt would remove the impurities from the grain boundaries. Future studies on different types of impurities will allow the grain boundaries of natural olivines to be more accurately modeled.

Table of Contents

Abstract	i
List of Tables	vi
List of Figures	vii
Chapter 1.	
Introduction	1
1.1 Grain Boundary Structure	2
1.2 Composition of Olivine Grain Boundaries	4
1.3 Melt in Grain Boundaries	5
1.4 Outline of Work in this Study	6
 Chapter 2. The Contribution of Grain Boundary Sliding in Diffusion Creep of Synthetic Forsterite	
Summary	8
2.1 Introduction	9
2.2 Theoretical Background	10
2.3 Methods for Measuring Grain Boundary Sliding	16
2.4 Experimental Procedure	24
2.5 Atomic Force Microscopy Imaging	27
2.6 Development of Analysis Method	31
2.7 Examples of Microstructures	39
2.8 Discussion	43
 Chapter 3. The Effect of Grain Boundary Impurities on the Deformation Strength of Synthetic Forsterite	
Summary	50
3.1 Introduction	51
3.2 Theoretical Background	52
3.3 Sample Preparation	55
3.4 Deformation Experiments	58
3.5 Grain Size Determination	60
3.6 Grain Growth	69
3.7 Normalizing Creep Data to Common Grain Size	74
3.8 Discussion	80
 Chapter 4: The Effect of Small Amounts of Melt on the Deformation Strength of Forsterite	
Summary	98
4.1 Introduction	100
4.2 Theoretical Background	100
4.3 Sample Preparation	108

4.4 Deformation Procedure	112
4.5 Microstructure of Pr Induced Melt Samples	113
4.6 Microstructure of Anorthitic Melt Samples	115
4.7 Microstructure of Pr Induced Melt Samples	117
4.8 Mechanical Data of Anorthitic Melt Samples	121
4.9 Discussion	124
Chapter 5: Future Work	
5.1 Grain Boundary Sliding	130
5.2 Changing Grain Boundary Composition	131
5.3 Melt	132
Bibliography	133

List of Tables

2.1 Vertical correction values for grain surface fitting	42
2.2 Summary of experiment conditions and grain sizes for annealed samples	46
2.3 Summary of experiment conditions, mechanical data, and grain sizes for deformed samples	47
3.1 Summary of mechanical data for undoped Fo	86
3.2 Summary of mechanical data for Ca-doped Fo	88
3.3 Summary of mechanical data for Pr-doped Fo	90
4. 1. Summary of mechanical data for melt bearing Pr-doped Fo samples	119
4.2 Summary of mechanical data for anorthitic melt bearing Fo samples	123
4.3 Fitting constant for anorthitic melt bearing Fo samples	124

List of Figures

2.1 Schematic of grain boundary sliding	18
2.2 Sketch of thermal grooving effect on grain surface topography	19
2.3 Sketch of grain boundary rotation at a grain surface	20
2.4 AFM micrographs pre and post thermal grooving	22
2.5 AFM micrograph of annealed surface scratches	23
2.6 Example of interferometry analysis of grain boundary sliding	24
2.7 AFM images of progressively more thermal grooving	27
2.8 Strain rate vs stress for deformation experiments at one atmosphere	28
2.9 AFM images detailing the image processing necessary	29
2.10 AFM images of annealed and deformed pairs	30
2.11 AFM image and line profiles for an anneal and deformation pair	31
2.12 AFM images showing the effect of thermal grooving on large and small grains	32
2.13 Sketch of line fitting method	35
2.14 Comparison of grain sizes measured by line intercepts and equivalent area circles	38
2.15 Histogram of grain sizes for an annealed sample	39
2.16 AFM image showing grain boundary migration of in large grains	40
2.17 AFM image showing faceted grains	40
2.18 Plot of GBS strain vs total strain for fine grained samples at 60 MPa	44
2.19 Plot of GBS strain vs total strain for large grained samples at 60 MPa	44
2.20 Plot of ξ as a function of grain size	48
2.21 Plot of GBS strain vs total strain for fine grained samples at 1 MPa	48
2.22 Plot of GBS strain vs total strain for all samples > 1 MPa	49
3.1 Comparison of natural and synthetic olivine strength from previous works	53
3.2 Example of transparent, fully dense forsterite	55
3.3 Backscatter image of Pr doped sample with melt phase visible	57
3.4 Example of line intercept grain size method	62
3.5 Example of equivalent area circle grain size method	62
3.6 Comparison of different grain size methods	63
3.7 Example of undoped Fo microstructure	65
3.8 Example of Pr-doped Fo microstructure	66
3.9 Example of Ca-doped Fo microstructure	67
3.10 Log-normal fits to grain size distributions	68
3.11 Example of grain growth effect of Ca-doped Fo mechanical data	71
3.12 Example of two types of abnormally large grains in Ca-doped Fo	73
3.13 Optical micrograph showing one of the largest clusters of abnormally large grains	73
3.14 Grain size distribution pre and post deformation	77
3.15 Comparison of 3 different grain size normalization methods	79

3.16 Strain rate vs stress plots for undoped Fo data	81
3.17 Strain rate vs stress plots for Ca-doped Fo data	82
3.18 Strain rate vs stress plots for Pr-doped Fo data	83
3.19 Comparison of undoped, Ca-doped, and Pr-doped Fo at different temperatures, with different stress exponents	84
3.20 Comparison of undoped, Ca-doped, and Pr-doped Fo at different temperatures, with a singular stress exponent	85
3.21 Arrhenius plot for undoped, Ca-doped, and Pr-doped strain rate data	95
3.22 Schematic detailing the effect slowing diffusion creep has on deformation mechanism transitions	96
3.23 Comparison of natural and synthetic olivine strength including this study	97
4.1 Normalized viscosity vs melt fraction model from Takei and Holtzman (2009)	101
4.2 Comparison of natural and synthetic olivine strength at 1300°C	102
4.3 EDS maps of anorthitic melt pocket and equilibrated Fo	110
4.4 BSE micrograph of Pr-doped sample with 1% melt	113
4.5 BSE micrograph of Pr-doped sample with 0.3% melt	114
4.6 Secondary electron micrograph of sample with 7% anorthitic melt	115
4.7 BSE micrograph of melt pocket in a sample with 1% anorthitic melt	116
4.8 Secondary electron micrographs of samples with 0%, 0.03%, 0.1%, and 0.3% melt	117
4.9 Strain rate vs stress data for sample with 1mol% Pr	120
4.10 Strain rate vs stress data for sample with 0.1mol%Pr	120
4.11 Strain rate vs stress data for samples with anorthitic melt fit with a combined $n = 1$ and $n = 3$ flow law	121
4.12 Strain rate vs stress data for samples with anorthitic melt fit with a combined $n = 1$ and $n = 3$ flow law, scaled to separate the data points	122
4.13 Strain rate vs stress data for samples with anorthitic melt fit with a $n = 2$ flow law	124
4.14 Normalized viscosity vs melt fraction plots for flow law fits with $n = 1, 2, 3$	125
4.15 Viscosity normalized by lowest melt fraction sample vs melt fraction plots for flow law fits with $n = 1, 2, 3$	126
4.16 Comparison of deformation strength of undoped Fo, Ca-doped Fo, Fo in equilibrium with the anorthitic melt, and Fo with 1% melt.	127
4.17 Plot showing agreement between the strength of natural olivine and Fo with a small amount of melt	128

Chapter 1

Introduction

Olivine is the most studied mantle mineral. As it makes up the majority of the upper mantle, understanding its thermal, seismic, and rheological properties is key to understanding mantle dynamics. Many of the experiments on olivine were performed on oriented single crystals, and the data is applied directly to the mantle. A problem with using these data is that single crystals lack a fundamental piece of the mantle: grain boundaries. The presence of grain boundaries does more than simply define a grain size or allow a wide variety of crystallographic orientations in the mantle. Grain boundaries provide sinks for vacancies and dislocations, can accommodate strain by sliding, and are rapid diffusion paths. With recent studies establishing the importance of grain boundaries as storage sites for incompatible elements (Hiraga et al., 2004), the effect of changing grain boundary chemistry needs to be understood. As melting initiates at grain boundaries the presence or removal of the incompatible elements can affect seismic and rheological properties of the mantle at the onset of melting. The experiments in this study are designed to further our understanding of the role grain boundaries play in deformation, and the effect of changing grain boundary composition on that role.

1.1 Grain Boundary Structure

Grain boundaries are interfaces created when bonding two misoriented crystal lattices of the same material together, while interfaces between different materials are known as phase boundaries. Along with multiple grain intersections, known as triple or quadruple junctions, these boundaries are key features of any polycrystalline material. However, the details of the structure of a grain boundary varies by the composition of the boundary as well as the amount of misorientation between the adjacent lattices. For very small misorientations, the boundary between the different lattice orientations can be defined by arrays of dislocations in tilt or twist walls. If the degree of misorientation is slight enough to be described by distinct dislocations, the walls are not considered grain boundaries, but instead sub-grain boundaries. Although the distinction between sub-grain and grain boundaries is not well defined, it is generally accepted that boundaries with between 2° and 10° of misorientation are sub-grain boundaries, and if the misorientation is $> 10^\circ$ then the boundary is a grain boundary (Hansen et al., 2012).

The width of a grain boundary is an important structural feature, which depends on the lattice spacing of the neighboring grains (McLean, 1957). This width can be estimated as equivalent to the width of the core of the dislocations that would make up the grain boundary, $\delta \approx 1-2b$ where b is the Burger's vector (Chang and Graham, 1966). As the storage capacity for incompatible elements is strongly dependent on this width, it

is often assumed to be equivalent to a monolayer of impurities filling the mismatched lattice sites (Hiraga et al., 2004; Baxter et al., 2007).

Measurements of grain boundaries can give very different widths. All grain boundaries are inherently disordered, and so the distinction between a wide grain boundary and a grain boundary containing a melt phase can be hard to find. Grain boundaries in natural olivine often have an 'amorphous film' which is 1-2 nm thick (Wirth, 1995; Drury and FitzGerald, 1996). These natural samples have also been shown to contain a phase in the triple junctions, which rounds the corners of the grains. Natural olivines with no melt added have even been found with amorphous layers 50-500 nm thick (Drury and FitzGerald, 1996). These wider layers, and the material in the triple junctions, is probably a glass/melt phase. The widths are orders of magnitude greater than the largest Burger's vector in olivine, and the rounded triple junctions are a distinctive criterion for melt. However, measurements on high-purity, synthetic olivine, which has absolutely no melt, have grain boundary widths of ~1 nm (Faul et al., 2004). The similarity between this measurement and the thin 'amorphous' layer in natural olivine suggests these layers are not actually an amorphous phase in the grain boundary, but the disordered grain boundary alone. Molecular dynamics simulations on grain boundaries show that, for high energy grain boundaries, a transition to a wide, disordered boundary can occur at temperatures well below the melting temperature (Wolf, 2001).

In addition to storing incompatible elements, the grain boundary width determines the flux of ions moving along the fast diffusion path of the grain boundary. This width is directly expressed in the constitutive equation for Coble creep (Coble, 1963):

$$\dot{\epsilon} \propto \sigma \frac{\delta D_{gb}}{d^3}, \quad (1)$$

where, $\dot{\epsilon}$ is strain rate, σ is stress, d is grain size, D_{gb} is the grain boundary diffusivity of the rate limiting ion, and δ is the width of the grain boundary. Molecular dynamics simulations have suggested that the structural width of the grain boundary is different than the diffusive width, defined as the spread of the atoms in the grain boundary that actually contributes to the diffusive flux (Kebllinski et al., 1999). For olivine, an estimate of grain boundary width was made from diffusion experiments, which resulted in an estimate of 3-5 nm (Farver and Yund, 2000), which is larger than most calculations of the structural width.

1.2 Composition of Olivine Grain Boundaries

Olivine grain boundaries in the Earth may be significant reservoirs for incompatible elements. Geochemical estimates of mantle composition from erupted magmas used to require accessory mineral phases to accommodate all the elements incompatible with olivine (Oxburgh, 1964; Green, 1981). More recent studies show that melt-free grain boundaries can store incompatible elements (Hiraga et al. 2004). Heavy alkali elements, as well as noble gases, likely reside primarily in mantle grain boundaries (Hiraga et al. 2007; Baxter et al. 2007). The concentration of these incompatible

elements strongly depends on grain size, as finer grain sizes have a larger grain boundary to grain volume ratio and thus have a greater storage capacity.

Understanding the effect of varying grain boundary composition on properties such as deformation strength or grain boundary mobility is key to a more accurate modeling of mantle deformation. Experimentally measured olivine compositions have enrichments in Ca, Al in the grain boundaries, with a corresponding depletion in Mg (Hiraga et al., 2004). This depletion indicates that Ca and Al are taking the place of Mg in the grain boundaries. As the majority of incompatible elements likely to reside in mantle grain boundaries are large cations, they will all reside in the available Mg sites of the grain boundary.

1.3 Melt in Grain Boundaries

At the onset of melting, melts are produced primarily in grain boundaries and triple junctions, and initially move along these interfaces (Watson et al., 1991). The incompatible elements sitting on the grain boundaries would be absorbed into this melt and would migrate with it. The melt cannot move solely along triple junctions and grain boundaries for its entire lifetime in the mantle. If melt moved solely through porous flow until right before it erupts, it would quickly equilibrate with the surrounding rock. Since erupted mantle melts are not in equilibria with the residual peridotite, some form of focusing and channelization of the melt is necessary, resulting in locally high melt fractions (Spiegelman and Kenyon, 1992; Aharonov et al., 1995; Kelemen et al., 1997). The vast majority of the melt bearing mantle, however, has < 1% melt (McKenzie, 1989).

Although there have been many deformation studies on partially molten peridotite, the majority of them have had melt fractions between 0.05 and 0.2. A model developed by Takei and Holtzman (2009) predict that in diffusion creep there is a large decrease in viscosity at the onset of melting. Experiments which confirm this model are necessary to accurately predict the strength of the partially molten mantle.

1.4 Outline of Work in this Study

This dissertation investigates the role of grain boundaries on olivine deformation. A key goal is understanding the importance of grain boundary chemistry, which will not only aid in our understanding of deformation in the mantle, but will also help bring laboratory deformation studies of different olivine compositions into agreement. A brief overview of the following chapters is given here.

Chapter 2 details the experiments designed to directly measure the contribution of grain boundary sliding to total strain in diffusion creep. Uniaxial compression experiments were performed on high purity forsterite at a temperature of 1250°C and with no confining pressure. A methodology was developed to use atomic force microscopy images to calculate the amount of strain due to grain boundary sliding from these images. In addition, this chapter compares two popular methods for measuring grain size.

Chapter 3 explains a series of deformation experiments on high purity forsterite, as well as forsterite with Ca or Pr impurities in the grain boundaries. Samples were deformed in diffusion creep at a confining pressure of 300 MPa and temperatures

between 1000°C and 1250°C. The effect of changing grain boundary chemistry on deformation strength in diffusion creep is detailed, as well as the effect on grain growth kinetics.

Chapter 4 builds on the results of Chapter 3, by changing the composition of the grain boundaries in forsterite to include a melt phase. We test the theory put forth by Takei and Holtzman (2009), which predicts a large change in viscosity with the addition of very small amounts of melt to initially melt free samples. Small amounts of melt (<1%) were created in triple junctions, then triaxial deformation experiments were performed on the samples at a temperature of 1300°C and a confining pressure of 300 MPa. The difference in deformation strength between natural olivines and high-purity synthetic olivines is accounted for with the addition of very small amounts of melt.

Chapter 5 summarizes the results of the previous chapters and suggests future avenues of inquiry into the role of grain boundaries in the deformation of olivine in the mantle and in lab experiments.

Chapter 2: The Contribution of Grain Boundary Sliding in Diffusion Creep of Synthetic Forsterite

Summary

High purity, synthetic forsterite was deformed at 1250°C and a confining pressure of 0.1 MPa in order to quantify the amount of grain boundary sliding strain in the diffusion creep regime. Uniaxial compression experiments with differential stresses of 1-125 MPa were performed on samples cut into right prisms, with at least one face polished flat. This face, oriented parallel to the applied stress, was imaged using atomic force microscopy after deformation. The amount of strain due to grain boundary sliding was determined using high resolution measurements of topography. A methodology was developed to account for thermal grooving of the polished face and to objectively quantify the ratio of grain boundary sliding strain to total strain, ξ . For the differential stresses applied, $\xi = 63\%$. This ratio was found to be independent of strain and to decrease slightly with increasing grain size. Its value, 63%, agrees with experimentally determined values of ξ for pure, fine grained alumina, but is lower than the value obtained for two-phase alumina-zirconia samples, indicating that a study of phase boundaries may be necessary to apply these results to the Earth. Attempts to deform samples at higher stresses in order to extend our results into the dislocation-accommodated grain boundary sliding regime proved impossible because the samples fractured.

2.1 Introduction

Grain boundary sliding (GBS) is a deformation process that requires either diffusion or dislocation motion in order to maintain fully dense samples and deform at a steady-state strain rate. When accommodated by diffusion (diffusion creep), this deformation is characterized by a Newtonian viscosity with a strong dependence on grain size. In contrast, strain rate in the dislocation accommodated grain boundary sliding (disGBS) regime has a stronger dependence on stress and a weaker dependence on grain size. Grain boundary sliding as part of a deformation mechanism is thought to dominate rheological behavior throughout a large portion of the upper mantle.

To better understand this deformation mechanism, explicit measurements on the contribution of GBS to total strain are necessary. There are several different methods for measuring the strain due to GBS, all of which are easier to use on samples deformed at ambient pressure than at pressures representative of plastic deformation regions in the Earth. For olivine, deformation at ambient pressure requires a fine grain size, or the thermal expansion anisotropy would cause the samples to crack. These small grain sized samples of olivine deform in diffusion creep, a mechanism that has the stronger dependence of strain rate on grain size than disGBS. High purity, synthetic forsterite was chosen to study the contribution of GBS, as it can be created with a grain size of $\sim 1 \mu\text{m}$ and its relatively sluggish grain growth kinetics limit the grain size to generally less than $10 \mu\text{m}$.

Of all the methods developed on metals and ceramics for measuring GBS, atomic force microscopy (AFM) was the most reliable for our samples. A new method for analyzing this AFM data was necessary, however, as the high temperature necessary to deform olivine induces a large amount of thermal grooving. Thermal grooving alters the initial planar surfaces of the grains, creating valleys above grain boundaries and hills directly adjacent to the boundaries. We adapt the AFM methodology of Clarisse et al. (1999) to account for this grooving, and utilize the equations laid out in Langdon (1994) to calculate strain from the vertical displacements of grains.

Characterizing the contribution of GBS to the total strain of a sample can help to distinguish between different deformation mechanisms. Separating diffusion and GBS in diffusion creep is a bit illogical, as diffusion creep requires both. Working in the diffusion creep field is useful for developing the methodology for calculating strain due to GBS, which can then be applied to disGBS and dislocation creep of olivine. Understanding how much grain boundary sliding occurs in these creep regimes can aid in the interpretation of textures of experimentally deformed samples as well as those of naturally occurring peridotites.

2.2 Theoretical Background

Grain boundary sliding (GBS) is a polycrystalline deformation process that requires an accommodation mechanism. Although a bicrystal with a perfectly planar grain boundary could, in theory, activate GBS alone, most boundaries have small irregularities that limit the rate of GBS by requiring an accommodation mechanism. For

small strains and small irregularities, GBS can be accommodated elastically. For higher strains or larger imperfections, diffusion along grain boundaries can relax the stress concentrations along the grain boundaries and permit GBS. Raj and Ashby (1971) first laid out a theoretical framework for describing the rate GBS accommodated by diffusion. Rapid diffusion along grain boundaries or high diffusive flux through the lattice allow normal stresses generated by GBS along boundaries or at triple junctions to be relaxed (Beere, 1978; Raj and Ashby, 1971). At very high stresses, accommodation by dislocation motion replaces diffusion as the dominant process facilitating continued sliding on grain boundaries.

These different accommodation mechanisms define three different regimes for grain boundary sliding. Elastically accommodated grain boundary sliding (EAGBS) is of interest in seismic attenuation studies and plays a role as part of initial transients in creep experiments. Grain boundary sliding is a fundamental part of diffusion creep when accommodated by diffusion. This creep regime, also known as Lifshitz sliding (Lifshitz, 1963), dominates at low stresses and fine grain sizes. Dislocation-accommodated grain boundary sliding, also known as Rachinger sliding (Rachinger, 1959), has two sub-regimes which have different dependencies on grain size. These regimes are distinguished by whether the grain size is smaller or larger than the sub-grain size, but both are considered to be Rachinger sliding (Langdon, 1994, 2006). Rachinger sliding is often called disGBS in more recent earth science literature (Warren and Hirth, 2006). In addition to these mechanisms, GBS can also occur as an

accommodation mechanism during dislocation creep, in which strain rate is independent of grain size. Although not necessary for dislocation creep, grain boundary sliding is often invoked to relax the von Mises criterion (von Mises, 1913) for olivine, as it lacks the required 5 independent slip systems required for homogeneous plastic deformation.

There are several criteria for determining the dominant deformation mechanism. For a mechanism involving GBS, these criteria are often associated with those of superplasticity, which has been used to indicate the Ratchinger sliding mechanism (Clarisse et al., 1999). Although this term has been used rather liberally, superplasticity is not a deformation mechanism. Rather, it is a phenomenon characterized by elongation of a sample to a strain of $\epsilon \geq 1000\%$ without necking or failure (Schmid et al., 1977; Hiraga et al. 2010). Superplasticity is often observed in metals or metallic alloys and occasionally in ceramics (Kim et al., 2001; Hiraga et al. 2010). Attempts to determine whether deformation was superplastic in natural samples by examining post-deformation microstructures led to the creation of several criteria: fine grain size, moderate stresses and strain rates, high temperature, no crystallographic preferred orientation (CPO), and low dislocation density with little to no subgrain structures (Boullier and Gueguen, 1975). Some of these criteria have been relaxed by more recent experiments. For example, recent studies have determined that it is possible for dislocation-accommodated GBS to produce a CPO (Hansen et al., 2011; Precigout and Hirth, 2014). All of these criteria are fulfilled by some shear zone mylonites (Boullier &

Gueguen, 1975; Warren and Hirth, 2006). However, it has been proposed that it is possible to create a mylonite texture without GBS being the dominant deformation mechanism (Fliervoet and White, 1995), based on textures observed in a quartz shear zone. While these criteria are necessary for GBS, they are not sufficient to determine that deformation involved grain boundary sliding (Clarisse et al. 1999).

Although different textures and deformation conditions can be used to infer deformation mechanism, the definitive way to distinguish among deformation mechanisms is through analysis of mechanical creep data (McNee et al., 2001). Creep data are generally fit to a flow law of the form

$$\dot{\epsilon} \propto \frac{\sigma^n}{d^p}, \quad (1)$$

where $\dot{\epsilon}$, strain rate, is dependent on stress, σ , to a stress exponent, n , and inversely dependent on grain size, d , to a grain size exponent, p . Previous studies on natural samples often overlooked grain boundary sliding, and all mechanical data with $n > 2$ was often assigned to dislocation creep (Hirth & Kohlstedt, 1995). Now, mechanical data with $n > 2$ can be split into a regime involving GBS and a dislocation creep regime. For Ratchinger sliding (i.e., disGBS), if the grain size of the deformed sample is smaller than the subgrain size, values of $n = 2$ and $p = 2$ are predicted. If the grain size is larger than the subgrain size, values of $n = 3$ and $p = 1$ are predicted (Langdon, 1994, 2006). For grains larger than the subgrain size, the activation energy for grain boundary sliding is expected to be that of the lattice diffusivity of the rate limiting species, while the activation energy should equal that of grain boundary diffusivity of the rate limiting

species for samples with grains smaller than the subgrain size (Langdon, 1994). These predicted values of stress exponent, grain size exponent, and activation energy allow one to determine the deformation mechanism active during a creep experiment.

Deformation experiments performed on olivine (Hirth and Kohlstedt, 1995; Hansen et al., 2011), ice (Goldsby & Kohlstedt, 2001), and quartz (Etheridge and Wilkie, 1979) have illustrated deformation dominated by disGBS. Recent studies argued for expanding the role of grain boundary sliding in olivine, making it a dominant mechanism of deformation in the uppermost part of the mantle (Hirth and Kohlstedt, 1995; Hansen et al., 2011, Hirth & Kohlstedt, 2003).

There is some ambiguity as to the meaning of these values for stress and grain size exponent. The values for stress and grain size exponent can also be created by a mixture of pure dislocation creep, with $n > 3$ and $p = 0$, and pure diffusion creep, with $n = 1$ and $p = 2$ or 3 (Nabarro, 1948; Herring, 1949; Coble, 1963; Raj and Ashby, 1971). A broad grain size distribution blurs the transition between diffusion and dislocation creep, making this mixture of deformation mechanisms occur over a larger range of stress and strain rate than predicted by models using a uniform grain size (Ghosh and Raj, 1981). Ice is an exception to this argument of a GBS regime being a mixture of diffusion and dislocation creep. The regime associated with 'superplasticity' in ice, with $n = 1.8$ cannot be an artifact of mixing adjacent regimes, as it is sandwiched in strain rate-stress space between basal slip, $n = 2.4$, and dislocation creep, $n = 4$.

Grain boundary sliding is also accommodated by diffusion (Lifshitz sliding).

Although some studies have distinguished between grain boundary sliding accommodated by diffusion and sliding during diffusion creep (Ashby and Verrall, 1973), we make no such distinction here. Diffusion accommodated grain boundary sliding will often experience an initial transient creep. This transient creep, which can initially be 50 times faster than steady state deformation, is likely due to elastically accommodated GBS, and the transition to Lifshitz sliding requires an increase in the density of grain boundary dislocations (Raj, 1975). Motion of these grain boundary dislocations induces sliding. As grain boundaries are often considered to be perfect sinks and sources for vacancies, motion of these vacancies into and out of the grain boundaries allow climb of these dislocations (Ashby, 1972). Anything that impedes the motion of boundary dislocations, impedes the motion of vacancies and thus slows diffusion creep. Lifshitz sliding affects the texture of deformed samples as well. Theoretical models based on Nabarro-Herring or Coble creep often predict elongation of grains during deformation. Grain boundary sliding allows switching of grain neighboring grains and rotation of grains, which effectively keeps grains relatively equiaxed (Ashby and Verrall, 1973).

Diffusion creep requires grain boundary sliding to avoid opening gaps at grain boundaries (Lifshitz, 1963; Raj and Ashby, 1971). This interdependency makes determining the individual contributions of sliding and diffusion to strain a bit questionable, as without both there would be no strain. Since it is possible for each to create strain, various attempts have been made to distinguish the strain produced by

each mechanism. Kim and Hiraga (2000), using a model made of spherical grains, predicted that roughly 60% of the strain of diffusion creep is due to GBS. Sahay and Murty (2001), using a model of hexagonal grains, predicted the majority of the strain was due to diffusion. As their hexagonal grains elongated, the contribution of diffusion increased with strain, until over 90% of the strain was associated with diffusion. Direct measurements of the proportion of strain accomplished by diffusion versus that achieved by grain boundary sliding have been performed for a number of metals (Bell et al., 1967; Gates and Stevens, 1974; Gifkins, 1977; McNee et al., 2001; Kottada and Chokshi, 2007) and ceramics (Clarisse et al. 1999, 2000), but not for olivine.

2.3 Methods for Measuring Grain Boundary Sliding

To separate strain produced in the diffusion creep regime into strain due to diffusion and that due to grain boundary sliding, direct measurements of strain are necessary. These measures of grain boundary sliding can be made on analogue materials that permit deformation to be viewed as it is happening (Ree, 1994). Scribed lines on the surface of a sample prior to deformation can also be used to measure the amount of grain boundary sliding. After deformation, offsets of these lines can be used to calculate GBS strain. Offsets near a grain boundary provide a measure of the strain due to grain boundary sliding. This method is most effective for larger grained samples, such as in metals (Gifkins, 1977), while a significant amount of GBS only occurs in ceramics with a relatively fine grain size (Kim et al. 2001, Warren and Hirth, 2006).

Interferrometry is also useful for measuring grain boundary sliding, but loses its effectiveness for very small grains (Clarisse et al. 1999, Langdon, 2006).

A measurement of strain due to GBS on the surface of a rock will not necessarily represent the strain due to GBS in the interior. In contrast to sliding in the plane of the surface or the interior of a rock, it is easier for grains to slide normal to the surface, as there are no grains in the way. To correct measurements of strain due to GBS at the surface to represent the interior, various equations have been developed (Langdon, 1972). Using these equations, several studies have shown excellent agreement between strain due to sliding measured on the surface and in the interior of samples, within the error of the measurements (Bell et al. 1967; Gates and Stevens, 1974).

Langdon (1994) proposed the following expression for estimating the contribution of grain boundary sliding to the total strain, ε_t :

$$\varepsilon_t = \varepsilon_g + \varepsilon_{gbs} + \varepsilon_{dc} \quad (2)$$

where ε_t is the total strain, ε_g is the strain due to intragranular dislocation processes, ε_{gbs} is the contribution of Ratchinger GBS (dislocation-accommodated grain boundary sliding), and ε_{dc} is the strain due to Lifshitz GBS (diffusion creep). In our experiments, direct measurement of the GBS contribution to diffusion creep is the desired goal; therefore, our experiments were designed such that $\varepsilon_t = \varepsilon_{dc}$. We redefine the total strain to represent processes, rather than mechanisms:

$$\varepsilon_t = \varepsilon_{dis} + \varepsilon_{GBS} + \varepsilon_{diff}, \quad (3)$$

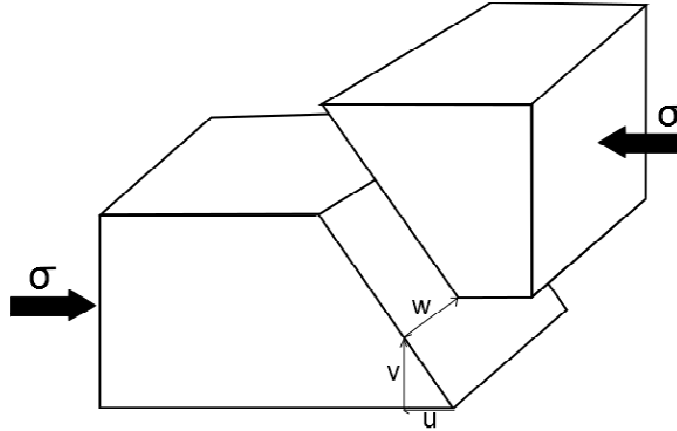


Figure 1. Schematic diagram illustrating sliding of two blocks (grains) along their shared grain boundary.

where ϵ_{dis} is the strain due to dislocation motion, ϵ_{GBS} is the strain due to the sliding of grains, and ϵ_{diff} is the strain due to diffusion. The contribution of GBS to total strain, ξ , is thus

$$\xi = \frac{\epsilon_{GBS}}{\epsilon_t} \quad (4)$$

To order to quantify ϵ_{GBS} , Langdon (1994) defined three orthogonal intergranular displacement measurements. The schematic in Figure 1 defines these displacements: v , normal to the surface, u , parallel to σ_1 in the plane of the surface, and w , perpendicular to σ_1 in the plane of the surface. It is sometimes difficult to measure all of these displacements, but grain boundary sliding strain can be calculated from a single one of these parameters (Gates and Stevens, 1974). Displacements normal to the surface translate to GBS strain as

$$\epsilon_{GBS} = k'' n_r \bar{v}_r \quad (5)$$

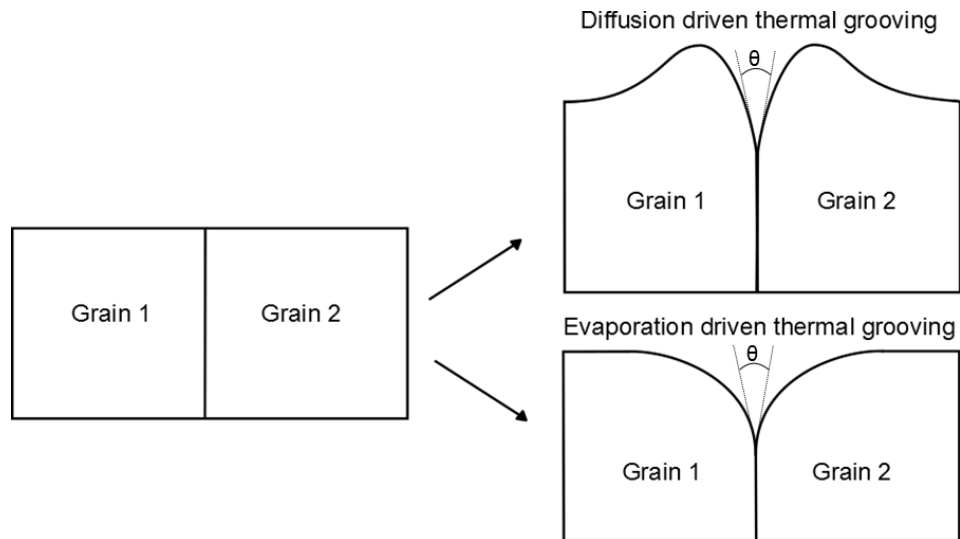
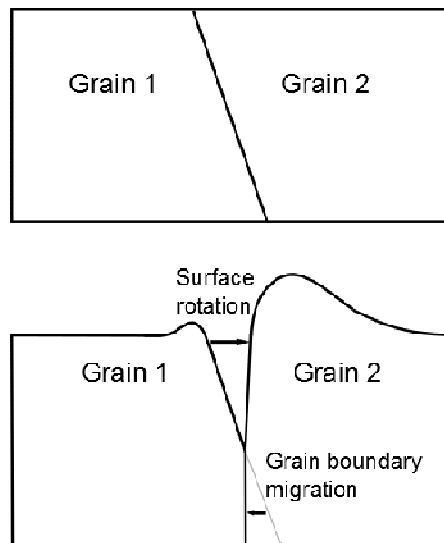


Figure 2. Sketch of the different two types of profiles that can be produced across a grain boundary by thermal grooving. The dihedral angle (θ) at the grain boundary is the same in both cases.

where k'' is a constant which corrects measurements on the surface to represent the interior and n_g is the number of grains per unit length. The average vertical displacement between grains, \bar{v}_g , is defined as the sum of all the displacements between adjacent grains divided by the total number of grains, with the subscript r denotes measurements taken across random grain boundaries. For a freshly cut surface, k'' is ~ 1.1 , as grain boundaries intersect the surface at random angles. As a surface anneals, grain boundaries near the surface rotate until they are perpendicular to the surface, which increases k'' to ~ 1.4 (Langdon, 1971). Langdon (2006) determined k'' to be a geometrical constant, while Gates and Stevens (1974) suggest it to be a material constant and Gifkins (1977) found a slight time dependence to it. For forsterite, as little as 10 min at the deformation temperature is enough to thermally groove the sample surfaces; thus, all surfaces are treated as annealed, and a constant value 1.4 was used.

Grain boundaries in polycrystalline material exposed at a polished surface

thermally groove at elevated temperatures (Mullins 1957). Thermal grooving removes part of a grain boundary and forms a valley opening above the remaining portion of the grain boundary. The width and depth of this valley is a function of the energy balance of the system and time. The balance of grain boundary energy and surface tension of the adjacent grains establishes the dihedral angle, the opening angle at the bottom of the valley. Material diffuses onto the adjacent grains and, as time progresses, diffusion and evaporation redistribute this mass, flattening the ridge. If diffusion dominates, material piled onto the surface of the grain directly adjacent to the boundary is moved further away from the boundary, as demonstrated in the sketch in Figure 2. This motion changes the dihedral angle, which induces additional grooving (Mullins, 1957). This ongoing process means that, as time progresses, the valley between grains grows deeper and the 'hill' of material evolves from a sharp ridge to a gentler curve. For small



grains, hills from different sides of the same grain meet and grow together, creating downward curvature everywhere. If evaporation is the dominant process for relocating

Figure 3. Sketch of the effect of thermal grooving on a grain boundary that intersects the surface at a non-90° angle.

material from the grain boundary, the material from the hill is removed to the atmosphere, which induces more grooving. The balance of surface tension and grain boundary energy produces a torque that also rotates grain boundaries near the surface (Kelly & Groves, 1970, p.356-357; Langdon 2006) to an orientation normal to the surface. This process can occur by grain boundary migration beneath the surface or by enhanced diffusion of material from the overlying grain. This enhanced diffusion causes more material to build up on one edge of a grain, resulting in apparent grain rotation in annealed samples, as illustrated in the sketch in Figure 3.

Mullins (1957) laid out a series of equations that describe the kinetics of grooving of a grain boundary due to surface diffusion or evaporation. Once the dihedral angle is established by moving material from the grain boundary onto adjacent grains, ridges begin to evolve. Surface diffusion migrates the material further away from the grain boundary, and evaporation removes material from the ridge into the atmosphere, due to the curvature of the ridge. To determine which mechanism dominates, Mullins created the dimensionless ratio

$$R = 0.38 \frac{(2Y D_s n M)^{0.5}}{P_0 \Omega \gamma^{0.5}} t^{-0.5}, \quad (6)$$

where Y is the number of atoms/area, D_s is the surface diffusion coefficient, M is the mass of a molecule, P_0 is the vapor pressure in equilibrium with a plane, Ω is the molecular volume, γ is the surface energy per area, and t is time in seconds. Mullins suggested that surface diffusion dominates if $R \geq 100$. To calculate R for olivine, we used values of $Y = 2.5 \times 10^{19} \text{ m}^{-2}$ (Gillet et al. 1991), $M = 2.3 \times 10^{-22} \text{ g}$, $\rho_0 = 9.4 \times 10^{-5} \text{ Pa}$

(Nagahara et al. 1994), $\Omega = 2.91 \times 10^{-28} \text{ m}^3$ (Gillet et al. 1991), and $\gamma = 1 \text{ J m}^{-2}$ (Swain & Atkinson). Instead of the surface diffusion coefficient of Si in olivine, the volume diffusion coefficient of $D_s \approx 2 \times 10^{-21} \text{ m}^2 \text{ s}^{-1}$ (Fei et al. 2012) was used. In general, surface diffusion coefficients are at least > 4 orders of magnitude greater than those for volume diffusion (Johnson, 1969), so using the volume diffusion coefficient provides a strong lower limit to the amount of time necessary for evaporation to affect the profile of a forsterite sample. With these values, a value of $R \approx 5 \times 10^5 t^{-0.5}$ is calculated, and a time of roughly 100 h at 1250°C is estimated as required before evaporation starts to become effective. This time jumps to > 100 years if one increases the diffusion coefficient by 4 orders of magnitude to approximate surface diffusion. For the calculations done in this study, it is therefore assumed that no mass evaporation occurs and that the surface and boundary energies are isotropic throughout the sample.

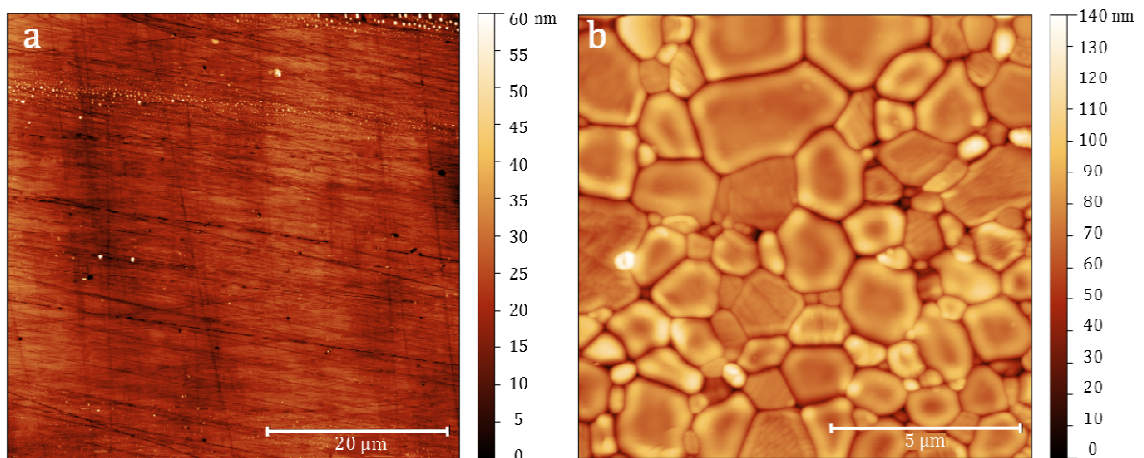


Figure 4. a) AFM image of polished surface of a sample prior to thermal grooving. b) AFM image of surface of sample thermally grooved for < 5 min. The color scale indicates height of surface topography.

The effect of thermal grooving on surface topography and grain boundary visibility is illustrated in Figure 4. In the atomic force microscopy (AFM) image in Figure 4a of a polished but not heated sample, a number of scratches are visible, but no grain boundaries. The AFM image in Figure 4b is of a sample that was heated to the deformation temperature at a rate of 300°C/h and then immediately cooled at the same rate. The scratches have almost completely disappeared, while the grain boundaries have grooved and are clearly visible. Note that the height range is a factor of ~ 2 greater than in Figure 4b than in Figure 4a.

There are several different methods for measuring grain boundary sliding, but not all of them are applicable to this study on forsterite. The relative ease with which scratches are removed by annealing in some forsterite grains and not others, makes the line scribing method unreliable. An example of a scratch that only partially survived

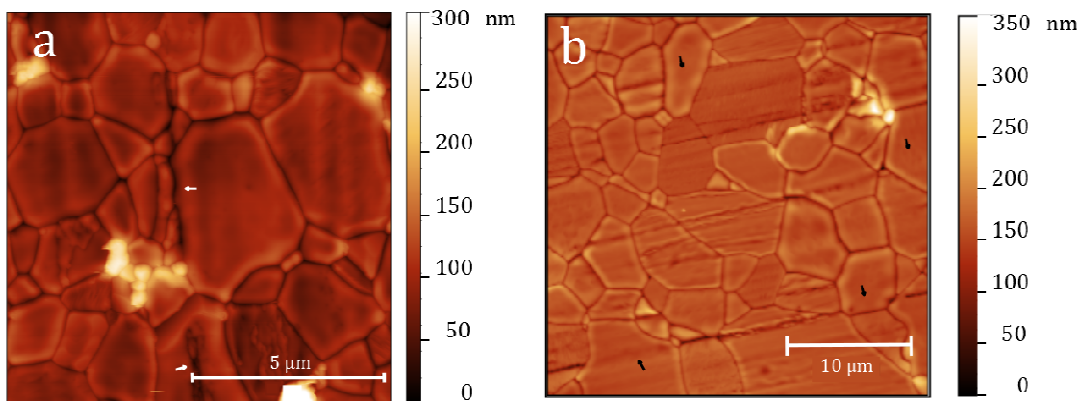


Figure 5. a) AFM image of deformed Sample 6-1. White arrows point to a scratch that is indistinguishable from the grain boundaries. The scratch was nearly vertical and crossed the sample in the middle of the image. b) AFM image of annealed Sample 16-1. Polishing scratches created roughly parallel lines across this image. Black arrows indicate where the scratches were almost entirely removed during annealing of some grains, while adjacent grains still show the scratches.

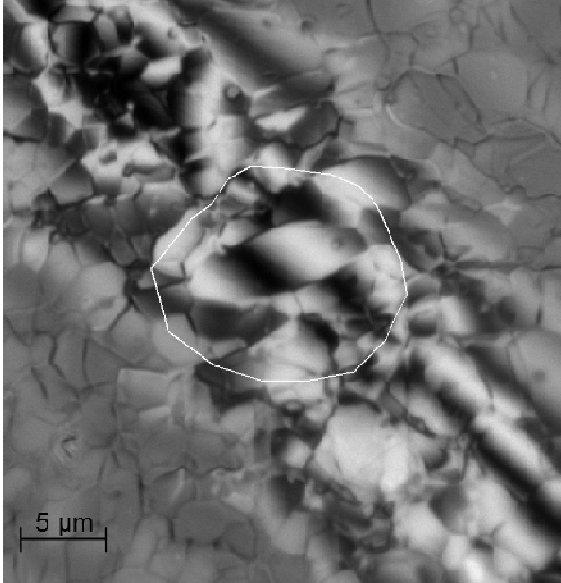


Figure 6. Interferogram from Sample RN1 demonstrating displacement at a grain boundary. The breaks in the central black stripe indicates changes in topography. The large grain in the center of the circle shows a clear break of this line at each of the grain boundaries. The grains at the lower end of the circle do not show a clear placement or width of the black stripe and thus cannot be analyzed.

annealing is shown in Figure 5. The scratch in Figure 5a became almost indistinguishable from a series of grain boundaries, and the scratch almost completely disappeared, while neighboring grains retain the scratch. Interferometry is a popular method for measuring vertical grain boundary sliding, but the measurement error for small strains and small grain sizes can be large (Clarisse et al., 1999). Vertical sliding of grains creates variations in relative height of the grains on the nanometer scale for fine-grained samples. The example of sliding at a grain boundary in forsterite presented in Figure 6 demonstrates the interference fringes. More precise characterization requires the use of atomic force microscopy (AFM), which in contact mode has an error of <10 nm in lateral measurements and <1 nm in vertical measurements (Haugstad, 2012.)

2.4 Experimental Procedure

Samples were prepared from high-purity, synthetic forsterite (Mg_2SiO_4) powder with an average particle size of <1 μm (Hiraga et al. 2010). This powder were uniaxially

pressed into cylindrical dies, removed from the dies, and then isostatically cold-pressed at >100 MPa. The cylindrical green bodies were vacuum sintered for 5 h at 1400°C . The average grain sizes of the resulting dense samples were <10 μm . These cylinders were then quartered along the long axis. One long face of each quarter was polished with diamond lapping film down to a grit of 0.5 μm . This polish ensured an initially flat surface, as shown in Figure 2a. The ends of the quarters were ground flat and parallel. One quarter from each cylinder was cut into three smaller pieces, each of which was paired with one of the remaining quarters. These anneal chips were placed beside the quarters during the deformation experiments, in order to determine the effects of time and temperature on surface topography.

To minimize cavitation during the deformation tests, samples with grain sizes of <10 μm were used. A sample with this fine a grain size is able to elastically accommodate strains due to thermal expansion anisotropy (Cooper, 1990; Evans, 1978). One sample that was annealed for a series of longer time steps than the deformation samples exhibited deep pits. The time sequence of AFM images in Figure 7 for this sample show an evolution from tight grain boundaries to a more open structure. These pits could be due to extensive thermal grooving, but cavitation cannot be ruled out. However, openings at the surface do not strongly develop until multiple days at temperature have passed. All deformation experiments were completed in less time than the sample which showed open pits at the surface.

Deformation experiments were carried out on the quarters in uniaxial compression in a one atmosphere furnace at 1250°C. Inside the furnace, the sample was sandwiched between Zr₂O₃ platens on SiC pistons. During deformation, two direct current displacement transducers (DCDT) measured the displacement of the sample. One DCDT used SiC extension rods for thermally compensated displacement measurements inside the furnace, while the second measured motion of the deformation column externally. Fine-grained forsterite, under low-stress, high-temperature conditions, deforms by diffusion creep, as evidenced by the stress exponent of $n \approx 1$ in Figure 8. We established a methodology that quantifies grain boundary sliding in diffusion creep, which can be applied to dislocation-accommodated grain boundary sliding creep which is anticipated to occur at higher stresses.

2.5 Atomic Force Microscopy Imaging

The atomic force microscopy images were taken in contact mode, meaning the cantilever tip was placed in 'contact' with the surface of the forsterite and rastered back and forth. A piezoelectric motor moves the sample up and down to keep the deflection of the cantilever constant. To have multiple grains in each image, the size of an image was often close to the mechanical limit of the piezoelectric motor to scan. These large images push the piezoelectric motor into non-linear motions, creating anomalous height differences. The unprocessed image in Figure 9a seems to be highly tilted, but removal of the polynomial background of Figure 9b creates the flattened image of Figure 9c. The

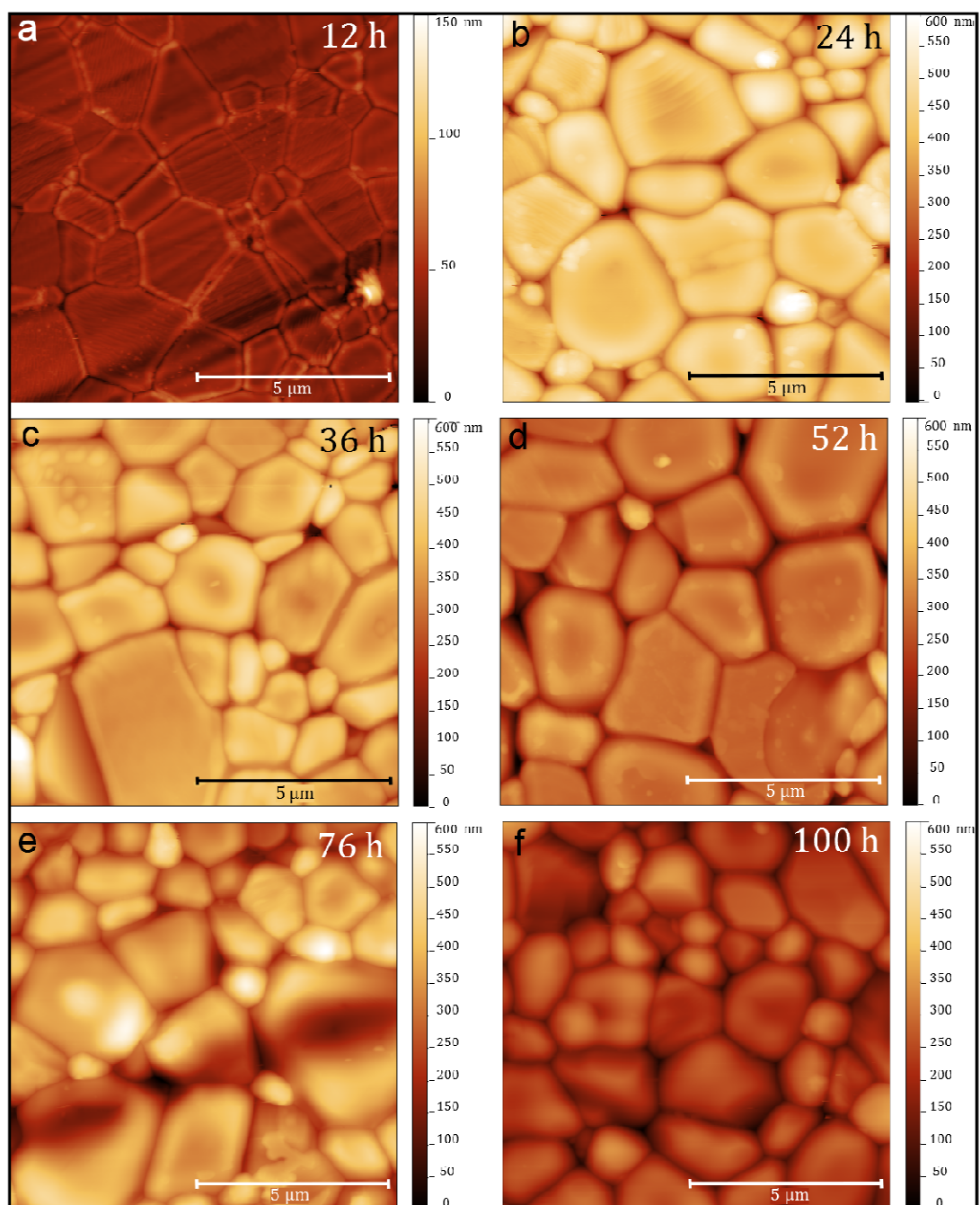


Figure 7. AFM images illustrating the time evolution of thermal grooving of Samples 3-1 through 3-6 in a) through f), respectively. a) 12 h, b) 24 h, c) 36 h, d) 52 h, e) 76 h, f) 100 h at 1250°C. Image a) shows closed grain boundaries. As time increases triple junctions get wider and pits start to open at the surface.

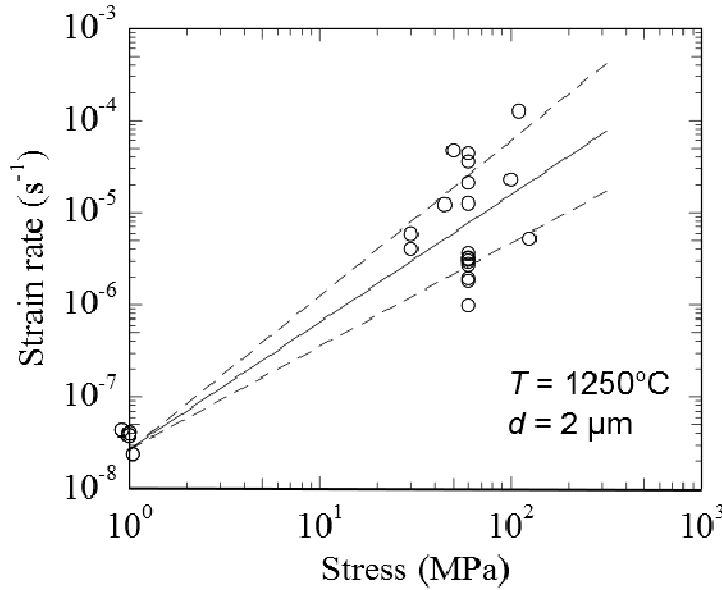


Figure 8. Strain rate as a function of stress from all twenty experiments. A linear least squares fit yields a stress exponent of $n = 1.3 \pm 0.3$.

shape of the background to be removed is dependent on relative position of the cantilever, so an xy polynomial fit was used for the subtraction step. Occasional raster lines are flawed, creating the bright horizontal lines in Figure 9c. These line spikes are ameliorated by replacing them with the average of the lines on either side. This processing does not affect the height of individual grains.

Images of deformed samples exhibit a wider range of heights than those of annealed samples, as can be seen comparing the images of the paired anneal chips in the right hand column to those from the associated deformed sample in the left hand column in Figure 10. The range of heights in the deformed sample increases with increasing strain more than the range increases due to thermal grooving (annealing) alone.

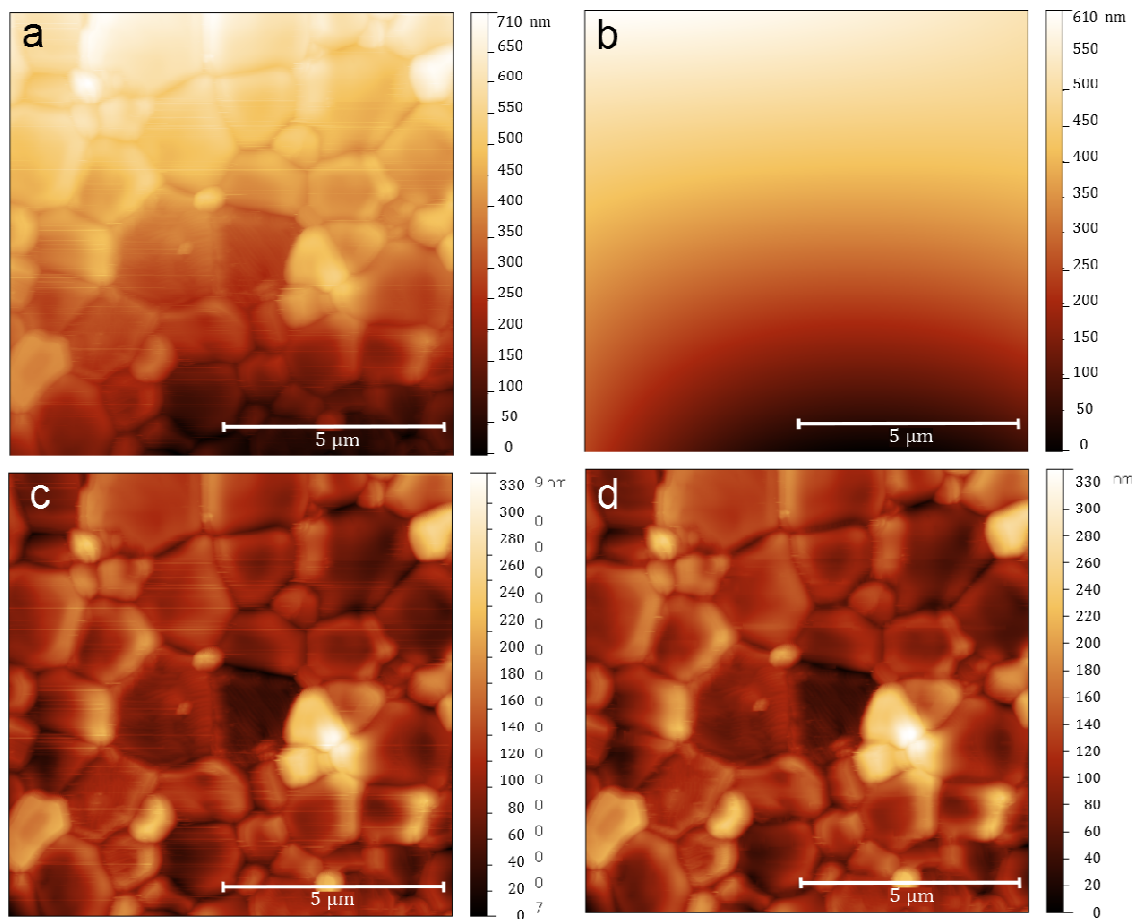


Figure 9. Series of AFM images demonstrating the processing necessary before analysis of grain topography: a) Initial image, b) piezoelectric motor background for removal, c) flattened image, and d) line flaws removed from image.

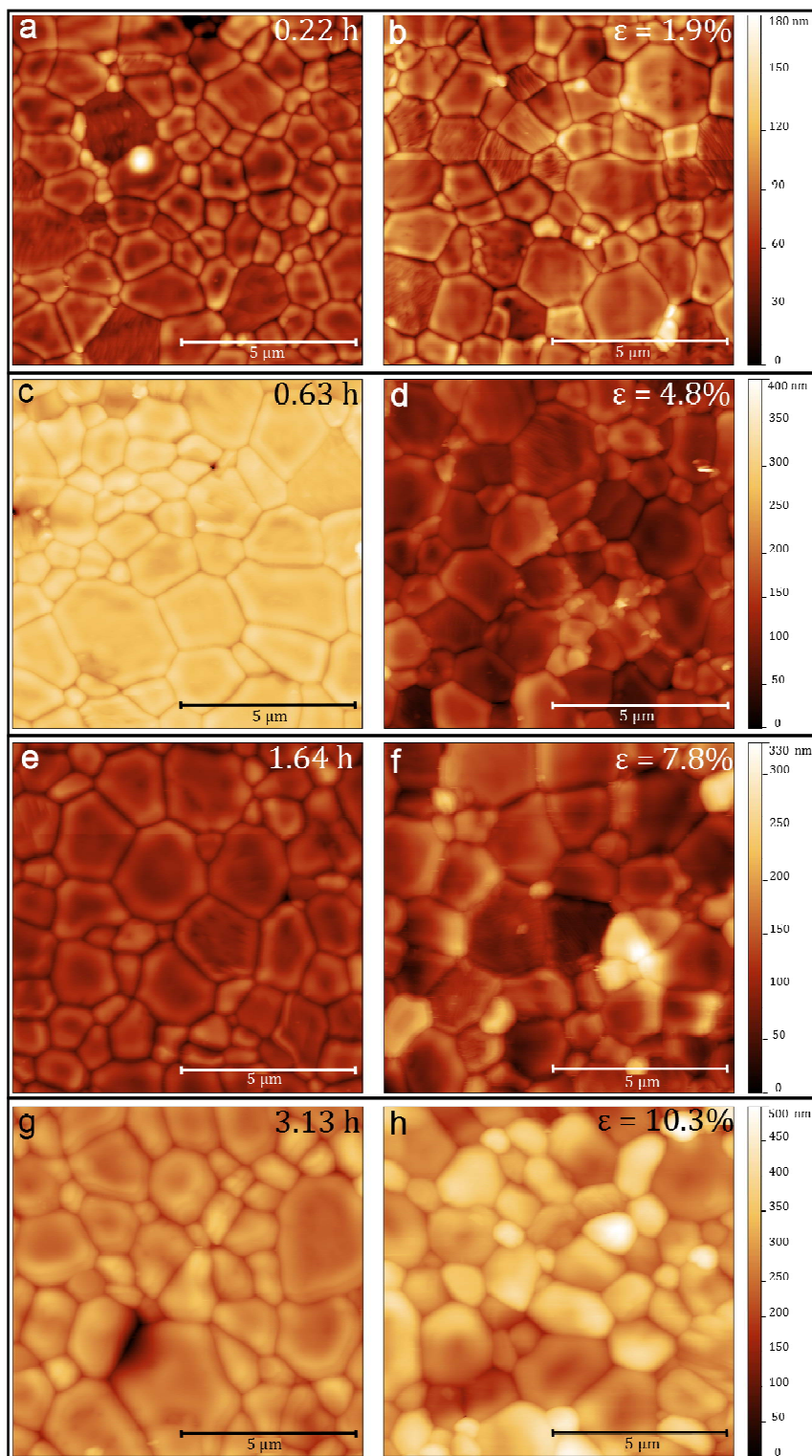


Figure 10: AFM images comparing the surfaces of annealed and deformed samples (Sample 6) progressing with increasing time and strain. The images in the right hand column are from samples deformed to strains of b) 1.9%, d) 4.8%, f) 7.8 %, and h) 10.3%. The images in the left hand column are from the anneal chips paired with deformed samples. The samples were at 1250°C for a) 0.22 h, c) 0.63 h, e) 1.64 h, and g) 3.13 h.

2.6 Development of Analysis Method

The approach laid out by Langdon (1976) for analyzing GBS quantifies the strain due to sliding between two rigid blocks. To apply it to the deformation of forsterite undergoing diffusion creep, the grains must be approximated as flat topped blocks. The effect of thermal grooving on the surface topography of the grains makes this flat top approximation difficult. Two examples of an AFM profile are presented in Figure 11 with line graphs of surface height, z , as a function horizontal position, x . The image and line profile in Figure 11b are from a sample deformed at 1250°C for 0.6 h to a strain of $\sim 5\%$ (Sample 6-2), while the image and line profile in Figure 11a are from its companion

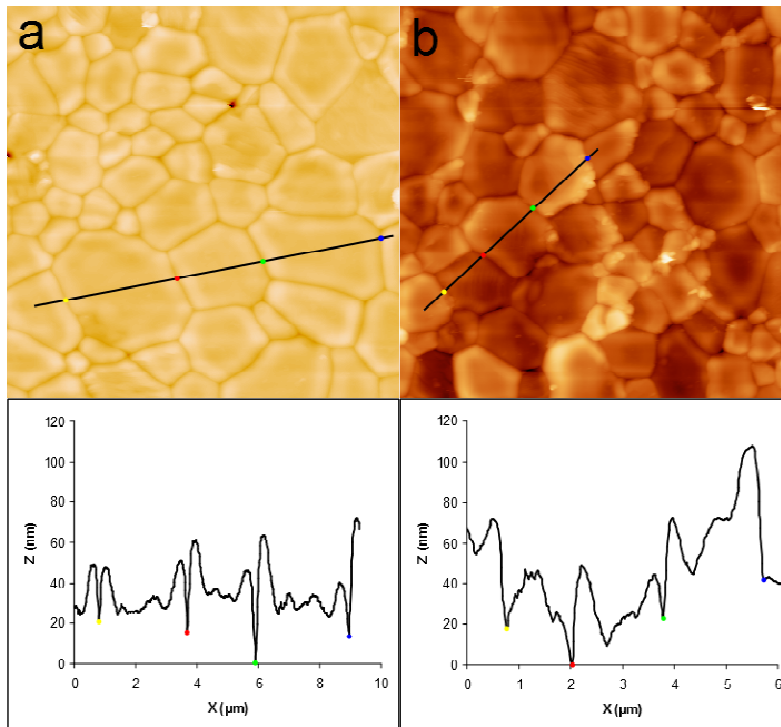


Figure 11. AFM images and line profiles for deformation/anneal pair of Sample 6-2. The sample was deformed at 1250°C for 0.6 h to a strain of $\epsilon = 4.8\%$. Colored dots on the line profiles correspond to grain boundaries along the line profiles included in the images above. a) Annealed sample. b) Deformed sample.

anneal chip. In all the profiles taken, $z = 0$ is set as the lowest point on that profile, not of the image as a whole. Each grain in these profiles shows a 'hilly' surface, especially directly adjacent to the grain boundaries. In the middle of the profile for each grain is a flatter region, which represents the relatively unaltered surface. It is this surface which needs to be fit with a line to approximate the grain as a rigid block.

As thermal grooving alters the surface of grains, the topography of the surface must be corrected for its effects. This correction can be small, if the sample was at temperature for a short time and/or the grain size is large; in either case, a large amount of the original surface would remain unaltered. An image of several large grains in a coarser grained sample that remain largely unaltered is included in Figure 12a.

Thermal grooving produced a thin, bright rim around the edge of the large grains, but

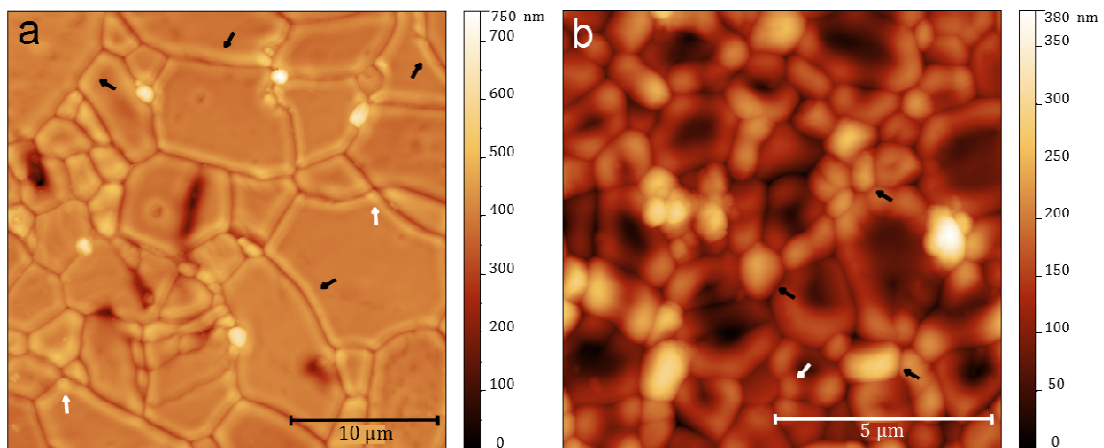


Figure 12. AFM images illustrating the effects of thermal grooving. a) Large grains (Sample 7-1) are characterized by a bright rim, indicated by black arrows, and a darker interior. The white arrows mark bright spots near triple junction, indicating elevated regions created by material from the two adjacent grain boundaries. b) The surfaces of small grains (Sample 1-1), indicated by the black arrows, have been completely altered by thermal grooving and are now just hill shaped. The white arrow marks a bright spot associated with a triple junction.

the interiors are flat. However, the original polished surface in fine-grained samples that experienced high temperatures for a long time can be completely altered. Smaller grains can be completely overgrown by thermal grooving, as demonstrated in Figure 12b.

The simplest approach that can be used to turn AFM profiles of grains into flat topped blocks for analysis of grain boundary sliding is to fit the profiles of each grain, from grain boundary to grain boundary, with a straight line. For samples with little to no thermal grooving, this approach provides an excellent approximation (Clarisse et al., 1999), as the original surface weights the line and the effect of the hills is small. This approach, however, yields a very poor approximation for grains without a sizeable amount of original surface left exposed. As the thin, high ridges near the boundaries evolve to wider, flatter hills, they begin to overlap. Without the original grain surface to anchor it, the fit line will skew higher and higher as time, and thus the extent of thermal grooving, increases. An additional complexity is inherent in reducing a three-dimensional system to two dimensions. Grain surfaces adjacent to triple junctions will have mass from the triple junction as well as the two adjacent boundaries added to them. An examination of Figure 12 reveals brighter spots, indicated in some places by white arrows, near triple junctions. This effect is somewhat mitigated by the choice of profile location; for example, profiles can be chosen to cross grain boundaries perpendicular to the boundary in order to avoid the triple junction areas. This

procedure limits the effect of diffusion in directions other than the plane of the profile, but the assumption of two-dimensional diffusion remains a point of error.

To attempt to correct for these errors, a new fitting method is necessary.

Clarisse et al. (2000) deformed the same sample several times and simply fit a horizontal line to the top of the small grains that had evolved into a single hill. This method relied upon reimagining the same area after each deformation step to allow relative displacements to remain accurate, although the absolute value of displacement would be in error. This method will not work with our experimental set up, however. The approach set out in Mullins (1957) demonstrates that surface diffusion and grain boundary diffusion dominate thermal grooving in forsterite at 1250°C; evaporation is negligible. Thus, the mass from the grain boundary must be accounted for in the hills on the grain surface. Therefore, we introduce a new form for fitting a straight line to grains that takes into account this type of thermal grooving.

A sketch illustrating our fitting method applied to a single grain is described in Figure 13. A second-order polynomial is fitted to the profile data of one grain to determine the 'center', where the mass removed from one grain boundary ends and the opposite grain boundary's mass begins. As demonstrated in Figure 13a, grains are split at this point into two half grains. Both small grains that have experienced extensive grooving and have a parabolic profile, as well as 'tooth-shaped' grains, are fit with this method. Using a reiterative MatLab program, a horizontal line is drawn through each half grain, starting at the highest point. This line is iterated down to a height where the

area below the profile and above the line, the thermal grooving hill, is equal to the area in the grain boundary valley below the line, as shown in Figure 13b. The intersection of this horizontal line and the profile is marked. A line is drawn between the intersection points on either side of the grain, as in Figure 13c. This procedure approximates the

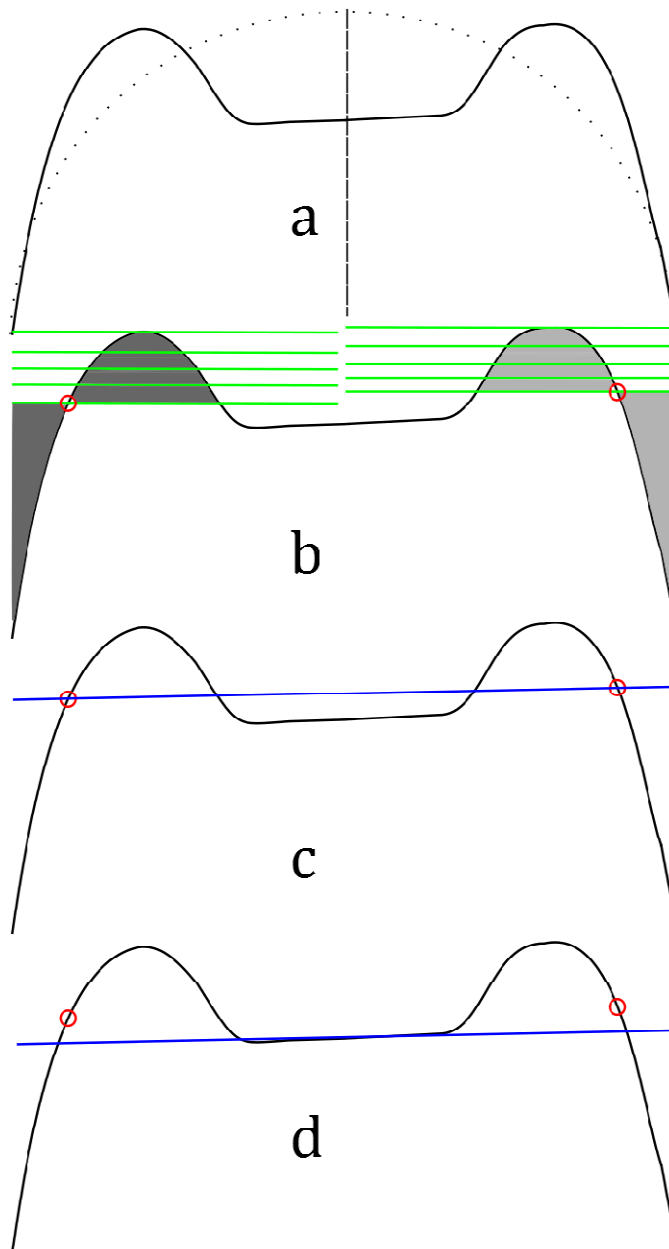


Figure 13. Sketch of a thermally grooved grain. a) The dotted curve represents the parabolic fit to the grain shape and the dashed line separates the grain into two regions, each affected by one grain boundary. b) Each half of the grain is crossed by a horizontal (green) line, which starts at the top of the grain and is iterated lower until the shaded area near the grain boundary matches that in the neighboring hill. The intersection of the horizontal (green) line and the grain profile is marked with a red circle. c) A line (blue) connecting the circles delineates the slope of the grain surface. d) This line is adjusted downward to coincide with the unaltered grain surface.

slope of the surface of the grain if no grooving had occurred. Displacement, v_p , is calculated by taking the difference of the reconstructed surface heights of adjacent grains at the x position of their shared boundary. The average displacement, \bar{v}_p , is determined by summing all displacements measured in all the images after each strain step and dividing by the total number of boundaries analyzed. Compared to fitting the whole grain profile with a line, this method is slightly less sensitive to a profile crossing the grain boundary valley at other than a 90° angle, as slight differences enhance the width of the boundary as well as the width of the hill.

The previous methods detail excellent ways to determine the slope of the fit line for each grain. A difficulty in both ways of fitting is that the valley above a grain boundary is never sampled to its full depth, due to the width of the AFM tip (Clarisse, 2000). As demonstrated in Figure 13c, the straight line calculated for any grain will always sit above the actual grain surface, as the mass in the hills from thermal grooving are not balanced by the deficit in the deep valleys. The assumption that grain boundaries groove identically means that the missing area for the grain boundary valleys should be the same for each grain. This assumption does not mean that the all the fitted lines are off by the same height, however. Larger grains are affected by this deficit less than small grains. To correct the fitted lines to truly represent the original surface, the correction needs to be scaled by grain size. For each experimental step, a profile of an annealed sample is taken across one of the larger grains for which the original surface is preserved. The fit line for that grain is manually adjusted to pass

through the original surface. This step is accomplished by altering the height intercept of the line, leaving the slope of the line unaltered, as shown in Figure 13d. For each strain step, a reference grain provides a width, d_{ref} , and the correction factor, δb , which are used to scale the grains in all the profiles for that experimental step. If the fit line for the i^{th} grain is

$$z_i = m_i x + b_i, \quad (6)$$

then

$$z_i = m_i x + b_i - \delta b * \frac{d_{ref}}{d_i}. \quad (7)$$

Large grains are scaled very little, while smaller grains receive a greater correction.

Table 1 lists the reference grain sizes and correction factors for the samples analyzed.

Profiles start at the center of one grain boundary valley and end at the center of another, with at least one valley in between. This approach means that the number of analyzed grain boundaries on which sliding has occurred is always one less than the number of grains in a profile. The number of grains analyzed in an image are summed and then divided by the total length of the profiles to obtain n_r for Equation (4).

Grain sizes were calculated two ways. One method often used in the earth sciences to measure grain size is the line intercept method, with a scaling factor of 1.5 turn a 2-D distribution into a 3-D grain size (Han & Kim, 1998). A second method of measurement involves calculating the area of a grain, equating that area with that of a circle, and reporting the diameter of that circle as the grain size. There is currently no consensus on whether to apply a scaling factor to represent a 3-D distribution, so the

equivalent diameters presented here have had no scaling applied (Heilbronner and Barrett, 2014). Grain sizes measured by the line intercept method differ from those obtained from the equivalent circle area method by a factor 1.69 as illustrated in Figure 14.

As experimental duration increases, openings at the surface can expose grains that were originally hidden. These highly open areas were avoided when choosing the locations of line profiles. Grain switching is also not accounted for in this methodology. For the amount of strain in these experiments, <20%, grain switching can be disregarded as a source of error (Clarisse et al. 2000).

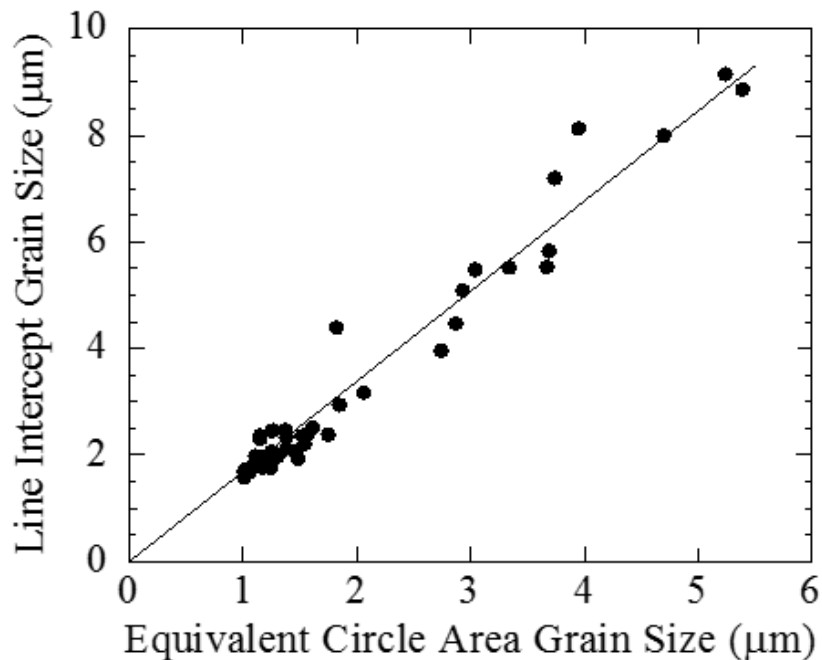


Figure 14. Comparison of grain sizes determined from the line intercept and equal area circle methods. The line intercept method produces grain sizes larger than the equivalent circle area method by a factor of 1.69 ± 0.03 .

2.7 Examples of Microstructures

Samples were fabricated in different batches, most of which have a grain size of $\leq 3 \mu\text{m}$, although one batch had a larger grain size. AFM images of an anneal chip with a grain size of $d = 7.2 \mu\text{m}$ and of an anneal chip with a grain size of $d = 1.7 \mu\text{m}$ are included in Figures 12a and 12b, respectively. The time sequence in Figure 7 for a fine-grained sample consistently shows an equilibrium microstructure, with straight grain boundaries and 120° triple junctions. Grain growth was small during these experiments with grain sizes $< 3 \mu\text{m}$, as demonstrated by the histograms of grain size in Figure 15 for the time sequence in Figure 7. The largest change in the grain size distribution with increasing time is the loss of the smallest grains, which causes the average grain size to increase.

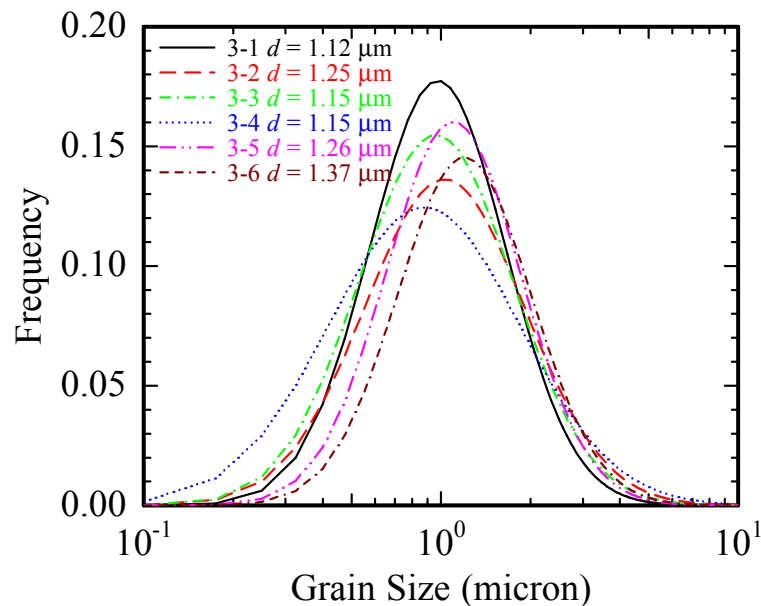


Figure 15. Histogram of grain sizes determined for the time evolution series presented in Figure 7. The similar shape of the grain size distributions indicate the smaller grains remain throughout the experiment. Grain boundary migration is not a critical factor in these experiments.

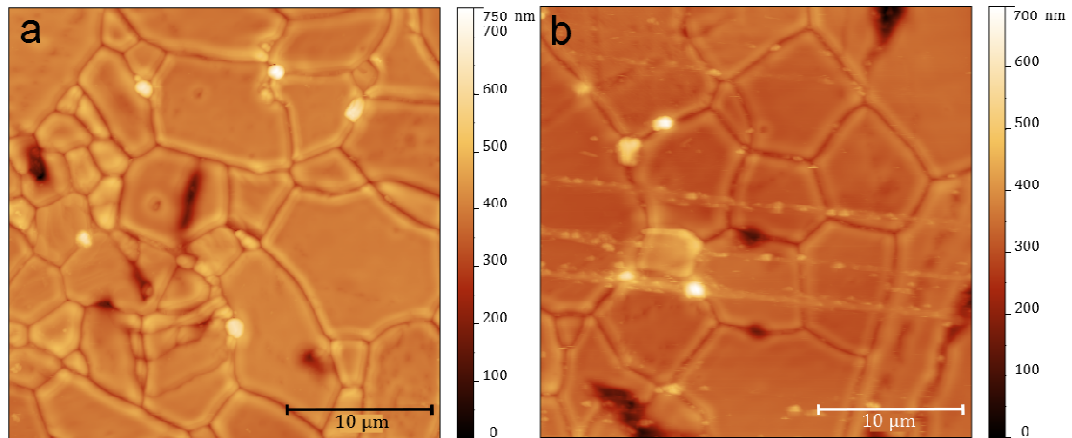


Figure 16. AFM images illustrating the evolution of texture of large-grained samples with time. The samples were at 1250°C for a) 3 h with $d_{ave} = 7.2 \mu\text{m}$ and b) 5 h with $d_{ave} = 8.9 \mu\text{m}$. In the later image, the grain boundaries are straighter and many of the very small grains have been incorporated into larger grains.

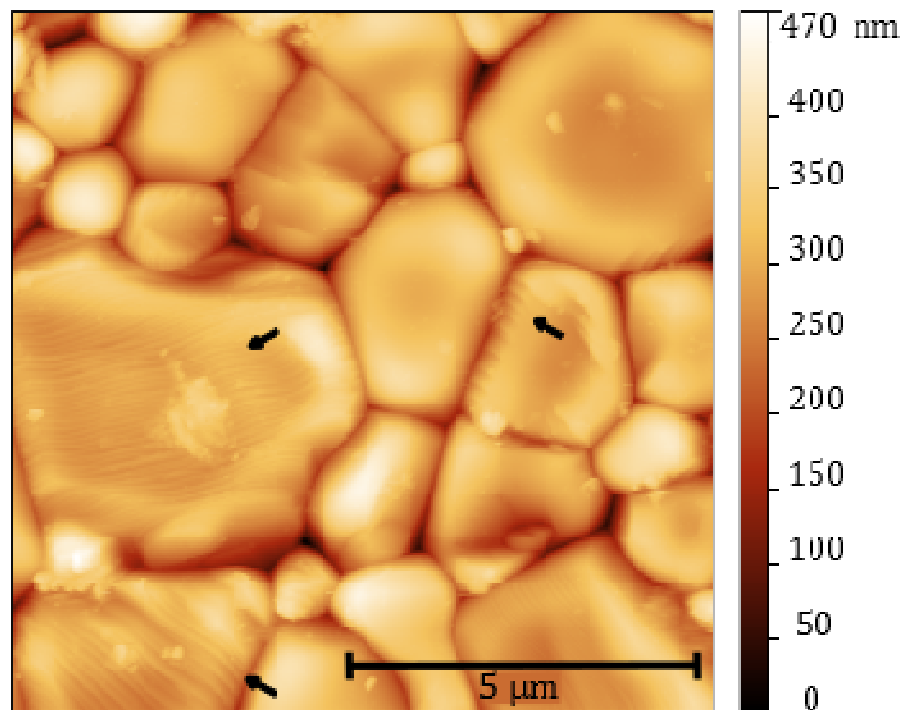


Figure 17. AFM image of Sample 2-1 annealed for 11.8 h illustrating faceting of grains at locations indicated by black arrows. The rightmost arrow shows faceting only along the plane of the grain boundary, not the center of the grain.

These smallest grains would generally be avoided when taking profiles, so grain boundary migration does not significantly influence these experiments. Grain boundary migration would alter the assumption that the ridge adjacent to the grain boundary is solely shaped by diffusion. In contrast to these small grain samples, samples with large grains have many curved grain boundaries, indicating that grain growth is active. The AFM micrographs in Figure 16 from a large-grained sample at two different times reveal a larger grain size and more equilibrated texture after a 5-h anneal than after a 3-h anneal. These larger grains have experienced more extensive grain boundary migration. The effect of grain boundary migration on the surface topography is minor for these larger grains, as there is a great deal of the original surface left unaltered. The line fitted to the grain is weighted by this surface, which helps accurately align the slope of the fit line to the slope of the grain.

As the AFM is very sensitive to vertical displacements, some features that would be barely or not at all visible in an SEM micrograph are clearly visible in an AFM image. One of the most noticeable is faceting on a surface. As olivine is not known to form twins, this faceting is attributed to the grain surface being a high energy plane. Thermal grooving allows this high energy plane to facet to two, lower energy planes, which causes the ridges imaged in grains in Figure 17. Although the steps due to the faceting are on the order of 10s of nm high, they do not fundamentally alter the fit for the

Table 1. Vertical correction values for grain surface fitting.

Sample	Step	Image	Profile	Grain	dref (nm)	δb correction (nm)
1	1	0	3	2	3789	13.5
1	2	6	11	2	3010	30
1	3	0	20	2	1945	35
1	4	1	6	2	2071	70
1	5	2	7	1	2667	42
1	6	3	5	1	3044	65
2	1	0	2	2	3369	20
2	2	1	8	1	2644	27
2	3	0	6	1	4302	13
3	1	0	4	1	1749	3
3	2	1	2	2	3287	12
3	3	1	8	1	2564	25
3	4	0	3	2	3125	20
3	5	2	5	4	2330	18
3	6	2	13	2	3276	18
5	1	0	3	1	3059	37
5	2	2	3	2	3687	90
5	3	1	10	1	4498	120
6	1	2	7	1	1917	10
6	2	0	2	1	2831	7
6	3	0	13	1	2432	12
6	4	0	3	1	2313	28.5
7	1	0	6	1	7793	10
7	2	1	2	1	9227	7
9	1	1	8	1	12281	3
14	1	4	1	3	5679	2
14	2	0	14	1	6617	7
15	1	0	15	1	7014	5
16	1	0	6	4	3311	13.5

original grain surface. To avoid any ambiguity, however, faceted grains were never chosen as the reference grain for a sample.

2.8 Discussion

The ratio of grain boundary sliding strain to total strain, ξ , should be stress independent within a deformation mechanism regime, but a transition to a different mechanism will induce a change in the value of ξ (Gifkins, 1977). To characterize ξ for diffusion creep, most samples were deformed at a low differential stress (60 MPa). Experimental conditions and grain sizes for the anneal chips are summarized in Table 2, while Table 3 has this information and mechanical data for the paired deformed samples. Deformation experiments on fine-grained samples with grain sizes of $\sim 1 \mu\text{m}$ yield $\xi = 63\%$, as shown in Figure 18. For our two samples with a larger grain size, between 4 and 6 μm , that were deformed at 60 MPa, the results in Figure 19 yield $\xi = 53\%$. Several studies on metals (Gifkins, 1977) and ceramics (Clarisse et al., 1999; Schmid et al., 1977) found that an increase in grain size resulted in a decrease in the contribution of grain boundary sliding, but the range in grain size was too small to accurately determine the dependence of ξ on grain size. Our results are similar in scope. A fit of ξ as a function of grain size in Figure 20 results in a slight negative correlation of -0.03 ± 0.02 , which confirms the observation that larger grains have less grain boundary sliding.

In an attempt to confirm the lack of stress dependence of ξ in the diffusion creep regime, two samples were deformed at a stress of 1 MPa. Analysis of the results

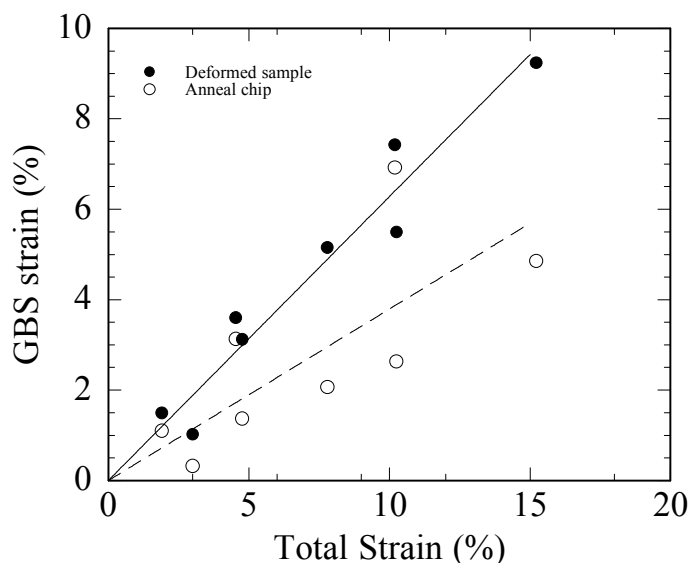


Figure 18. Plot of GBS strain calculated from AFM images for fine-grained ($\sim 1 \mu\text{m}$) samples deformed at 60 MPa versus total strain.

from these deformed samples yielded $\xi = 343\%$, as shown in Figure 21. The data from the corresponding anneal chips, plotted in the same figure, actually showed a higher contribution of GBS, with $\xi = 430\%$. This level of GBS contribution to total strain is clearly impossible. The long time required to produce even a small strain in samples

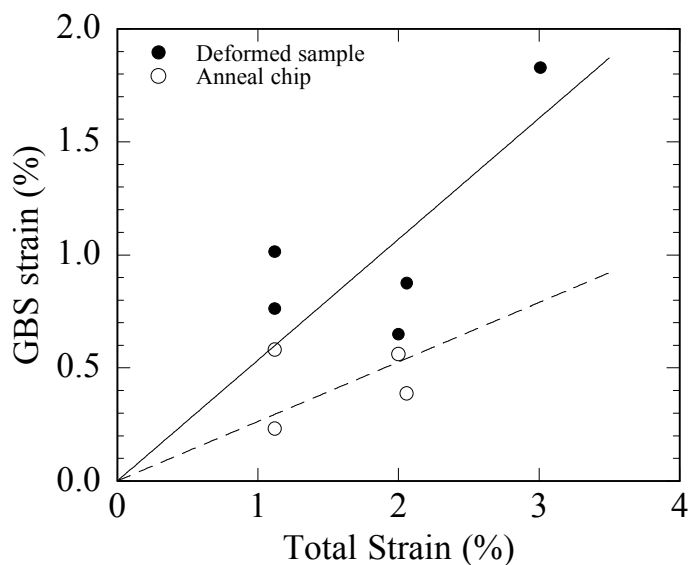


Figure 19. Plot of GBS strain, calculated from AFM images as a function of the total strain for larger grained ($4\text{-}6 \mu\text{m}$) samples deformed at 60 MPa.

deformed a small stress (1 MPa) resulted in complete alteration of the grain surfaces due to thermal grooving. The grain boundary sliding strain determined for the samples deformed at 1 MPa is clearly unreliable.

The contribution of grain boundary sliding strain in diffusion creep of forsterite, $\xi = 63\%$, is similar to the value of $\xi = 70\%$ reported for alumina (Wakai et al., 1997; Clarisse et al., 1999). It is a bit smaller than the value of $\xi = 75\%$ determined for diffusion creep of a Mg-Al alloy (Kottada and Chokshi, 2007) and the value of $\xi = 84\%$ obtained for diffusion creep of an alumina-zirconia ceramic (Clarisse et al., 2000). The similarity of the value of ξ determined for forsterite to the value reported for pure alumina and the difference from values for two-phase deformation suggests that grain boundary sliding acts differently in a multi-phase rock than in single-phase materials. The theoretical models of Kim and Hiraga (2000) and Sahay and Murty (2001) predicted very different contributions of grain boundary sliding to diffusion creep. Kim and Hiraga (2000) predicted $\xi = 60\%$ and allowed their grains to remain equiaxed, very similar to our observations. In contrast, Sahay and Murty (2001) predicted diffusion would be the dominant contributor to strain, and this contribution would increase with increasing strain. Our experiments do not support this model. This suggests that the key feature missing from their model is grain rotation, and that the ability of grains to remain equiaxed by rotating is an intrinsic feature of a deformation regime requiring grain boundary sliding. A few experiments were also performed specifically to deform in the dislocation accommodated deformation regime. For a fixed grain size and temperature,

Table 2. Summary of anneal chip data

Sample	Step	Apparent GBS strain (%)	Equivalent Area Circle Grain Size (μm)	Line intercept grain size (μm)	Time at Temp (h)	Total Time (h)
1	1	3.13	1.17	1.76	0.77	0.77
1	2	6.92	1.03	1.70	1.68	2.44
1	3	4.86	1.25	2.06	1.61	4.05
2	1	2.63	1.38	2.33	11.77	11.77
2	2	2.86	1.18	1.88	24.00	35.77
2	3	3.00	1.46	2.07	24.00	59.77
3	1	0.00	1.12	1.81	12.00	12.00
3	2	0.02	1.25	2.45	12.00	24.00
3	3	0.03	1.15	2.30	12.00	36.00
3	4	0.03	1.15	2.36	16.00	52.00
3	5	0.04	1.26	2.46	24.00	76.00
3	6	0.03	1.37	2.47	24.00	100.00
5	1	5.71	1.38	2.12	12.00	12.00
5	2	5.71	1.61	2.51	11.82	23.82
5	3	10.92	1.75	2.38	12.00	35.82
6	1	1.10	1.01	1.58	0.22	0.22
6	2	1.37	1.01	1.69	0.41	0.63
6	3	2.07	1.09	1.80	1.02	1.64
6	4	2.63	1.24	1.76	1.49	3.13
7	1	0.58	3.74	7.20	3.13	3.13
7	2	0.39	5.39	8.86	1.93	5.05
9	1	0.23	5.45	2.40	2.73	2.73
10	1	0.56	4.10	2.77	29.39	29.39
14	1	0.32	3.67	5.53	0.61	0.61
15	1	0.74	1.82	4.39	0.41	0.41
16	1	0.33	3.04	5.48	16.05	16.05

Table 3. Summary of deformed sample data

Sample	Step	Strain at this step (%)	Total Strain (%)	GBS strain (%)	ξ	Equivalent Area Circle Grain Size(μm)	Line intercept grain size (μm)	Stress (MPa)	Strain Rate (1/s)	Normalized strain rate $d = 2 \mu\text{m}$ (1/s)	Time at Temp (h)	Total Time (h)
1	1	4.53	4.53	3.60	0.80	1.1	2.0	60	1.57E-05	2.72E-06	0.77	0.77
1	2	5.66	10.19	7.42	0.73	1.2	2.0	60	1.25E-05	2.97E-06	1.68	2.44
1	3	5.03	15.22	9.24	0.61	1.3	2.0	60	1.15E-05	3.15E-06	1.61	4.05
2	1	0.84	0.84	2.18	2.59	1.6	2.4	1	5E-08	2.39E-08	11.77	11.77
2	2	0.35	1.19	2.65	2.22	1.5	2.4	1	1.4E-08	6.05E-09	11.81	23.58
2	3	0.34	1.53	3.43	2.24	2.1	3.2	1	4E-08	4.36E-08	28.90	52.48
5	1	0.81	0.81	5.51	6.78	1.5	1.9	1	9.41E-08	3.81E-08	12.00	12.00
5	2	0.41	1.22	4.71	3.86	1.5	2.2	1	8.93E-08	4.08E-08	11.82	23.82
5	3	0.27	1.50	6.63	4.43	1.9	2.9	1			12.00	35.82
6	1	1.90	1.90	1.49	0.79	1.0	1.7	60	2.42E-05	3.22E-06	0.22	0.22
6	2	2.86	4.76	3.12	0.66	1.1	1.7	60	1.33E-05	1.93E-06	0.41	0.63
6	3	3.03	7.79	5.15	0.66	1.2	2.0	60	8.16E-06	1.81E-06	1.02	1.64
6	4	2.46	10.25	5.50	0.54	1.2	1.9	60	4.44E-06	9.83E-07	1.49	3.13
7	1	1.12	1.12	1.01	0.91	4.0	8.1	60	2.75E-06	2.12E-05	3.13	3.13
7	2	0.94	2.06	0.88	0.43	5.2	9.2	60	2.46E-06	4.43E-05	1.93	5.05
9	1	1.12	1.12	0.76	0.68	6.1	2.4	60	1.27E-06	3.57E-05	2.73	2.73
9	2	1.89	3.01	1.83	0.61	4.7	8.0	60	2.78E-07	3.61E-06	20.33	23.06
10	1	2.00	2.00	0.65	0.32	5.2	3.2	30	3.27E-07	5.85E-06	29.39	29.39
								45	6.81E-07	1.22E-05		
								60	7.02E-07	1.26E-05		
14	1	3.00	3.00	1.02	0.34	2.9	4.5	50	1.61E-05	4.76E-05	0.61	0.61
15	1	2.10	2.10	1.27	0.60	2.7	4.0	110	4.91E-05	1.26E-04	0.41	0.41
16	1	5.00	5.00	3.40	0.68	3.7	5.8	125	8.34E-07	5.24E-06	16.05	16.05

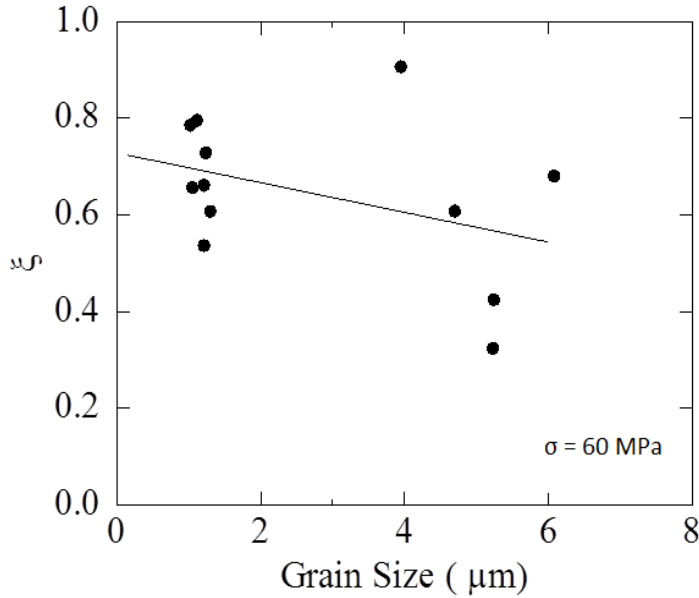


Figure 20. Plot of the grain boundary sliding parameter ξ as a function of grain size. A linear least squares fit yields $\xi \propto (-0.03 \pm 0.02) * d$.

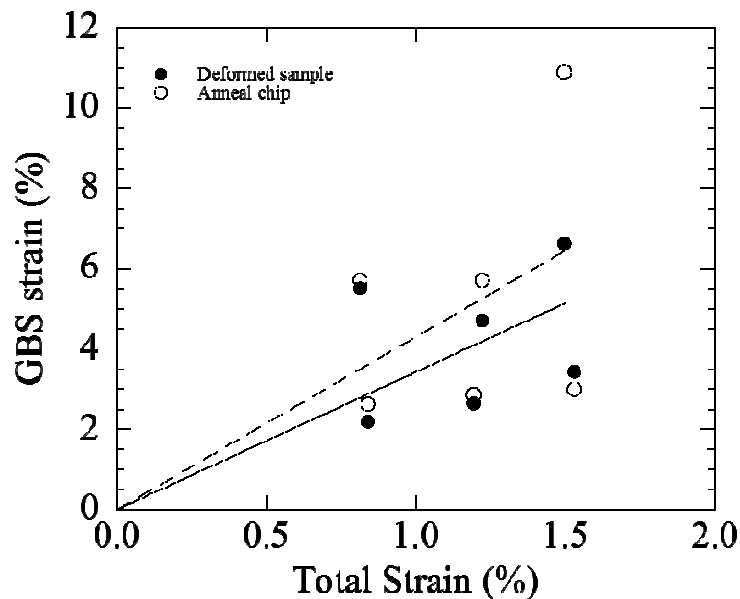


Figure 21. Plot of GBS strain calculated from AFM images as a function of the total strain for fine-grained samples deformed at 1 MPa. These samples show a contribution of GBS to the total strain >100%, which is impossible.

transitioning from diffusion creep to a dislocation accommodated deformation grain boundary sliding mechanism requires increasing the applied stress. At a fixed stress and temperature, the transition can occur with an increase in grain size. Samples were successfully deformed at stresses up to 125 MPa, with Figure 22 showing ξ from the samples deformed stresses greater than 1 MPa. The faster deformation due to

increased stress means the samples were at temperature for less time than samples deformed at lower stresses. This reduction in time makes the high stress data more reliable, as the correction for thermal grooving is smaller than for the samples deformed at lower stresses. Attempts to increase the stress above 125 MPa resulted in fracturing of the sample, which makes the amount of plastic strain impossible to determine. To keep the sample from cracking under high stress, a finer grain size is necessary. Although the finer grain size would push the transition stress higher, the sample would be more be less likely to crack due to thermal expansion anisotropy. With this robust new methodology for determining the strain due to grain boundary sliding, we will be able to characterize in detail the regime the samples transition into at high stresses. This will allow us to distinguish between a grain boundary sliding field and dislocation creep.

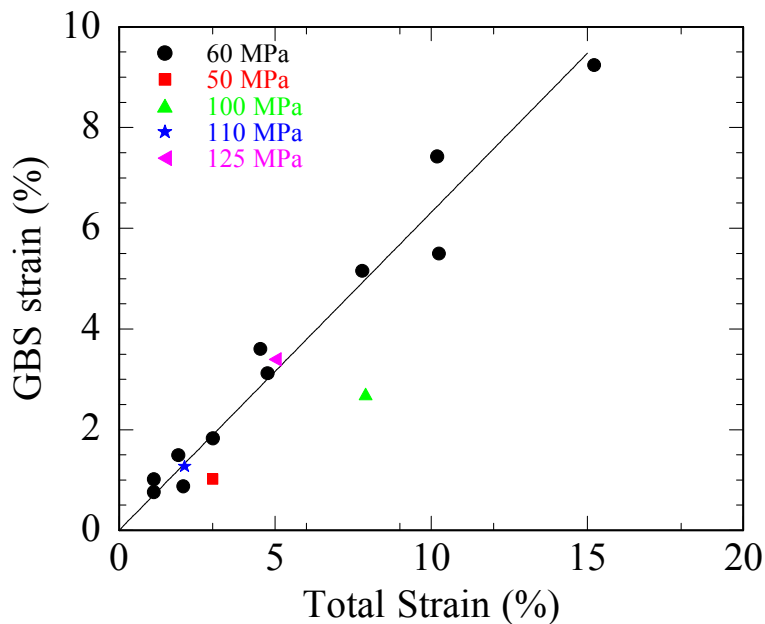


Figure 22.
Plot of GBS strain calculated from AFM images as a function of the total strain for all samples deformed at stresses >1 MPa.

Chapter 3: The Effect of Grain Boundary Impurities on the Deformation Strength of Synthetic Forsterite

Summary

Under sub-solidus conditions, trace elements in mantle rocks are primarily stored along grain boundaries. The effect of these impurities on the physical properties of grain boundaries in an olivine-rich rock has not been explicitly studied. The large difference in deformation strength of lab samples synthesized from fine-grained natural olivine and those prepared from purely synthetic powders may depend on the differences in composition of the grain boundaries. To investigate the role of impurities along grain boundaries on creep strength, deformation experiments were performed on fine-grained, synthetic forsterite (Fo). Samples were either left as high-purity Mg_2SiO_4 or were doped with an impurity, either Ca^{+2} or Pr^{+3} . These samples were then deformed in triaxial compression in a gas-pressure medium creep apparatus at temperatures of 1000° to 1250°C and a confining pressure of 300 MPa. Samples of undoped Fo that deformed in the diffusion creep regime displayed creep strengths similar to previously studied synthetic olivine samples, both iron-bearing and iron-free. Samples of Fo with 0.1 mol% Ca were 4-12 times stronger than the undoped Fo, and the presence of Ca induced abnormal grain growth. The addition of 0.01 mol% Pr increased the strength of the Fo by a factor of 4-23. The similarity of the strengths of the Fo samples doped Ca and with an order of magnitude less Pr indicates that the charge compensating effect for Pr slows the diffusion of the slowest ionic species, Si, by reducing the concentration

of Si interstitials moving in the grain boundaries. These deformation experiments illustrate that the viscosity of polycrystalline olivine is affected by grain boundary composition, even at impurity levels below that necessary to create a second phase. The strengthening effect of adding these impurities does not bring natural olivine creep strengths and pure synthetic creep strengths into agreement. A different explanation must be made to bring these different experimental results together.

3.1 Introduction

Grain boundaries in the Earth play an important role in deformation, electrical conductivity, seismic attenuation as well as other kinetic properties. The effect of grain boundary composition on these properties is not fully understood. In ceramics such as ice (Durand et al., 2006) and Al_2O_3 (Altay and Gülgün, 2003), changes in boundary composition affect, for example, grain growth kinetics. Isovalent cations that segregate to the grain boundaries in Al_2O_3 affect creep strength (Ikuhara et al., 2001, Yoshida et al., 1998, Yoshida et al., 2001), as do heterovalent cations (Yoshida et al., 2005). However, no systematic correlation of this alteration of creep strength with size or valence of the impurity has been reported. In their studies of impurities in Y_2O_3 stabilized ZrO_2 , Mimurada et al. (2001) observed that ions smaller than Zr weakened the ceramic while larger ions strengthened it, but they observed no direct correlation between strength and size or charge. For olivine, Spandler et al. (2007) showed that the diffusion coefficients for various incompatible elements do not exhibit a systematic dependence on size or charge. As Hiraga et al. (2004) have demonstrated that grain

boundaries act as a primary storage site for incompatible elements, it is important to investigate the effect of composition on rheological properties.

3.2 Theoretical Background

In the upper mantle, olivine, $\text{Mg}_{1.8}\text{Fe}_{0.2}\text{SiO}_4$, is the most abundant phase, and likely the weakest phase under a wide variety of conditions. Natural olivine-rich rocks contain a number of minor and trace elements. Hiraga et al. (2007) suggest that heavy alkali elements are likely to be primarily stored in grain boundaries in the mantle, so naturally occurring olivine will have cations in the grain boundaries that are larger and have a different charge than Mg or Fe. A number of previous deformation experiments on olivine used natural single crystals (e.g., Bai et al., 1991), cored cylinders of polycrystalline olivine (e.g., Chopra and Paterson, 1981), or powdered single crystals synthesized back into dense cylinders (e.g., Hirth and Kohlstedt, 1995). While these approaches produce samples with compositions representative of mantle olivine, samples of high-purity, synthetic forsterite was chosen for study in order to isolate the effect of grain boundary composition on deformation strength of earth materials. By focusing on the Mg end-member forsterite, any complications introduced by the presence of Fe^{3+} are avoided and the effect of boundary chemistry on creep behavior can be isolated.

One issue with results from deformation studies on purely synthetic olivine samples is a marked difference in strength compared to samples composed of natural olivine. High-purity synthetic olivines, both iron bearing (Faul and Jackson, 2007) and

iron-free (Tasaka et al., 2013), are much stronger than natural synthetic samples deformed under similar conditions (Hirth and Kohlstedt, 1995). Figure 1 illustrates this strength difference for diffusion creep of olivine samples with a 2 μm grain size deformed at 1200°C and 300 MPa confining pressure. These high-purity samples lack the impurities the natural samples have on the grain boundaries.

To change grain boundary chemistry, elements that are highly incompatible in the Fo lattice were added to our samples. Hiraga et al. (2004) demonstrated that many common impurities show a preference for the Mg sites in olivine grain boundaries. The greater the lattice strain to accommodate an impurity, the more strongly it segregates to the boundary. Cation impurities sit in the core of a grain boundary, not as a secondary phase (Hiraga et al. 2007). However, the charge of impurities located in grain

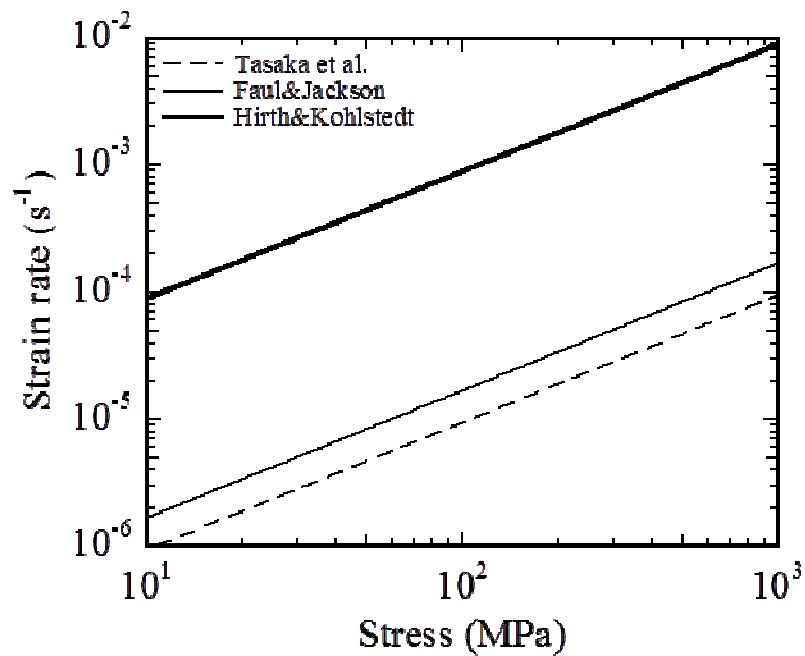


Figure 1: Comparison of strength in the diffusion creep regime for fine-grain San Carlos (Hirth and Kohlstedt, 1995), synthetic iron-bearing olivine (Faul and Jackson, 2007), and synthetic forsterite (Tasaka et al., 2013).

boundaries can produce a space charge region extending up to 10 nm from the boundary (Johnson, 1977).

With the addition of impurities, the energy of the system increases for two main reasons: size and valence differences between the impurity and the host. The elastic strain energy associated with the accommodation of a differently sized cation, $U_{elastic}$, can be approximated by (Brice, 1975)

$$U_{elastic} = 4\pi E_{\alpha} N_A \left[\frac{r_0^3}{2} (r_i - r_0)^2 + \frac{1}{3} (r_i - r_0)^3 \right], \quad (1)$$

where E_{α} is the effective Young's modulus of the site α , N_A is Avogadro's number, r_0 is the radius of the site, and r_i is the radius of the substituted ion. The strain due to charge differences, $U_{electric}$, can be calculated from the expression (Wood and Blundy 2001)

$$U_{electric} = \frac{N_A e^2 (Z_c - Z_0)^2}{8\pi \epsilon_0 \epsilon r}, \quad (2)$$

with e being the charge of an electron, Z_c the charge of the cation, Z_0 the charge associated with the site, ϵ_0 the permittivity of free space, ϵ the dielectric constant of the crystal, and r the effective radius over which the excess charge is distributed. For olivine, this radius is taken to be the radius of the cation site plus the diameter of one O^{2-} (Wood and Blundy 2001).

To study the effects of heterovalency and ionic size on grain boundary creep strength, two elements were chosen, Ca and Pr. Calcium ions are isoivalent with Mg^{2+} , but have a radius of $\sim 1.12 \text{ \AA}$ in octahedral sites (Shannon 1976), significantly larger than octahedrally coordinated Mg ions with an ionic radius of $\sim 0.9 \text{ \AA}$. The 25% larger ion segregates strongly to grain boundaries in olivine with $U_{elastic} \approx 32 \text{ kJ/mol}$, corresponding

to a partition coefficient of $\sim 3 \cdot 10^{-2}$ (Beattie, 1994). To investigate the effect of heterovalency on deformation strength, the element praseodymium was chosen. With an effective ionic radius roughly equal to that of Ca (Shannon 1976), Pr is a +3 cation. Differences between the deformation of Ca-doped samples and Pr-doped samples can, therefore, be attributed to the effect of charge alone. With a 3+ cation on the site, the radius of the site drops from 0.9 to 0.71 (Hiraga and Kohlstedt, 2009), which makes $U_{\text{elastic}} \approx 118 \text{ kJ/mol}$ and $U_{\text{electric}} \approx 25 \text{ kJ/mol}$, leading to a partition coefficient of $\sim 6 \cdot 10^{-5}$ (Beattie, 1994).

3.3 Sample Preparation

Forsterite powder was prepared from nano-powders of high-purity brucite ($\text{Mg}(\text{OH})_2$) and silica (SiO_2). These powders were mixed in a 2:1 ratio of Mg to Si. A small additional amount of SiO_2 was added to create a small, <1%, amount of enstatite, MgSiO_3 . This procedure ensured that the forsterite composition has the same silica activity as the mantle. These powders were mixed in high-purity ethanol and tumbled in a plastic bottle with plastic coated iron balls for $\sim 24 \text{ h}$. This suspension was then

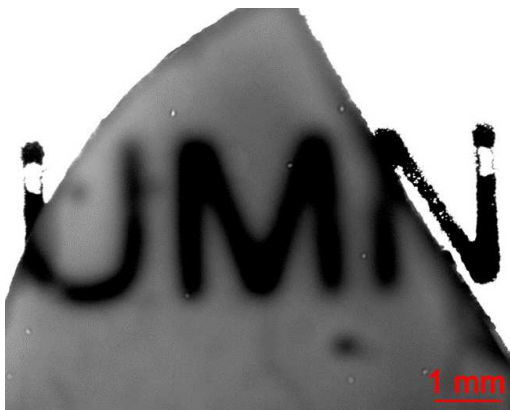


Figure 2. Optical-light picture of fully dense forsterite sample with a grain size of $\sim 1 \mu\text{m}$. This wedge is transparent at a thickness of 0.5 mm.

transferred to a beaker and dried at 60°C on a hot plate until no visible moisture remained. Next the powder mixture was coarsely disaggregated in an agate mortar and placed in an alumina boat for calcining in air at 1000°C for 3 h. This stage reacted the Mg and Si phases together to form forsterite and ensured that any contamination from the alcohol or plastic was removed. After cooling, the powder was again disaggregated in an agate mortar. Powder was transferred to a cold-press die and shaped into a cylindrical green body. This body was then carefully placed in a latex balloon, the air was removed from the balloon, and the balloon was sealed. A second balloon was sealed around the first, after having the air removed, to ensure no leakage. This assembly was then placed into an isostatic pressure vessel, filled with either anti-freeze or hydraulic oil. This vessel was pressurized to >100 MPa for ~5 min before the pressure was gradually released. The cold-pressed green body was removed from the fluid medium and carefully cut out from the balloons. The compressed powders were placed on a platinum crucible and fired in vacuum at 1400°C for 5 h. After this densification step, samples were >99.9% dense. As shown in Figure 2, the density is high enough to allow one to read through polished samples. Five hours at 1400°C is more time than is necessary to produce a high density sample; the additional time was an attempt to effectively exhaust grain growth. Grain growth is rapid at first, then quickly decreases to a very slow rate. As subsequent deformation experiments using these samples were

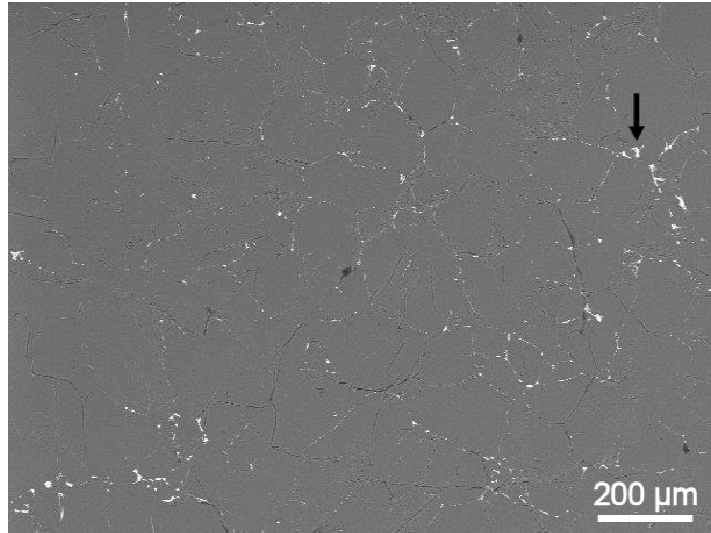


Figure 3. SEM backscatter electron image of Pr-doped sample with a Mg:Pr ratio of 1:10². The bright white phase is a Pr rich melt, which is sitting along grain boundaries. The black arrow is pointing to larger pocket of the melt. This bright phase outlines the large (>50 μm) grains of this sample.

performed at lower temperatures, grain growth during deformation should be minimal.

Fully dense samples were cylinders ~4 mm in diameter and at least 7 mm in length.

After densification some additional polishing was performed to make the ends of the cylinder flat and parallel.

Impurities were added to some of the Fo powder after the calcination step but before sintering. In ethanol, either $\text{Pr}(\text{NO}_3)_3 \cdot 6\text{H}_2\text{O}$ or $\text{Ca}(\text{NO}_3)_2$ were added to the powder. The nitrates dissolved in the ethanol and the slurry was mixed to coat the Fo powder with the impurities. After mixing, the slurry was left in air to evaporate the ethanol. The powder was disaggregated and then calcined again at 1000°C for 3 h. This second calcination removed any remaining N, C, or H and allowed time for the impurity to diffuse into the sub-micron Fo grains. Densification proceeded in the same manner as for the undoped samples. The 5-h anneal at 1400°C allowed the grains to grow,

which aided in the equilibration of the impurity between the grains and grain boundaries, in addition to growing the grains.

The initial amount of impurity was in a $1:10^{-2}$ ratio of Mg:Pr/Ca. In Pr-doped samples, this concentration of impurity was enough to turn the sample from a clear whitish to pale green and induce extreme grain growth. A secondary phase appeared in the grain boundaries, similar to the way over-doping alumina with Y creates a second phase (Gülgün et al., 2002). In our case, however, the precipitate was a melt, as evidenced by its cusped shape in triple junctions and the lack of a clear Kikuchi pattern when analyzed with electron backscatter diffraction (EBSD.) In the scanning electron microscope (SEM) micrograph of these 1% Pr-doped samples in Figure 3, the Pr-enriched melt phase appears bright white. When the concentration of impurities was lowered to $1:10^{-4}$ Mg to Pr, the samples remained clear and fine grained. In Ca-doped samples, the initial dopant level resulted in white samples with many large grains. Decreasing the dopant level to $1:10^{-3}$ Mg to Ca resulted in fine-grained, clear samples.

3.4 Deformation Experiments

Two different apparatuses were used for deformation experiments. The gas vessel uses Ar as a pressure medium, providing a confining pressure of 300 MPa (Paterson, 1990). To prevent the Ar from reaching the sample, the sample cylinders were placed inside an Fe tube, sandwiched between alumina pistons, which were sandwiched between zirconia pistons with steel pistons on the outside. This machine has an internal load cell, which allows for high resolution load measurements. Displacement is measured with

roughly 1 μm resolution externally to the pressure vessel. Deformation was always carried out in compression, under various constant load steps. For these confined deformation experiments, the rock cylinders were placed in a Ni can. In most olivine deformation experiments, the Ni is used to buffer the oxygen fugacity of the sample. Although oxygen fugacity was not a concern for this iron-free olivine, the Ni had two uses in these experiments. Although Ni flows easily at the experimental temperatures used, corrections to the stress must be still made for the Ni can. By maintaining the same assembly, comparison of results to those previously obtained in the same apparatus was simplified. The more important purpose for the Ni can was to take up space. Traditional gas-medium experiments for compression deformation required samples with either a 10 mm or a 7 mm diameter, which is generally larger than our forsterite cylinders after sintering. Heat enters the system through a Mo wire-wound furnace, which provides a zone of uniform temperature of roughly 30 mm in length. The sample was always centered in the hot zone, reducing the temperature gradient to less than 1°C over its length.

The other apparatus used for deformation experiments provided no confining pressure. This one-atmosphere rig is a simple end-loaded machine. A SiC piston is attached to a rigid platform above the rock cylinder, and the bottom SiC piston is moved up and down with a cantilever. The sample is loaded by stacking weights on the other side of the lever arm. The calculation of load is a simple one, as the loading points of the cantilever are at 1:1 positions. Any load applied to the lever is directly transferred

to the sample. A furnace on a mobile platform can be raised around the sample, providing a roughly 20-mm long hot zone. Displacement was measured both inside the furnace and outside. The internal displacement was measured using SiC rods resting on plates above and below the sample, which transfers that sample displacement to a direct current displacement transducer (DCDT) located above the top SiC piston. The symmetry of the rods to the bottom and top of the sample almost perfectly compensates for thermal expansion. The external measurement of displacement included all of the displacement between the top platform of the machine and the bottom. This placement means that the external DCDT measures the thermal expansion of every component of the system. However, once the set temperature is reached and changing thermal expansions stop, the external and internal DCDTs yield very similar measurements of displacement.

3.5 Grain Size Determination

Several different methods are currently in use in the earth sciences for determining grain size (Berger et al., 2011). The most popular in the past has been the line intercept method (Mendelson, 1969; Han and Kim, 1998). Shown in Figure 4, parallel lines were scribed across an image, and the number of grains crossed was counted. The length of the line, divided by the number of grains crossed, times 1.5 gives an approximate value for grain size. This method was determined to be an accurate measure of the grain diameter for a random planar cut through a 3-D matrix of tetrakaidecahedral grains of

identical size. It has the advantage of being computationally easy and, as so many previous works have used this method, it is easy to compare data sets.

A newer method of grain size measurement involves determining the area of each grain in an image of a polished surface (Heilbronner and Barrett, 2014). Samples were polished flat before the grain boundaries were thermally grooved. Secondary electron images clearly showed the grain boundaries, which were manually traced, as illustrated in Figure 5. This map of the grain boundaries was analyzed by converting the number of pixels in each grain into an area. Grain size from this method is assumed to be the diameter of the circle that has an equivalent area. This method has the advantage of measuring every complete grain in an image, as well as simultaneously providing other information such as aspect ratio and orientation of the long axis of a grain. The equivalent circle diameter method produces a smaller grain size than the line intercept method, which may be related to the fact that the equivalent circle method has no generally agreed upon correction to 3D. The difference in grain size distributions from the different methods is demonstrated in Figure 6. Optical or electron microscope images are often used for these measurements, but electron back-scatter diffraction (EBSD) maps also provide this information. Both a line intercept and an equivalent circle diameter method are incorporated into the HKL software, a popular analysis software for EBSD data. These methods produced slightly different values of grain size. For EBSD images, the very small grains yielded few clean adjacent Kikuchi patterns, so they were not indexed. These grains, which appear to be blank spaces in an EBSD map, were either

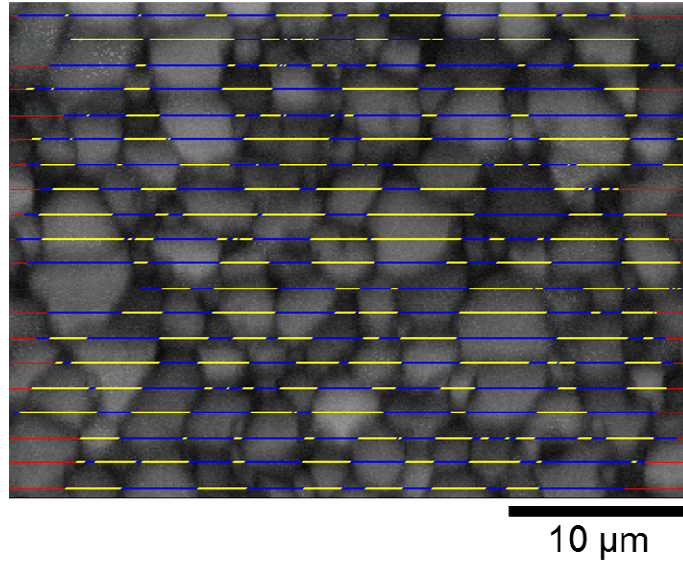


Figure 4. Example of line intercept method of determining grain size. This EBSD image was analyzed with 20 lines. Red portions of the lines indicate a section of the line which is not bounded by two grain boundaries. Line sections which are bounded by two grain boundaries alternate between blue and yellow, to aid the eye in distinguishing between different grains. The lengths of the individual blue and yellow lines are summed, divided by the number of lines summed, then multiplied by 1.5 to determine grain size.

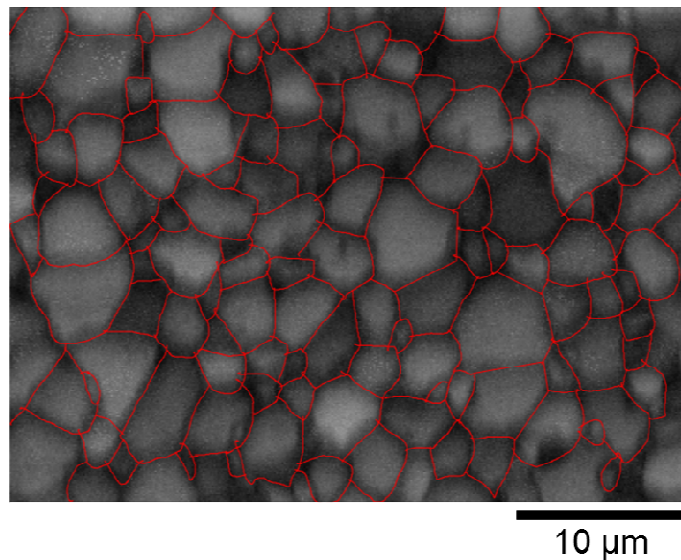


Figure 5. The same EBSD micrograph as was shown in Figure 4. This image shows the grain boundaries hand traced in red. Grain size is determined by calculating the area of a grain bounded by red and then calculating the diameter of a circle with the same area. The average of these diameters is the average grain size of the image.

overgrown in the noise reduction process or left unanalyzed by the software. The area equivalent circle method produces grain size distributions similar in shape and position to the EBSD results. Compared to EBSD approach, the area equivalent circle method requires less sample preparation, is faster, and is easier to image all the grains, so the grain sizes reported and used for correcting deformation data were from the area equivalent circle method.

To determine grain size, a sample was polished with sequentially finer diamond lapping films, down to 0.5 μm . After polishing, the sample was cooked on a Pt plate in air at 1300°C for 0.5 h. This heat treatment thermally grooved the grain boundaries

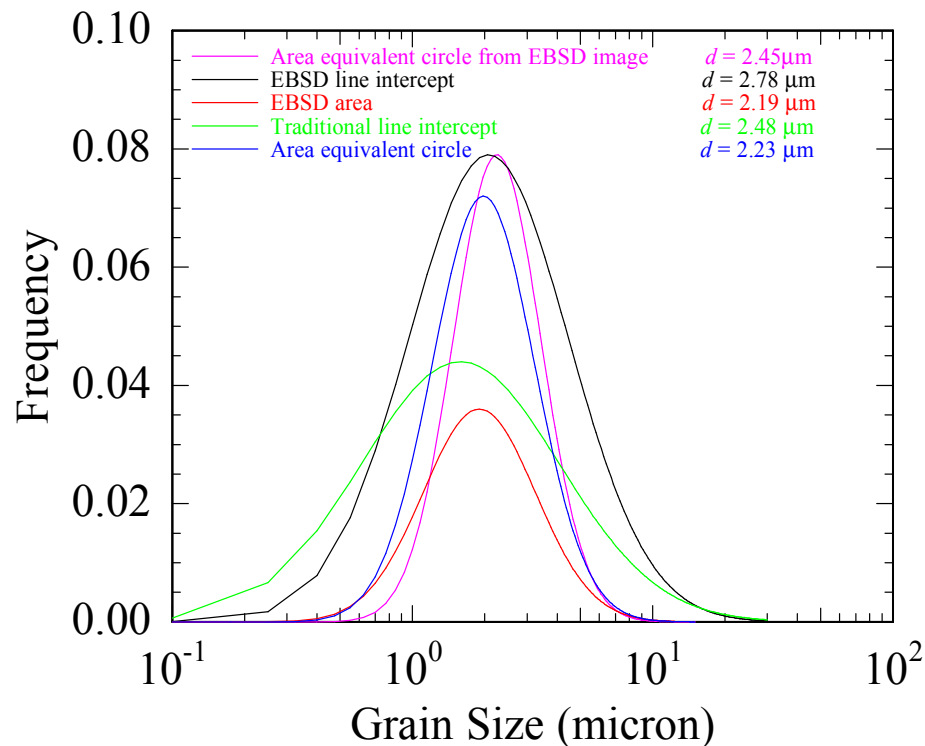


Figure 6. Comparison grain size distributions for three different fitting methods for determining grain size of an undoped sample of Fo. The lines represent log-normal fits to the different grain size distributions. Note that all of the methods produce similar values, with the line intercept methods being the highest.

(Mullins, 1957). Negligible grain growth occurs during this heating (Hiraga et al., 2010).

Samples were imaged with either a scanning electron microscope for those with very small grains or with an optical microscope for those with larger grains. After grain boundaries were hand traced in Inkscape, the grain boundary map was analyzed using ImageJ software. Although grain boundaries are at least a pixel wide in this method, no correction was made to the area to account for this width. The difference in area for grains $<1 \mu\text{m}$ in diameter, if corrected for this grain boundary width, could be as high as 5% of the total area, but for most grains it is $< 1\%$. To eliminate the small 'grains' that are merely artifacts of the tracing process, grains below 200 nm in diameter were eliminated, after a visual correlation revealed that many of these grains were being counted even though no grain existed in the image. The undoped-Fo samples exhibited a typical log normal grain size distribution, with a mean of $\sim 0.8 \mu\text{m}$ before deformation and $\sim 1 \mu\text{m}$ after deformation. A micrograph of a sample of undoped Fo, as well as the traced grain boundaries and the ImageJ grain outline map, are displayed in Figure 7. A similar series of images for a sample doped with Pr is presented in Figure 8.

Praseodymium-doped samples had slightly smaller grain sizes than the undoped-Fo samples. Calcium-doped samples experienced abnormal grain growth during deformation experiments, leading to a bimodal distribution of grain sizes. The micrograph of the fine-grained region of a Ca-doped sample is displayed in Figure 9 with the traced grain boundary image and the ImageJ outline. In addition, a vertical transect

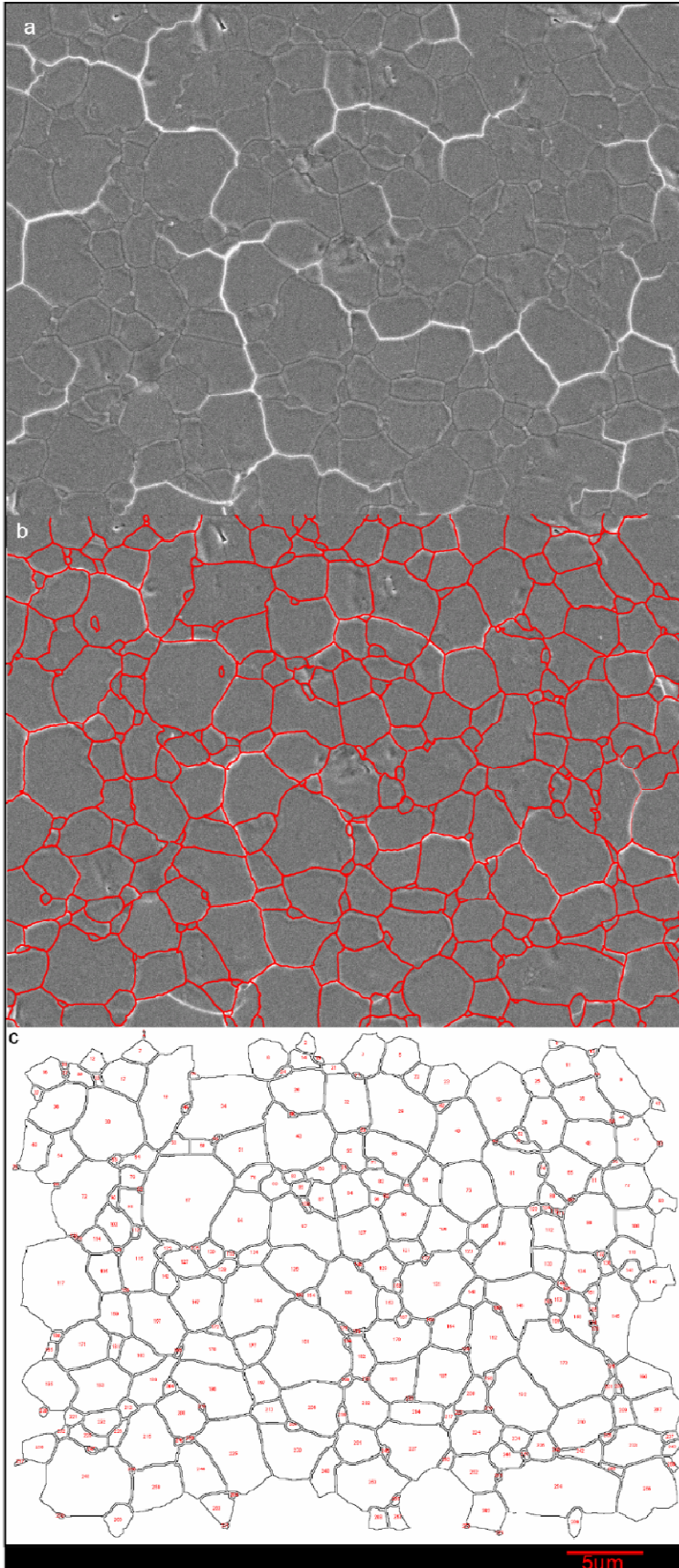


Figure 7.

a) Secondary-electron micrograph of undoped-Fo sample (Fo4). After it was polished, this sample was thermally etched to reveal the grain boundaries. The white lines result from charging effects due to the thin carbon coat not covering the most deeply grooved grain boundaries and fractures. b) Hand-traced grain boundaries. c) Outline of grains analyzed in Image J. This program calculates the area of each grain entirely bounded by red. Edge grains are discarded.

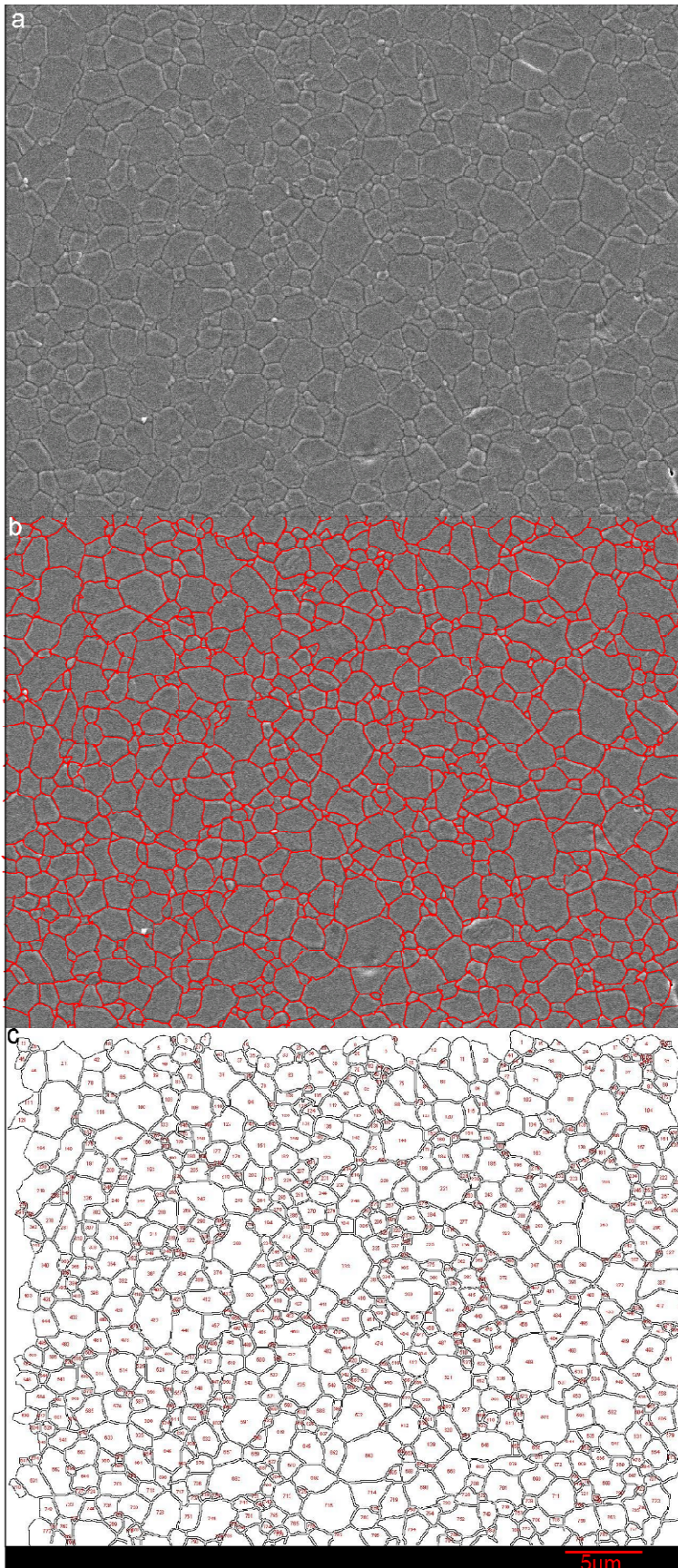


Figure 8.
a) Secondary-electron micrograph of a Pr-doped Fo sample (Pr8). After it was polished, this sample was thermally etched to reveal the grain boundaries. b) Hand-traced grain boundaries. c) Outline of grains produced in ImageJ.

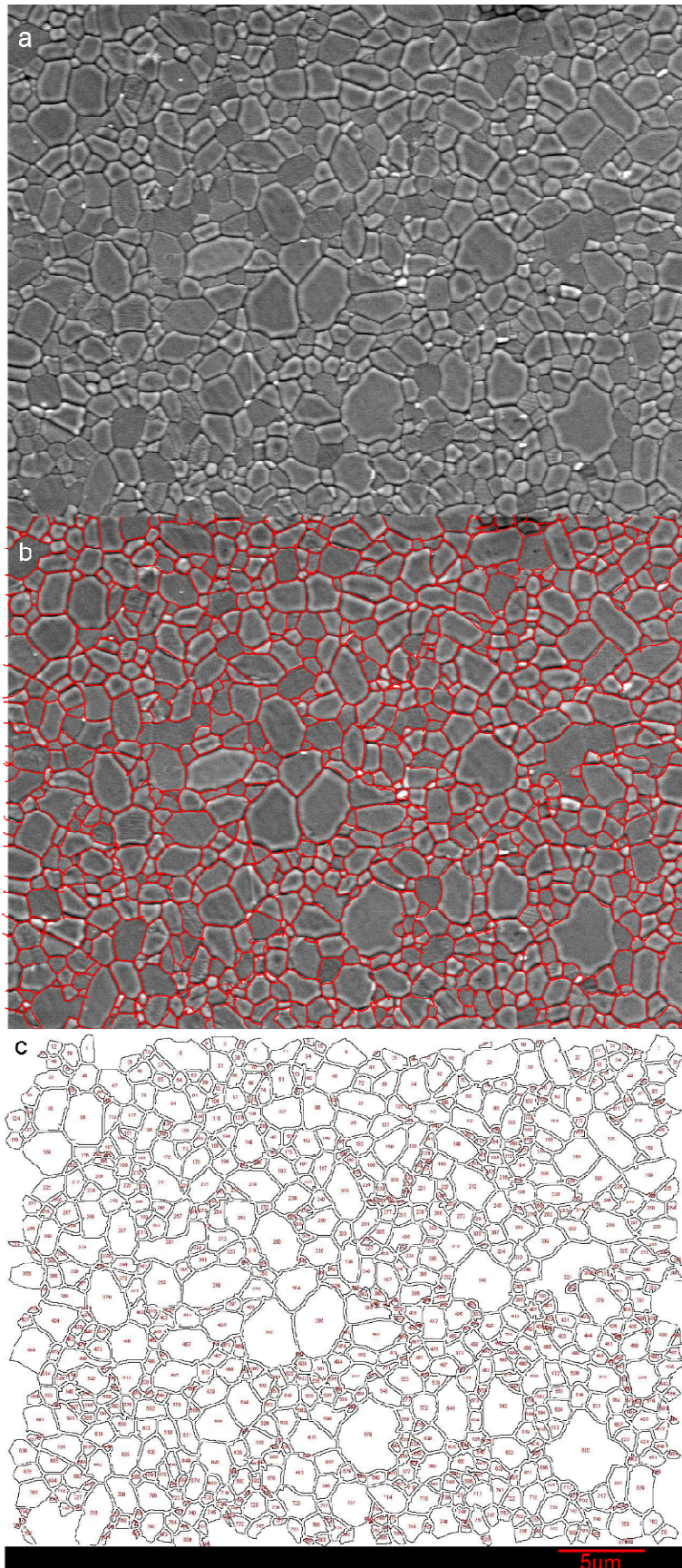
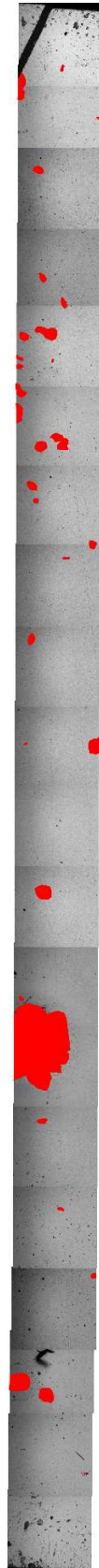


Figure 9

a) Secondary-electron micrograph of a Ca-bearing sample (Ca4). After it was polished, this sample was thermally etched to reveal the grain boundaries. b) Hand-traced grain boundaries. c) Outline of grains produced in ImageJ. d) Vertical transect of this sample with abnormally large grains filled in. This image was stitched together from several reflected-light optical micrographs.



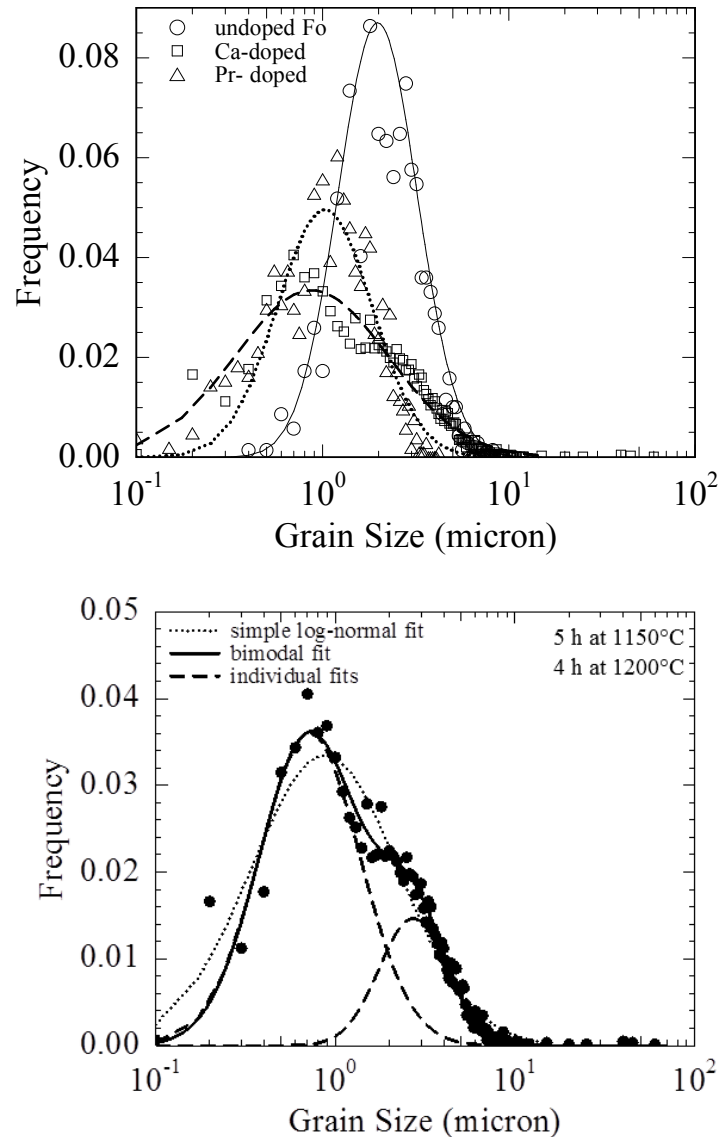


Figure 10. (top) Log-normal fits to grain size distributions for undoped, Pr-doped and Ca-doped Fo. The Pr-doped samples tend to have smaller grain sizes than the undoped samples. The Ca-doped sample grain sizes can be fit with a single log-normal line without significant error, although it actually has 3 distinct peaks, at $\sim 0.7 \mu\text{m}$, $\sim 2 \mu\text{m}$, and $\sim 40 \mu\text{m}$. (bottom)

of one of the Ca-doped samples is included, with the abnormal grains colored in. A

comparison of the different sample grain size distributions is presented in Figure 10.

The undoped Fo sample and the Pr-doped sample both show simple log-normal

distributions, with the Pr-doped sample grain sizes a bit smaller. The Ca-doped sample

grain sizes can be fit with a single log-normal function, but this fit masks the multiple peaks in the grain size distribution. The grain sizes reported for the Ca-doped samples do not include the abnormally large grains. The cut off was determined from the histogram of the small grains. All grains larger than the main group of grains were not considered.

3.6 Grain Growth

Grain growth is driven by minimizing the total energy associated with grain boundaries. To limit the growth of forsterite grains during deformation experiments, all the samples were vacuum sintered at 1400°C for 5 h. This anneal allowed grains to quickly grow from $\ll 1 \mu\text{m}$ to an average of $\sim 1 \mu\text{m}$. The slower kinetics at the temperatures of deformation ($\leq 1250^\circ\text{C}$), coupled with the decreased driving force of fewer grain boundaries, did limit the amount of grain growth that occurred. Nonetheless, grain growth still occurred during deformation, such that we needed to extrapolate to obtain the relevant grain size during the course of the experiment based on the grain growth law described below. Grain size was measured before and after deformation and, in order to calculate the grain sizes in between, a power-law grain growth model was used:

$$d_t^s - d_0^s = kt, \quad (3)$$

where d_t is the grain size at time t , d_0 is the grain size at $t = 0$, s is the grain growth exponent, and k is the grain growth parameter, which is temperature dependent.

Different values for s have been suggested for olivine. Karato et al. (1989) used $s = 2$ to

fit grain growth of samples fabricated from natural San Carlos olivine. Hiraga et al. (2010) fit grain growth data for high-purity samples of synthetic forsterite + enstatite with different values of s . Grain growth results for the samples with an enstatite fraction of 0 fit best with $s = 9$; however, they later fit their entire data set with $s = 4$, which matches their samples with an enstatite fraction of ~ 0.03 . As the synthetic forsterite used in this study was fabricated in the same way as used in Hiraga et al. (2010) and has a small amount of enstatite, we used a value of $s = 4$ in the grain growth law in Eq. (3).

To calculate the grain size at the beginning of each stress step, for each temperature and for each type of sample, a value of k was calculated based on the grain size before and after the deformation experiment combined with the elapsed time. For undoped Fo, k has values of 1.8×10^{-4} , 1.2×10^{-4} , 8.9×10^{-4} , and $2.1 \times 10^{-4} \mu\text{m}^4/\text{s}$ for temperatures of 1100° , 1150° , 1200° , and 1250°C , respectively. The pre- and post-deformation grain sizes for the experiment performed at 1000°C were indistinguishable. For the Ca-doped samples, k has similar values: 5.1×10^{-5} , 1.1×10^{-5} , 1.6×10^{-4} , and $2.1 \times 10^{-4} \mu\text{m}^4/\text{s}$ for the respective temperatures. For the Pr-doped samples, k had smaller values: 3.1×10^{-5} , 1.39×10^{-5} , 4.25×10^{-5} , and $7.8 \times 10^{-5} \mu\text{m}^4/\text{s}$ for the respective temperatures. The similarity of the values of k for Ca-doped and undoped samples indicates that there is not a large pinning effect due to cation size, while the difference in the values of k for the Pr-doped and Ca-doped/undoped samples indicates that the difference in point

defect concentration on the grain boundaries due to charge difference of Pr slightly inhibits grain growth.

The majority of the volume of the Ca-doped samples remained fine grained throughout the deformation experiment. However, the most striking feature of the Ca-doped samples was the abnormally large grains that grew during the course of the deformation experiment. Similar grain growth was observed in Ca-doped alumina (Dillon & Harmer 2008) for which a correlation was observed between grain size and grain growth rate, with the mm-sized grains growing at roughly 10x the rate as the ~100

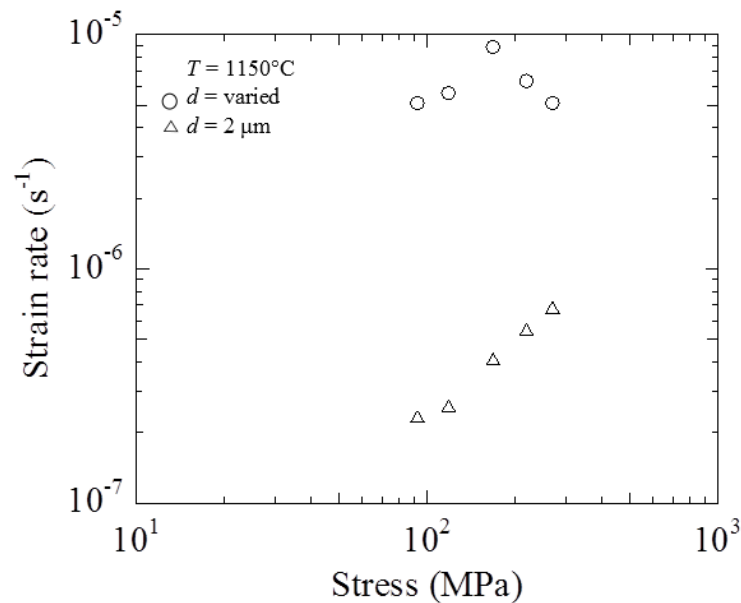


Figure 11. Creep data from Ca-doped sample (Ca4) deformed at 1100°C without any grain size normalization. The experiment was conducted starting at low stress and moving to high stress, so that the data points are in the order in which they were collected from left to right. The initial data points show typical stress-strain rate behavior, with an increase in stress resulting in an increase in strain rate. The later data points show opposite behavior, as an increase in stress results in a decrease in strain rate.

μm grains. This grain growth was evident in the mechanical data, as illustrated in Figure 11 for a Ca-doped sample deformed at 1100°C . In experiments on Ca-doped samples, at some point in the experiment an increase in the stress applied to the rock resulted in a slower deformation rate than occurred for the previous step. This transition point did not seem to correlate with a specific stress or time in the experiment. However, abnormally large grains were present in all Ca-doped samples after deformation. Some of the large grains were surrounded by the fine-grained matrix, while others appeared in clusters, with each large grain in the cluster seeming to grow out from a central point. Micrographs illustrating examples of each are presented in Figure 12. In Figure 12b, a number of small olivine grains, outlined in red, occur within the abnormally large olivine grain. Grain growth is so rapid that some small forsterite grains are surrounded by, and not made a part of, the large grain. As time goes on, grain boundary migration incorporates the small interior olivine grains into the large grain. This feature is common to most of the abnormally large grains, even the large grains in Figure 12a encapsulated a few small grains. A number of small grains exist within the large grain, but the centers of the larger grains are free of small isolated grains. Note that the abnormally large grains in Figure 12 are in fact small compared to the largest grains in each sample. The SEM image in Figure 13 of a Ca-doped sample (Ca6) demonstrates the scale of the largest grains. This image actually includes a group of grains, rather than a single grain; the damage due to polishing in the center of this cluster made it impossible

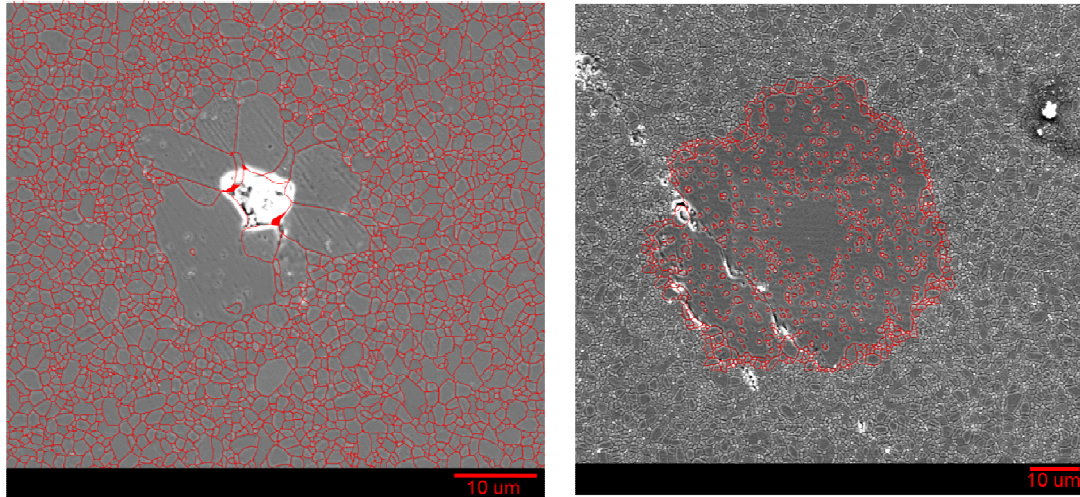


Figure 12. Secondary electron images of abnormally large grains in Ca-doped Fo. (a) Cluster of abnormally large grains in sample Ca4. (b) Isolated abnormally large grain in sample Ca5. There are a number of small grains, also outlined, which reside inside the large grain. These are also forsterite grains which were surrounded by the rapid growth of the large grain.

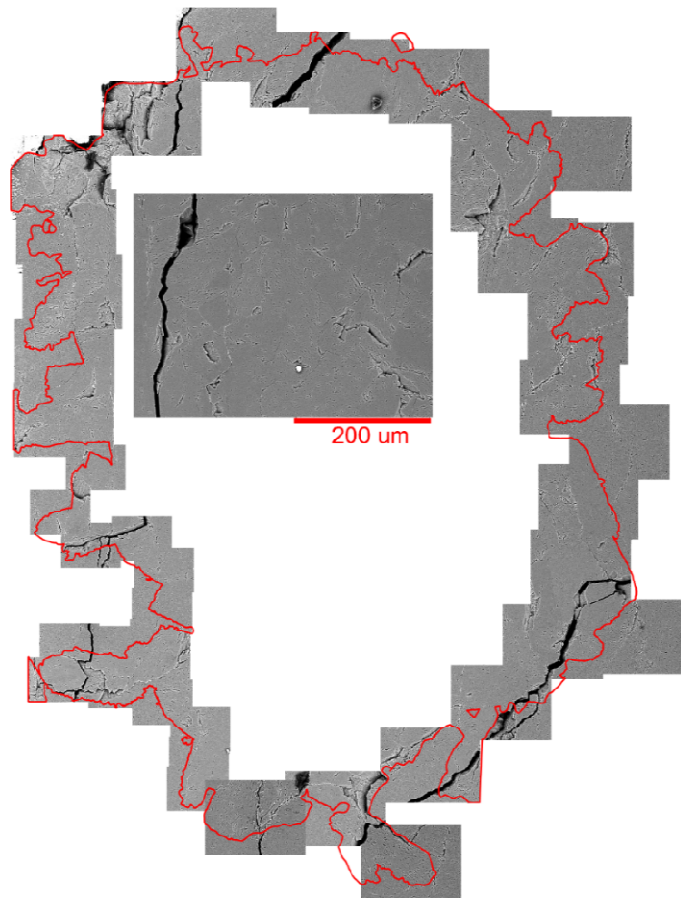


Figure 13.
Conglomerate of
abnormally large grains
(Ca6).

to trace the grain boundaries separating them. All but the smallest of the abnormally grown grains in this cluster are larger than the large grains shown in Figure 12.

3.7 Normalizing Creep Data to Common Grain Size

Grain size is an important variable in determining the strength of a rock deforming by diffusion creep. In the flow law for diffusion creep, the strain rate, $\dot{\epsilon}$, depends inversely on grain size, d , to a power p , and linearly stress, σ :

$$\dot{\epsilon} \propto \frac{\sigma^n}{d^p}, \quad (4)$$

with the stress exponent $n = 1$ for diffusion creep. The grain size of these samples does not vary over a large enough range to independently obtain a grain size exponent. A value of $p = 2$ applies if diffusion is through grain interiors, and a value of $p = 3$ applies if diffusion is along grain boundaries. Since previous studies on synthetic olivine (Tasaka et al., 2013; Faul and Jackson, 2007), as well as natural olivine (Hirth and Kohlstedt, 1995) obtained a value for the grain size exponent of $p = 3$ for samples deformed under similar conditions of fine grain size ($<5 \mu\text{m}$), moderate stress, and high temperature, $p = 3$ was used to analyze data from our experiments. To double check this assumption, we calculate the Nabarro-Herring creep rate for $2 \mu\text{m}$ grains deforming at 1200°C and 100 MPa . For Nabarro-Herring creep (Nabarro, 1948; Herring, 1950), the strain rate is given by

$$\dot{\epsilon}_{NH} = 14 \left(\frac{V_m \sigma}{RT} \right) \frac{D_{gm}}{d^3}, \quad (5)$$

where V_m is the molar volume, R is the ideal gas constant, T is temperature, and D_{gm} is the diffusion coefficient through the grain matrix. Using $D_{gm} = 10^{-19} \text{ m}^2 \text{ s}^{-1}$ (Fei et al., 2012), and $V_m = 4.3 \times 10^{-5} \text{ m}^3/\text{mol}$ (Akaogi et al., 1989), $\dot{\epsilon}_{NH} = 1 \times 10^{-7} \text{ 1/s}$. Therefore, grain boundary diffusion must dominate, as this calculated value is over an order of magnitude slower than the experiments.

To compare our experimental results for different sample compositions, data were normalized to a single grain size of $2 \mu\text{m}$ using the relationship

$$\dot{\epsilon}_{gsn} = \dot{\epsilon}_{measured} * \left(\frac{d}{2}\right)^3. \quad (6)$$

The subscript *gsn* indicates a value that has been grain size normalized. Traditionally, the average grain size obtained from a grain size distribution is used to normalize the data set. However, this approach, particularly for the Ca-doped samples, does not taken into account the bimodal nature of its grain size distribution illustrated in Figure 10. Thus, the stress or strain rate were apportioned into bins by grain size, and individually normalized to $2 \mu\text{m}$ in two ways: a uniform stress limit (Sachs model) and a uniform strain rate limit (Taylor model).

The Sachs model assumes that, for samples deformed in compression, the grains lie in horizontal layers, segregated by grain size. For each layer, an area, A_i , is calculated:

$$A_i = f_i * \pi * \left(\frac{d_i}{2}\right)^2, \quad (7)$$

where d_i is the grain size of the layer and f_i is the number of grains of the i^{th} layer. This quantity is converted to a height, h_i , by dividing by a width common to all the layers,

w_{layer} :

$$h_i = A_i / w_{layer} . \quad (8)$$

In this analysis, the flow law parameters of interest are σ and d . For the i^{th} layer, the strain rate, $\dot{\epsilon}_i$, is given by

$$\dot{\epsilon}_i = \frac{C\sigma}{d_i^3} . \quad (9)$$

All other terms, such as temperature and pressure dependence, are contained in the parameter, C . This strain rate for each layer is then converted to displacement rate, $\dot{\Delta}_i$, of that layer using the relation

$$\dot{\Delta}_i = \dot{\epsilon}_i * h_i , \quad (10)$$

from which the total displacement rate measure for the sample, $\dot{\Delta}_{tot}$, is calculated as

$$\dot{\Delta}_{tot} = \sum \dot{\Delta}_i = \sum \frac{C\sigma h_i}{d_i^3} \quad (11)$$

and apportioned to each layer:

$$\dot{\Delta}_i = \frac{\dot{\Delta}_{tot}}{\sum \frac{h_i}{d_i^3}} * \frac{h_i}{d_i^3} . \quad (12)$$

To normalize to a common grain size of 2 μm , the displacement rate of each layer was corrected using the relation

$$\dot{\Delta}_{i,gsm} = \dot{\Delta}_i * \left(\frac{d_i}{2}\right)^3 . \quad (13)$$

These displacement rates were then summed and divided by the total height of the sample to create the grain size normalized strain rate:

$$\dot{\epsilon}_{tot,gsm} = \dot{\Delta}_{tot,gsm} / h_{tot} = (\sum \dot{\Delta}_{i,gsm}) / h_{tot} . \quad (14)$$

The Taylor model assumes that the sample is composed of vertical columns, each of different grain size for compressive deformation. A width for each column is

calculated in the same manner as height for the uniform stress orientation. This orientation normalizes stress for grain size to determine the stress that would be necessary to deform the rock if all the columns had a grain size of 2 μm . The method has a similar approach as the uniform stress orientation. First, a width, w_i , for each column of grain size was defined, by dividing by a uniform height of all the columns:

$$w_i = A_i / h_{\text{column}} \quad (15)$$

This width converts the stress acting on each column into a force acting on the column,

$$F_i = \sigma_i * w_i, \quad (16)$$

with the sum of the forces on the columns to equal the applied force:

$$F_{\text{applied}} = \sum F_i = \sum C \sigma w_i d_i^3. \quad (17)$$

The force apportioned onto each column is then determined from the width of the column, the binned grain size for the column, and summation of these values from all the columns:

$$F_i = \frac{F_{\text{applied}}}{\sum w_i d_i^3} * w_i d_i^3. \quad (18)$$

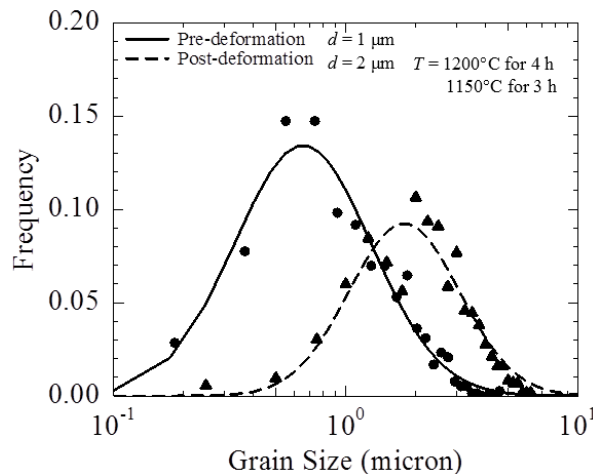


Figure 14: Comparison of a pre-deformation grain size distribution with a grain size of 1 μm , and a post deformation grain size distribution with a grain size of 2 μm .

Grain size is normalized to 2 μm for each of these columns from the binned value:

$$F_{i,gsn} = F_i * \left(\frac{2}{\bar{d}_i}\right)^3. \quad (19)$$

The forces are then summed and divided by the total width of the sample to create the grain size normalized stress value:

$$\sigma_{tot,gsn} = F_{tot,gsn}/w_{tot} = (\sum F_{i,gsn})/w_{tot}. \quad (20)$$

Grain size distributions could be measured only before and after deformation, for each experiment. Although not entirely accurate, the assumption is made that the distribution is self-similar throughout the experiment, with only the position of the peak changing with time. However, as demonstrated in Figure 14, the change in the shape of the distribution is not large. The initial load step uses the pre-deformation grain size distribution, and for subsequent stress steps, the grain size of each bin is scaled by the ratio of the average initial grain size and the average grain size calculated for each step.

For the Ca-doped samples, which do not have a simple log-normal distribution, a slightly different approach was used. The abnormally large grains were assumed not to deform; thus the values calculated in Eq. (12) and Eq. (18) for those bins are set to 0.

In the plot of strain rate versus stress in Figure 15, the results of applying these methods are compared on a dataset obtained on an undoped sample. Included in this figure with the raw strain rate versus stress data are the data corrected in the uniform strain rate orientation, the data corrected in the uniform stress orientation, and the data normalized using the average grain size. The strain rate of the sample decrease with time due to grain growth. For this experiments in which the load steps were taken

from low to high load, the raw data plot nearly horizontally with an apparent stress exponent of ~ 0.1 . The traditional grain size normalization corrects the strain rate for this grain growth and results in a slope much of $n = 0.86$. The data obtained from the uniform stress orientation correction plots almost on top of the traditional normalization with a similar slope. The data corrected with the uniform strain rate orientation has a slope of $n = 0.25$, which is an improvement over 0.1, but still far from the ideal of $n = 1$ for diffusion creep. As the only variable in these experiments that could result in a small value of n is increasing grain size, a slope of $n < 1$ indicates that the creep data were not fully corrected for grain growth.

The different correction methods lead to very different interpretations of the data. The marked difference between the result of the Sachs model and the Taylor or traditional models, as well as the inability of it to correct for grain growth, indicate that the uniform strain rate bound is not appropriate. The choice falls between the traditional and the

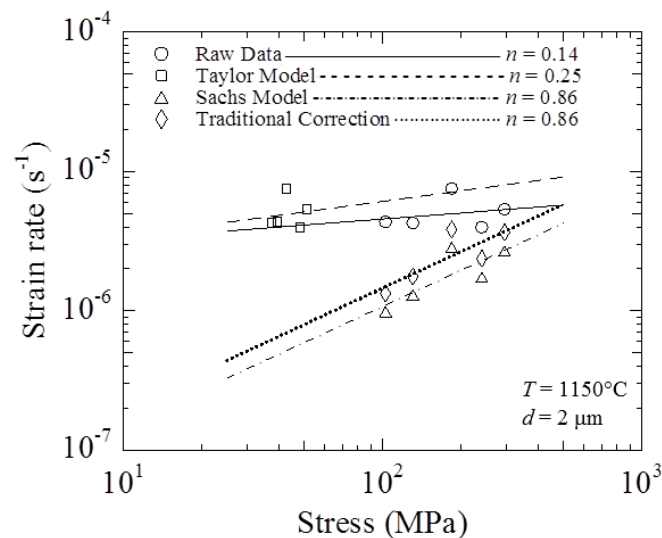


Figure 15. Effect on creep data of three different methods for normalizing grain size. Grain size was normalized to $2 \mu m$.

uniform stress orientation methods, which produce very similar creep strengths and values of n . Although the traditional method allows for a wider comparison of data, the ability to account for different grain size distributions is preferred as it allows for correction of samples with a bimodal grain size distribution. Thus, all data in the subsequent analyses are corrected using the uniform stress orientation method.

3.8 Discussion

Except for the highest temperature condition for the Pr-doped samples, our experiments were primarily carried out in the diffusion creep regime. In Figure 16, mechanical data from samples of undoped Fo, summarized in Table 1, are plotted for five temperatures, both allowing n to vary (Figure 16a) and fixing $n = 1$ (Figure 16b). In the first case, the stress exponent does not vary significantly from $n = 1$, demonstrating that the undoped samples deformed in the diffusion creep regime in all our experiments. A similar comparison is shown in Figure 17 for Ca-doped samples and Figure 18 for Pr-doped samples. Mechanical data for the Ca doped samples are summarized in Table 2, and the mechanical data for Pr-doped samples in Table 3. The stress exponent for the Ca-doped samples also does not vary significantly from $n = 1$, again indicating deformation by diffusion creep. The Pr-doped samples, however, show markedly different behavior. At 1250°C, the stress exponent for the Pr-doped samples closer is to 3 than to 1, indicating a significant contribution from a dislocation-dependent creep mechanism.

The strengths of the doped samples are compared to those of the undoped samples at various temperatures in Figure 19 (n allowed to vary) and

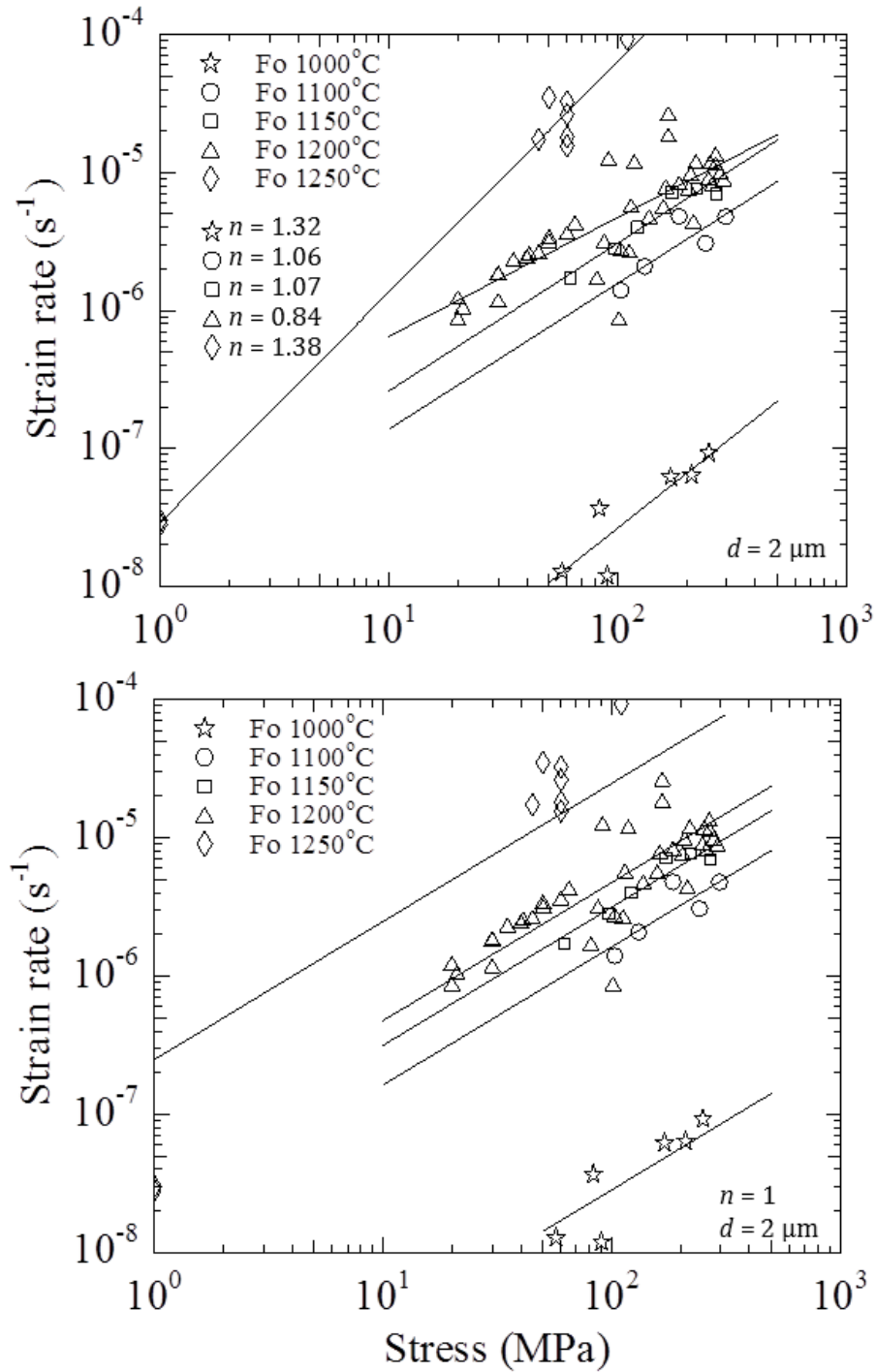


Figure 16.

Comparison of non-linear least-squares fits of creep data for an undoped-Fo sample. This sample was deformed at five temperatures. Top) Stress exponent allowed to vary. Bottom) Stress exponent fixed at $n = 1$

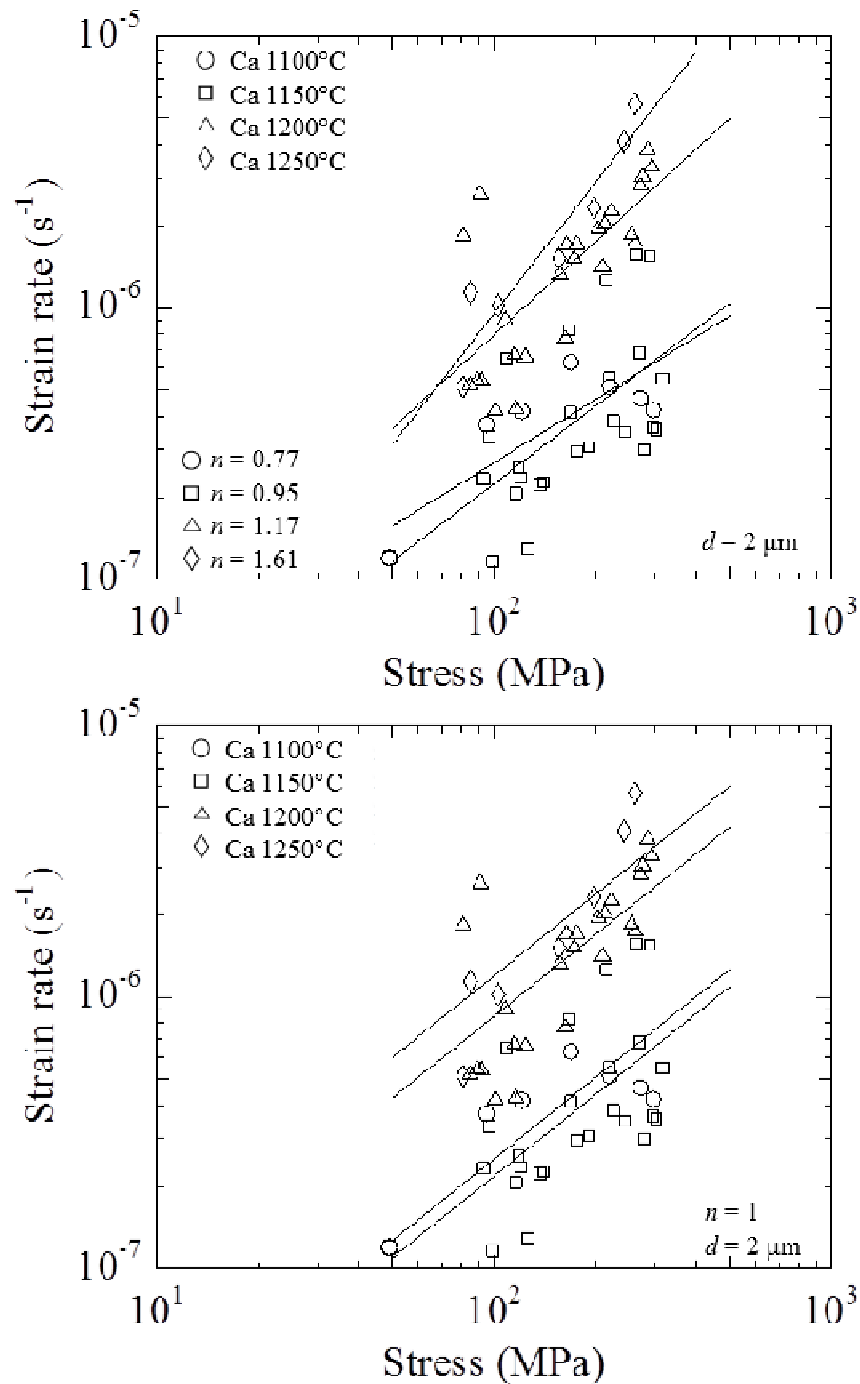


Figure 17.

Comparison of non-linear least-squares fits of creep data for Ca-doped samples deformed at four temperatures. Top) Stress exponent allowed to vary. Bottom) Stress exponent fixed at $n = 1$.

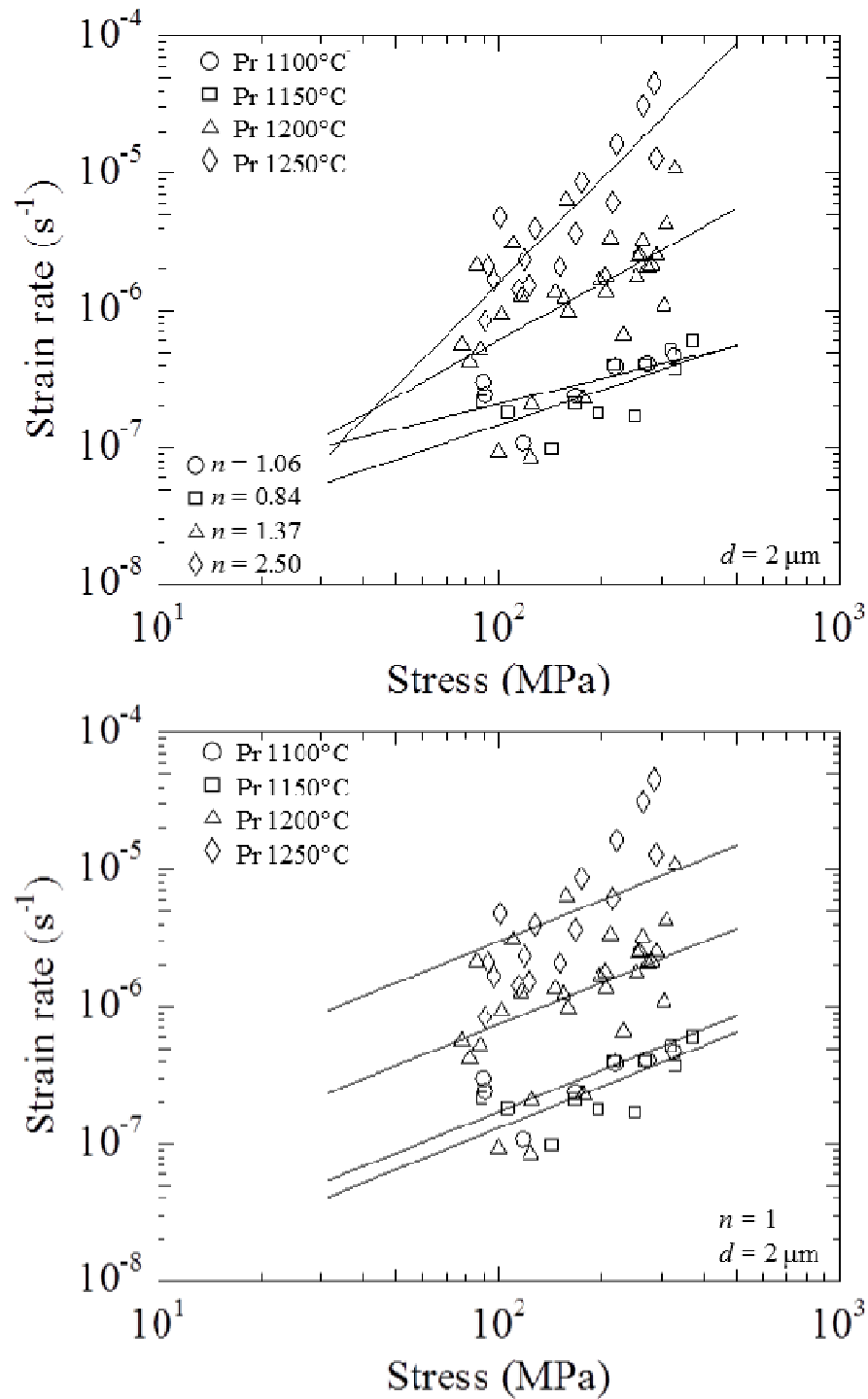


Figure 18.

Comparison of non-linear least-squares fits of creep data for Pr-doped samples deformed at four temperatures. Top) Stress exponent allowed to vary. Bottom) Stress exponent fixed at $n = 1$.

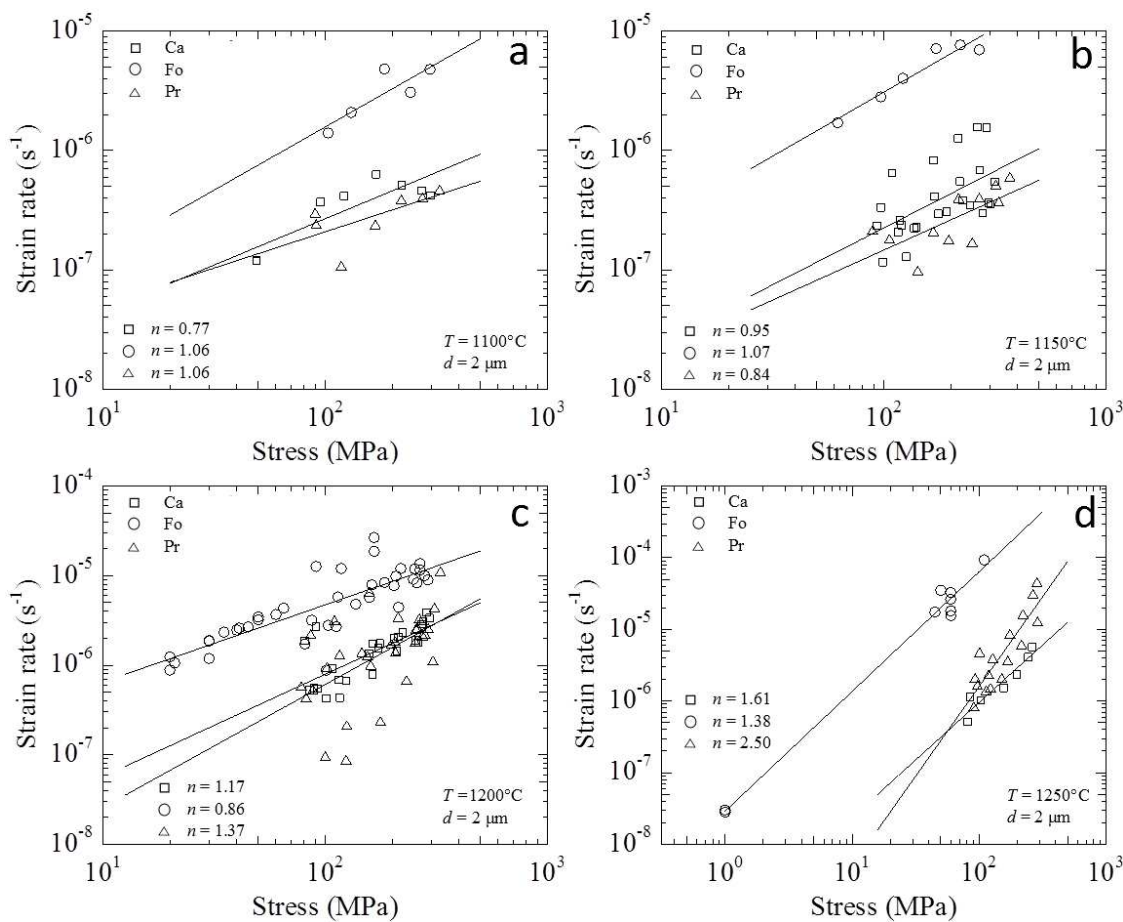


Figure 19. Compilation of deformation data for samples of undoped Fo, Ca-doped Fo, and Pr-doped Fo, all normalized to a grain size of $2 \mu m$. Data are plotted for four temperatures: a) $1100^{\circ}C$, b) $1150^{\circ}C$, c) $1200^{\circ}C$, and d) $1250^{\circ}C$. The stress exponent, n , was allowed to vary.

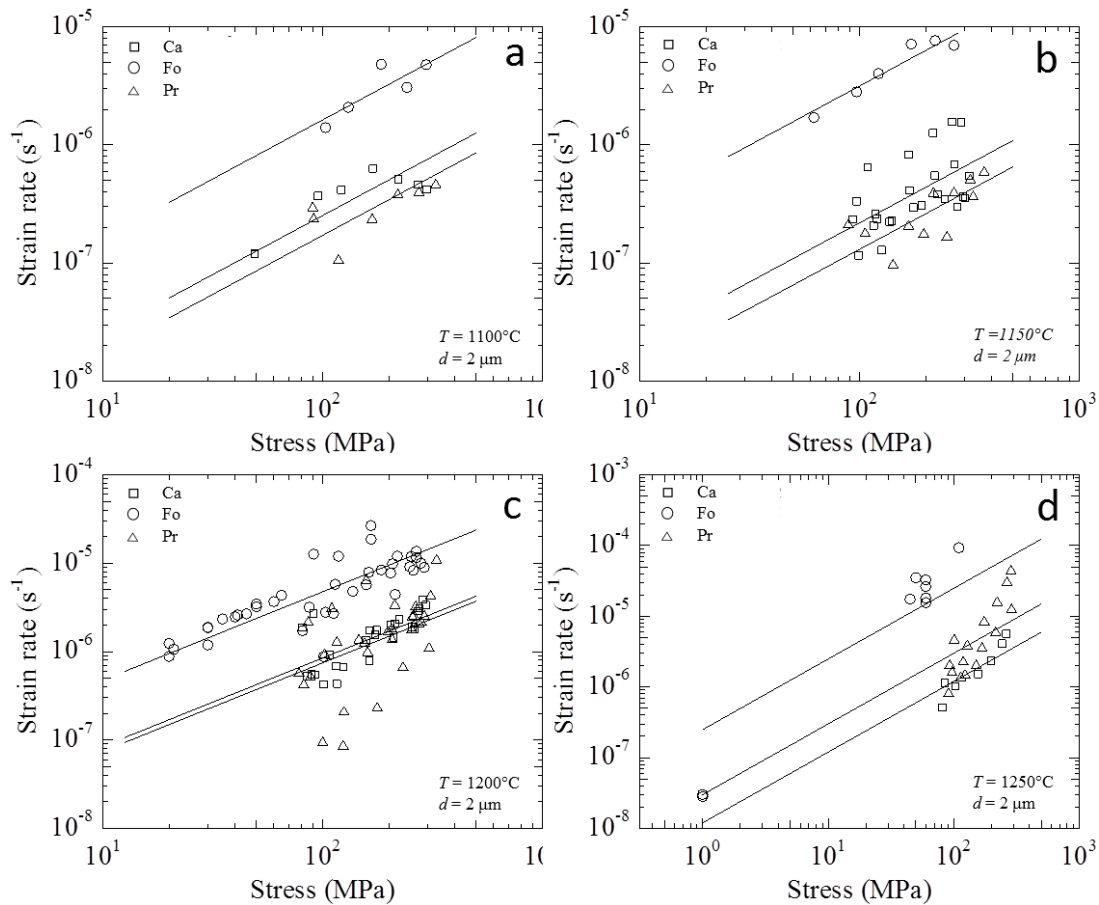


Figure 20. Compilation of deformation data for samples of undoped Fo, Ca-doped Fo, and Pr-doped Fo. Data are plotted for four temperatures: a) $1100^{\circ}C$, b) $1150^{\circ}C$, c) $1200^{\circ}C$, and d) $1250^{\circ}C$. The stress exponent was fixed at $n = 1$

Table 1: Summary of undoped Fo mechanical data

Experiment	Temperature (°C)	Stress (MPa)	Strain rate (1/s)	Normalized Strain Rate (1/s)	Strain (%)	Grain Size (μm)
5-1	1250	1	9.41E-08	2.81E-08	0.80	1.48
5-2	1250	1	8.93E-08	3.00E-08	0.50	1.54
7-1	1250	60	2.75E-06	1.56E-05	1.12	3.95
7-2	1250	60	2.46E-06	3.26E-05	0.94	5.24
9-1	1250	60	1.27E-06	2.63E-05	1.12	6.08
10-2	1250	45	7.73E-07	1.74E-05	1.00	6.26
10-2	1250	60	8.01E-07	1.81E-05	0.50	6.26
14-1	1250	50	1.61E-05	3.51E-05	3.00	2.87
15-1	1250	110	4.91E-05	9.30E-05	2.10	2.74
1475	1200	65	6.36E-06	4.34E-06	1.03	1.95
	1200	114	8.45E-06	5.77E-06	0.92	1.95
	1200	162	1.16E-05	7.91E-06	1.13	1.95
	1200	208	1.44E-05	9.87E-06	1.34	1.95
	1200	253	1.75E-05	1.19E-05	1.56	1.95
1558	1200	103	3.90E-06	2.79E-06	1.43	1.98
	1200	137	5.63E-06	4.81E-06	1.17	2.10
	1200	185	9.01E-06	8.37E-06	1.53	2.16
	1200	214	4.46E-06	4.44E-06	1.32	2.21
	1200	259	7.79E-06	8.32E-06	1.37	2.26
	1200	280	8.86E-06	1.00E-05	1.30	2.31
	1200	101	7.41E-07	8.78E-07	0.30	2.34
1522	1200	91	1.78E-05	1.27E-05	1.37	1.98
	1200	118	1.65E-05	1.20E-05	1.36	1.99
	1200	166	3.61E-05	2.67E-05	1.46	2.00
	1200	166	2.50E-05	1.87E-05	0.65	2.01
	1200	219	1.59E-05	1.20E-05	1.67	2.02
	1200	267	1.50E-05	1.16E-05	1.46	2.03
	1200	290	1.14E-05	8.95E-06	1.36	2.04
	1200	87	3.61E-06	3.18E-06	1.68	2.12
	1200	112	2.92E-06	2.70E-06	0.70	2.16
	1200	158	5.90E-06	5.69E-06	1.01	2.19
	1200	204	7.70E-06	7.72E-06	1.43	2.22
	1200	249	8.77E-06	9.11E-06	1.51	2.24
	1200	267	1.28E-05	1.36E-05	1.54	2.26
	1200	81	1.59E-06	1.72E-06	1.66	2.27

Table 1 continued: Summary of undoped Fo mechanical data

Experiment	Temperature (°C)	Stress (MPa)	Strain rate (1/s)	Normalized Strain Rate (1/s)	Strain (%)	Grain Size (μm)
GBSFo3	1200	20	5.87E-08	1.24E-06		6.13
	1200	30	7.24E-08	1.86E-06		6.54
	1200	40	8.52E-08	2.47E-06		6.81
	1200	50	9.97E-08	3.21E-06		7.05
	1200	21	2.90E-08	1.06E-06		7.36
	1200	30	4.89E-08	1.88E-06		7.47
	1200	45	7.02E-08	2.68E-06		7.46
	1200	35	5.56E-08	2.34E-06		7.71
	1200	41	6.00E-08	2.60E-06		7.78
	1200	50	7.64E-08	3.45E-06		7.89
	1200	60	7.75E-08	3.67E-06		8.01
GBSFo2	1200	20	3.83E-08	8.82E-07		6.30
	1200	30	4.27E-08	1.19E-06		6.71
1475	1150	62	5.30E-06	1.71E-06	1.01	1.52
	1150	97	6.56E-06	2.81E-06	1.20	1.67
	1150	122	7.72E-06	4.02E-06	1.50	1.78
	1150	172	1.17E-05	7.16E-06	1.64	1.88
	1150	221	1.16E-05	7.66E-06	1.66	1.93
	1150	269	9.79E-06	6.97E-06	1.81	1.98
1478	1100	103	4.33E-06	1.40E-06	0.94	1.52
	1100	131	4.26E-06	2.08E-06	1.68	1.75
	1100	185	7.52E-06	4.81E-06	3.20	1.91
	1100	242	3.97E-06	3.07E-06	5.43	2.03
	1100	296	5.34E-06	4.78E-06	6.59	2.13
1461	1000	57	2.89E-07	1.27E-08	0.11	0.78
	1000	90	2.72E-07	1.19E-08	0.10	0.78
	1000	170	1.41E-06	6.18E-08	0.27	0.78
	1000	210	1.46E-06	6.38E-08	0.29	0.78
	1000	250	2.11E-06	9.21E-08	0.40	0.78
	1000	83	8.34E-07	3.65E-08	0.65	0.78

Table 2: Summary of Ca-doped Fo mechanical data

Experiment	Temperature (°C)	Stress (MPa)	Normalized Strain Rate (1/s)	Strain (%)	Grain Size (μm)
1548	1250	85	1.14E-06	0.66	1.51
	1250	103	1.02E-06	0.58	1.53
	1250	156	1.52E-06	0.99	1.55
	1250	198	2.34E-06	1.24	1.57
	1250	243	4.10E-06	1.44	1.59
	1250	262	5.65E-06	1.46	1.60
	1250	81	5.12E-07	1.05	1.61
1544	1200	92	5.46E-07	0.93	1.25
	1200	115	6.85E-07	0.99	1.30
	1200	164	1.74E-06	1.40	1.33
	1200	213	2.07E-06	1.82	1.35
	1200	262	1.78E-06	1.42	1.37
	1200	286	3.89E-06	1.41	1.38
	1200	81	1.87E-06	1.12	1.41
	1200	108	9.18E-07	0.31	1.44
	1200	157	1.35E-06	0.45	1.47
	1200	204	1.99E-06	0.71	1.49
	1200	89	5.51E-07	0.00	1.26
1533	1200	116	4.33E-07	0.49	1.30
	1200	163	7.85E-07	0.72	1.33
	1200	210	1.44E-06	0.97	1.36
	1200	256	1.89E-06	1.03	1.38
	1200	276	3.10E-06	1.09	1.40
	1200	85	5.29E-07	0.49	1.41
	1200	176	1.75E-06	3.17	1.31
1552	1200	101	4.27E-07	0.71	1.34
	1200	124	6.71E-07	0.54	1.38
	1200	173	1.55E-06	0.95	1.41
	1200	223	2.32E-06	1.01	1.44
	1200	272	2.86E-06	1.29	1.46
	1200	294	3.37E-06	1.04	1.48
	1200	91	2.68E-06	0.89	1.50

Table 2 continued: Summary of Ca-doped Fo mechanical data

Experiment	Temperature (°C)	Stress (MPa)	Normalized Strain Rate (1/s)	Strain (%)	Grain Size (μm)
1508	1150	93	2.34E-07	0.95	0.75
	1150	118	2.60E-07	1.27	0.75
	1150	169	4.12E-07	1.68	0.75
	1150	220	5.50E-07	1.57	0.75
	1150	270	6.84E-07	1.18	0.76
	1150	116	2.07E-07	0.78	0.76
1528	1150	140	2.27E-07	1.02	0.77
	1150	192	3.07E-07	1.61	0.79
	1150	244	3.49E-07	1.09	0.80
	1150	296	3.64E-07	0.81	0.81
	1150	316	5.49E-07	0.72	0.82
	1150	109	6.48E-07	0.70	0.83
	1150	137	2.23E-07	0.00	0.84
	1150	99	1.16E-07	0.26	0.75
1498	1150	126	1.29E-07	0.29	0.76
	1150	176	2.95E-07	0.85	0.77
	1150	226	3.83E-07	1.15	0.79
	1150	279	2.99E-07	1.19	0.80
	1150	302	3.54E-07	0.95	0.81
	1150	97	3.33E-07	0.22	1.53
1553	1150	120	2.36E-07	0.05	1.55
	1150	167	8.27E-07	0.08	1.56
	1150	216	1.26E-06	0.14	1.58
	1150	264	1.57E-06	0.27	1.60
	1150	290	1.55E-06	0.27	1.62
1468	1100	49	1.20E-07	0.34	0.75
	1100	95	3.71E-07	0.60	0.87
	1100	121	4.16E-07	1.17	0.89
	1100	169	6.31E-07	1.92	0.92
	1100	221	5.12E-07	1.71	0.95
	1100	272	4.62E-07	1.32	0.97
	1100	297	4.20E-07	0.67	1.00
	1100	49	1.19E-07	0.39	1.02

Table 3: Summary of Pr-doped Fo mechanical data

Experiment	Temperature (°C)	Stress (MPa)	Strain rate (1/s)	Normalized Strain Rate (1/s)	Strain (%)	Grain Size (μm)
1564	1250	101	3.86E-06	4.80E-06	0.58	1.48
	1250	128	3.19E-06	3.97E-06	0.75	1.48
	1250	175	6.97E-06	8.68E-06	0.92	1.48
	1250	222	1.32E-05	1.64E-05	0.95	1.48
	1250	266	2.51E-05	3.12E-05	1.14	1.48
	1250	286	3.66E-05	4.56E-05	1.24	1.48
1594	1250	93	1.65E-06	2.10E-06	0.63	1.50
	1250	119	1.84E-06	2.35E-06	0.68	1.50
	1250	168	2.87E-06	3.66E-06	1.06	1.50
	1250	216	4.80E-06	6.14E-06	1.05	1.50
	1250	289	1.01E-05	1.29E-05	1.06	1.50
	1250	91	6.53E-07	8.40E-07	0.45	1.50
1623	1250	114	1.10E-06	1.42E-06	0.30	1.51
	1250	97	1.35E-06	1.67E-06	2.31	1.47
	1250	123	1.22E-06	1.53E-06	1.67	1.48
1564	1250	151	1.66E-06	2.09E-06	1.42	1.49
	1200	78	1.54E-06	5.86E-07	0.42	1.47
	1200	102	2.51E-06	9.59E-07	0.41	1.47
	1200	155	3.35E-06	1.28E-06	0.68	1.47
	1200	206	4.87E-06	1.87E-06	0.96	1.47
	1200	256	6.65E-06	2.55E-06	0.95	1.48
1569	1200	281	5.78E-06	2.22E-06	0.96	1.48
	1200	116	6.39E-06	1.32E-06	1.35	1.20
	1200	146	6.75E-06	1.40E-06	0.99	1.20
	1200	198	8.36E-06	1.73E-06	1.91	1.20
	1200	260	1.27E-05	2.63E-06	1.74	1.20
	1200	310	2.11E-05	4.39E-06	2.26	1.20
1515	1200	330	5.37E-05	1.12E-05	1.23	1.20
	1200	86	1.36E-05	2.22E-06	1.21	1.11
	1200	110	1.92E-05	3.18E-06	1.23	1.12
	1200	158	3.99E-05	6.67E-06	0.91	1.12
	1200	213	2.06E-05	3.46E-06	0.80	1.12
	1200	265	1.97E-05	3.33E-06	0.82	1.12
1515	1200	290	1.52E-05	2.60E-06	1.13	1.13
	1200	88	2.59E-06	5.39E-07	1.12	1.20

Table 3 continued: Summary of Pr-doped Fo mechanical data

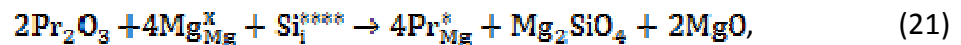
Experiment	Temperature (°C)	Stress (MPa)	Strain rate (1/s)	Normalized Strain Rate (1/s)	Strain (%)	Grain Size (μm)
1515	1200	160	4.81E-06	1.01E-06	0.90	1.21
	1200	207	6.68E-06	1.41E-06	1.05	1.21
	1200	254	8.60E-06	1.83E-06	1.27	1.21
	1200	274	1.01E-05	2.15E-06	1.27	1.21
	1200	82	2.03E-06	4.35E-07	1.09	1.21
1593	1200	100	2.47E-07	9.60E-08	0.20	1.48
	1200	125	5.50E-07	2.14E-07	0.28	1.48
	1200	177	6.05E-07	2.37E-07	0.42	1.49
	1200	232	1.74E-06	6.84E-07	0.62	1.49
	1200	305	2.84E-06	1.13E-06	0.75	1.49
	1200	124	2.21E-07	8.79E-08	0.26	1.49
1473	1150	106	9.74E-07	1.82E-07	0.21	1.16
	1150	167	1.11E-06	2.10E-07	0.23	1.16
	1150	217	2.10E-06	4.00E-07	-0.09	1.17
	1150	269	2.09E-06	4.02E-07	0.37	1.17
	1150	319	2.67E-06	5.19E-07	0.44	1.18
	1150	369	3.07E-06	6.02E-07	0.51	1.18
	1150	89	5.70E-07	2.16E-07	0.16	1.47
	1150	142	2.59E-07	9.86E-08	0.10	1.47
	1150	196	4.70E-07	1.80E-07	0.18	1.47
	1150	250	4.42E-07	1.70E-07	0.24	1.48
1592	1150	329	9.62E-07	3.72E-07	0.45	1.48
1472	1100	91	1.48E-06	2.42E-07	0.26	1.11
	1100	90	1.83E-06	3.01E-07	0.07	1.11
	1100	118	6.54E-07	1.08E-07	0.09	1.11
	1100	168	1.43E-06	2.40E-07	0.24	1.12
	1100	220	2.30E-06	3.89E-07	0.35	1.12
	1100	274	2.37E-06	4.05E-07	0.51	1.13
	1100	327	2.72E-06	4.71E-07	0.40	1.13
	1100	381	1.96E-06	3.43E-07	0.45	1.14
	1100	433	2.32E-06	4.11E-07	0.36	1.14
	1100	487	1.82E-06	3.26E-07	0.34	1.14
	1100	539	1.79E-06	3.25E-07	0.39	1.15
	1100	588	2.26E-06	4.14E-07	0.43	1.15

Figure 20 (n fixed at 1). The small amount Ca added to the forsterite had two dramatic effects. The first and more obvious effect is the abnormal grain growth. The second effect is a more subtle increase in creep strength. After correcting strain rate for the abnormal grain growth, the Ca-doped samples were between 4 and 12 times stronger than the undoped forsterite. The addition of Pr did not have a strong effect on grain growth, producing similar log-normal grain size distributions with only slightly smaller grain sizes than the undoped forsterite. The Pr-doped samples were between 4 and 23 times stronger than undoped Fo, that is, they were of similar strength as the Ca-doped samples. The addition of Pr also affects the position of the boundary between diffusion and dislocation creep. At the highest temperature, the stress exponent is significantly greater than 1. For the undoped and Ca-doped forsterite at 1250°C, $n = 1.6$, indicating that diffusion creep is not accommodating all of the strain. The Pr-doped samples, however, exhibit this transition from just diffusion creep to the addition of a dislocation-driven mechanism at a lower temperature. The stress exponent for Pr-doped samples increases with temperature from the diffusion creep value of $n \approx 1$ at 1150°C to $n \approx 3$ at 1250°C, a value associated with a dislocation-accommodated creep process.

The addition of these impurities have both a mechanical and a chemical effect on forsterite. In diffusion creep of a ceramic, the rate of deformation is limited by the slowest ion (Andersson, 1989) which in bulk forsterite is Si. Based on an analysis of published diffusion data, Hirth and Kohlstedt (1995) argued that grain boundary diffusion of Si rate limits diffusion creep of San Carlos olivine. Silicon diffusivity along

grain boundaries in Fo is 10^9 times faster than Si diffusivity through the matrix at 1200°C, and grain boundary diffusivity of Si in the grain boundaries is within error for Mg diffusivity along grain boundaries (Farver and Yund, 2000). In ceramics, the rate limiting species for deformation is the slowest ion along its fastest path (Gordon, 1973). At temperatures less than 1200°C, grain boundary diffusion of Si is definitely the rate limiting species (Farver and Yund, 2000). Figure 1 of Hirth and Kohlstedt (2003) compares the diffusivities at 1300°C for Mg through the grain matrix, Mg through the grain boundaries, Si through the matrix, Si through the grain boundaries, and the diffusivity of olivine deforming by diffusion creep for a wide range of grain sizes. Although the diffusivities of Mg and Si through grain boundaries are closer together than Mg and Si through the grain matrix, the bulk diffusivity of olivine very closely matches that of Si through the grain boundaries at 1300°C. These results confirm that for the temperatures at which the undoped and doped olivines were deformed, Si diffusing along grain boundaries is rate limiting. Thus, in the diffusion creep regime to make the impurity doped rock stronger than the undoped rock, the presence of the impurity must retard diffusion of Si. As replacing Mg with Ca should have no effect on the concentrations of intrinsic point defects, the larger Ca ion in the very narrow grain boundaries must physically limit the ability of Si to move past it. Yoshida et al. (1998) found a similar result in Al_2O_3 , where the diffusion of Al^{3+} along the grain boundaries was restricted by the boundary segregation of small amounts La^{3+} , Y^{3+} or Lu^{3+} , which are significantly larger than Al^{3+} .

The addition of Pr^{3+} induces a change in the point defect population to compensate for its charge difference. This change in the concentration of point defects due to Pr^{3+} should have an effect similar to that of Fe^{3+} , which makes Fe-bearing olivine weaker than forsterite (Zhao et al., 1999). A weakening effect is not seen, however. The concentration of Ca is at least an order of magnitude larger than the concentration of Pr in our impurity-doped samples. For alumina, increasing concentration of the dopant Zr^{4+} by an order of magnitude resulted in an order of magnitude increase in the strength (Wakai et al., 1997). Since the Ca-doped and Pr-doped samples have similar strengths, the chemical effect of the addition of Pr must offset the effect of a smaller concentration of the impurity on the grain boundaries. If Si diffuses by an interstitial mechanism (Hirsch and Shankland, 1993; Houlier et al., 1990), the addition of Pr would decrease the self-diffusivity of Si by decreasing the concentration of Si interstitials via the reaction



using Kröger-Vink notation (Kröger and Vink, 1956).

The activation energies for creep of the three types of samples are all ~250 kJ/mol, as detailed in Figure 21. The similarity of the values for the activation energies suggests that all three types of samples are rate limited by the same diffusing species; the presence of Pr^{3+} merely decreases the concentration of the point defects that facilitate diffusion thus slowing the rate of diffusion. This chemical effect on Si diffusion is limited to grain boundaries and near grain boundary regions, as Pr is not easily

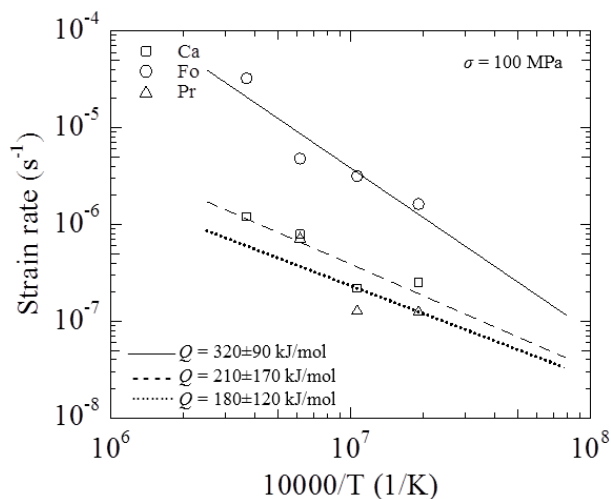


Figure 21. Arrhenius plot for calculation of activation energy. Stress exponent was fixed at $n = 1$.

incorporated into the forsterite lattice (Nielsen et al., 1992; Beattie, 1994; Hiraga, et al. 2007).

As the rate of diffusion creep of the Pr-doped samples is slower than the undoped samples, the transition to dislocation creep happens at lower temperatures and smaller grain sizes, as indicated by the increase in stress exponent with increasing temperature observed for the Pr-doped samples. As the effect of Pr^{3+} is limited to the grain boundary area, dislocation creep should be largely unaffected by its presence. The log-log plot of strain rate versus stress in Figure 22 illustrates the effect of decreasing the rate of diffusion creep on this transition. Based on the flow laws from Hirth and Kohlstedt (1995) for diffusion creep and dislocation creep, the transition between the mechanisms occurs at ~ 300 MPa. If the diffusion creep flow law is strengthened by a factor of 23 (the highest difference between the Pr-doped and undoped samples), the transition occurs at a stress of ~ 100 MPa.

The strengthening effect of these cation impurities in the grain boundary diffusion creep regime indicates that compositional differences alone do not account for the difference between natural and undoped synthetic samples. In the comparison in Figure 23 of the strengths of natural and synthetic, as well as iron-bearing and iron-free olivine samples, at a given strain rate, the synthetic samples are at least an order of magnitude stronger than the natural sample. Larger impurities cannot be used to bring the strength of natural olivines and synthetic forsterite into agreement. Smaller impurities, such as H^+ (Hirth & Kohlstedt 1996; Mei & Kohlstedt, 2000) or Fe^{3+} (Zhao et al. 1999), have been shown to weaken olivine. Additional smaller impurities could be used to help explain the strength difference. Unlike the alumina or zirconia, cations smaller than Mg^{2+} also have the opportunity to reside on the Si^{4+} site. With the

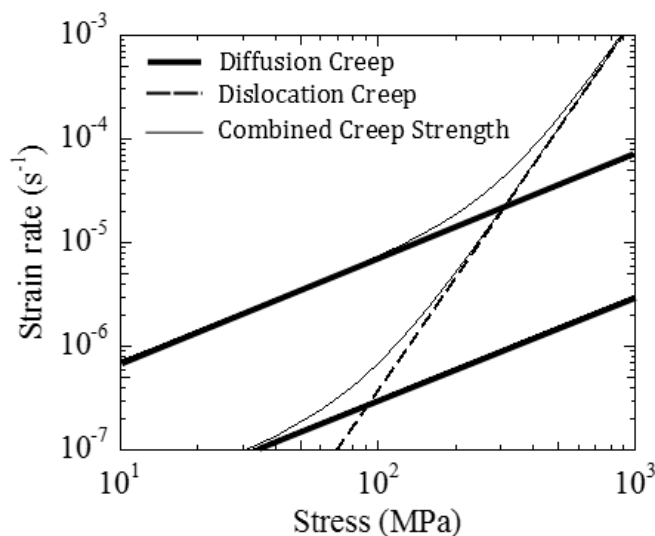
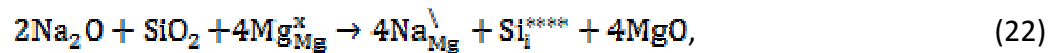


Figure 22. Schematic diagram of the transition from diffusion creep (thick lines) to dislocation creep (dash line). The upper black line represents diffusion creep of undoped Fo, and the lower black line represents the diffusion creep of Pr-doped Fo. If the presence of Pr does not affect dislocation creep, the Pr doped samples will transition into dislocation creep at a lower stress than the undoped Fo.

exception of H^+ , most cations are larger than Si^{4+} , and so a similar effect could occur, placing a larger cation on a smaller site. Titanium is a good example of this, as Ti^{4+} is smaller than Mg^{2+} and larger than Si^{4+} , but is known to reside on both Mg and Si sites (Hermann et al., 2005). An alternate option is to have an undercharged cation, such as Na^+ or H^+ , sitting on the Mg^{2+} site,



which could have the opposite effect of Pr and increase the population of Si interstitials.

Compositional changes alone in grain boundaries do not seem to cause a big enough shift to bring natural synthetic and purely synthetic sample mechanical data into agreement. A structural change, such as a small amount of melt, remains a likely candidate to explain the difference in strengths.

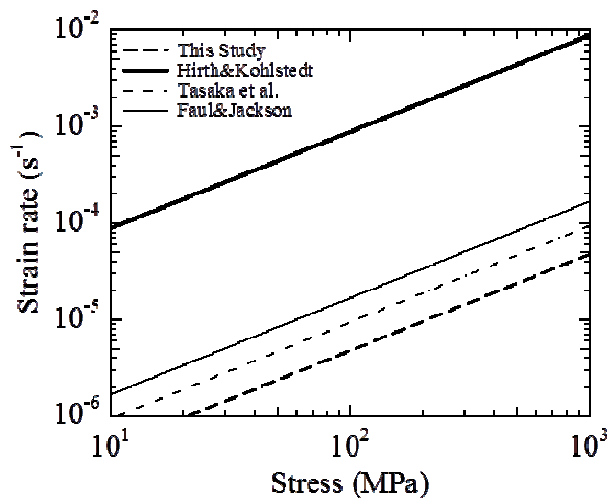


Figure 23. Comparison of diffusion creep strength for natural San Carlos (Hirth and Kohlstedt, 1995), synthetic, iron-bearing olivine (Faul and Jackson, 2007), synthetic forsterite (Tasaka et al., 2013), and undoped Fo (this study).

Chapter 4: The Effect of Small Amounts of Melt on the Deformation Strength of Forsterite

Summary

The majority of the melt-bearing mantle has a melt fraction, ϕ , of less than 0.01, while the majority of deformation experiments on partially molten rocks have been carried out on samples with $\phi > 1\%$. As the presence of melt has a strong effect on numerous properties, such as creep strength, it is important to understand the effect of very small amounts of melt on rheological properties. A theory by Takei and Holtzman (2009) predicts a large decrease in olivine viscosity at the onset of melting, which is not encompassed by existing flow laws for partially molten olivine. To test this theory, two types of partially molten samples were created. The first type of samples were created by adding a melt phase rich in Ca and Al to a forsterite rock that had been synthesized to be in chemical equilibrium with it. Samples with melt fractions of $\phi = 0, 0.0003, 0.001, 0.003, 0.01, \text{ and } 0.07$ were deformed in a gas medium apparatus at a confining pressure of 300 MPa and a temperature of 1300°C. For samples with $\phi < 0.01$, the grain size remained mostly small, and the melt was not observed with scanning electron microscopy. Occasional melt pockets were identified in samples with $\phi = 0.01$, and melt pockets were prevalent in samples with $\phi = 0.07$. These higher melt fraction samples also had larger grain sizes, at 5 and 7 μm , respectively, compared to $\sim 1 \mu\text{m}$ in the smaller melt fraction samples. The second type of samples used the impurity praseodymium in forsterite to create a melt phase. The addition of 1 mol% Pr to

forsterite creates ~1 vol% melt, but also induces extreme grain growth. Decreasing the amount of Pr decreases the amount of melt, but even small amounts of melt enhanced grain growth. At a confining pressure of 300 MPa and 1100° or 1200°C, the melt bearing-samples were weaker than the melt-free, Pr-doped forsterite samples. The change in deformation mechanism from diffusion creep in the melt-free samples to a dislocation creep mechanism in the melt-bearing samples invalidates a direct comparison of viscosities. The strength of the Ca/Al melt-bearing samples decreased with increasing melt fraction, with the exception of the samples with $\phi = 0.0003$, which were weaker than all but the samples with $\phi = 0.01$ and $\phi = 0.07$. This weakening effect was larger than existing flow laws predict. These data confirm that significant weakening occurs at the onset of melting; however, the decrease in viscosity with the initial melting is larger than predicted by Takei and Holtzman (2009). An additional result of these experiments is to confirm an explanation for why high purity synthetic olivines are more than an order of magnitude stronger than natural samples. Although composition is an important variable, the addition of a melt fraction as small as 0.001, which would not be observable in SEM images of fine grain samples, brings the undoped Fo data of this study into agreement with published strengths of natural San Carlos olivine.

4.1 Introduction

The presence of small amounts of melt in the mantle profoundly influences physical properties including seismic velocities, electrical conductivity, and creep strength. A variety of studies have determined that the majority of the partially molten mantle does contain more than $\sim 1\%$ melt. Nonetheless, the vast majority of experiments on partially molten materials have used samples with melt fractions between 0.05 and 0.2. The recent theory of Takei and Holtzman (2009) predicts a significant decrease in rock viscosity at very small melt fractions, as shown in Figure 1, which has not been fully explored in previous studies. It is important to understand this weakening behavior not only to model properly the large-scale behavior of the mantle, but also to explain recent experimental results. Figure 2 details the difference in strength between natural olivine and the purely synthetic forsterite of this study, deformed under similar conditions. Although changing the concentration of minor or trace elements can affect creep strength, a small amount of melt not visible to scanning electron microscopy could also be used to explain this strength difference. A fuller understanding of the effect of small amounts of melt on the mechanical properties of rocks is clearly important for understanding many chemical and physical processes in the Earth.

4.2 Theoretical Background

Although the melt fraction in the upper mantle is small, $\phi < 0.01$ (McKenzie, 1989), the presence of this melt strongly affects mechanical, electrical, and chemical

properties of the partially molten rock. High seismic attenuation (Anderson and Sami's, 1970), high electrical conductivity (ten Grotenhuis et al., 2005; Yoshino et al. 2010), and low seismic velocities (Nakajima et al., 2005; Ni et al., 2011) under ocean basins are often attributed to the presence of melt (Gribb and Cooper, 2000; Kawakastu et al., 2009). Melt affects the mechanical strength of olivine-rich rocks directly by enhancing diffusion through grain boundaries and lowering grain boundary contiguity (Kohlstedt and Zimmerman, 1996; Scott and Kohlstedt, 2006; Faul and Jackson, 2007; Hustoft et al. 2007) and indirectly by affecting the evolution of grain size (Cooper and Kohlstedt, 1984; Braun et al., 2000; Faul and Scott, 2006) as well as the water content (Kohlstedt and Zimmerman, 1996; Braun et al., 2000). The total amount of melt and history of melting affects the bulk chemistry of the mantle (Daines and Kohlstedt, 1994; Aharonov et al., 1995; Hier-Majumder et al., 2006) as well as the presence of trace elements (Drury and

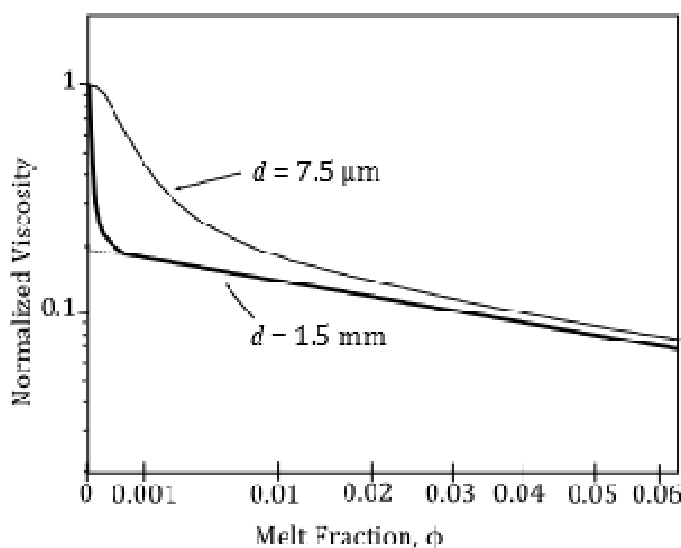


Figure 1: Predicted dependence of viscosity of melt-bearing samples versus melt fraction, as modified from Takei and Holtzman (2009). Viscosity has been normalized by the viscosity of a melt-free sample. The critical melt fraction at which the viscosity decreases rapidly with increasing melt fraction depends on grain size; the critical melt fraction decreases as grain size decreases.

FitzGerald, 1996; Kohlstedt and Zimmerman, 1996; Kelemen et al., 1997; McKenzie, 2000). Given the vast influence of melt, it is important to determine the quantity and distribution of melt in the upper mantle and to quantify how the melt distribution affects mechanical properties.

The amount of melt in the upper mantle varies with both vertical and horizontal location. Under ridges, large region of produced over a large region is focused into a small area of melt extraction (Langmuir et al. 1993; Faul, 2001). This means regions of the mantle exist with melt fractions below the level necessary for segregation, roughly 200 km wide at the onset of melting (Braun et al., 2000). Melting is initiated at a depth of 70-120 km beneath a mid-ocean ridge (Shen and Forsyth, 1995). Deeper melts are possible, though, as the seismic low velocity zone at 350 km can also be explained by 1% melt (Hier-Majumder and Courtier, 2011). The composition of the produced melts

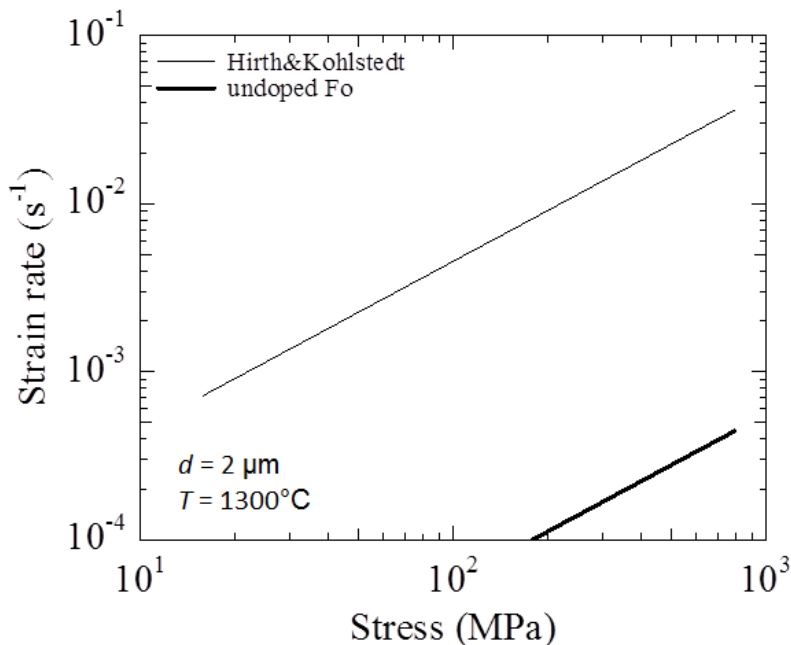


Figure 2: Strain rate versus differential stress for polycrystalline samples of San Carlos olivine (Hirth and Kohlstedt, 1995), compared to creep data from high-purity, synthetic forsterite (this study).

indicates 'near fractional melting', where a small amount of melt is produced and then extracted (Langmuir et al., 1977; Kelemen et al. 2001). This limits the amount of melt present to $0.1\% < \phi < 1\%$ (Kelemen et al., 1997; McKenzie, 2000). Naturally occurring dunites have been calculated to retain $<0.1-0.2\%$ melt after crystallization, indicating the necessary interconnected porosity to extract melt is $>0.2\%$ (Sundberg et al. 2010). Electrical conductivity studies indicate the partially molten upper mantle has 1-4% melt (ten Grotenhuis et al., 2005; Yoshino et al., 2010). Seismic studies agree that the seismic low velocity zone can be explained by $\sim 2\%$ melt (Ni et al., 2011). To extract this melt, these small melt fractions are focused into higher melt fraction areas.

The effect of melt on physical properties of the mantle depends on more than the mere existence of the melt; the distribution of the melt also plays an important role. Seismic velocity reductions (Waff and Faul, 1992; Yoshino et al., 2005) and seismic attenuation data (Gribb and Cooper, 2000) cannot be adequately explained by a texturally equilibrated melt phase. At the grain scale, melt distributions are determined by the dihedral angle, which for basalt and olivine is $\theta = 20^\circ-50^\circ$ (Waff and Bulau, 1979; Mei et al. 2002; Yoshino et al., 2007). This angle means grain boundaries are not wetted with melt (Cooper and Kohlstedt, 1984), which would correspond to $\theta = 0^\circ$. Because $\theta < 60^\circ$, small amounts of melt sit entirely in olivine triple and four-grain junctions (Waff and Faul, 1992; Yoshino et al., 2007), which become interconnected at melt fractions of $\phi > 0.005$ (Bargen and Waff, 1986; Holtzman, 2015). As the amount of melt increases, an increasing fraction of the grain boundaries become wet. Approximately 10% of grain

boundaries are wetted at $\phi = 0.02$, and ~40% are wetted at $\phi = 0.012$ (Mei et al. 2002; Zimmerman and Kohlstedt, 2004; Yoshino et al., 2005; Garapic et al., 2013). Grain boundaries do not wet uniformly. The anisotropy in surface energies for olivine causes melt to wet some grain boundaries before others (Cmiral et al., 1997). This result is confirmed by conductivity data that indicates that even at melt fractions ~0.1, many grain boundaries are still completely melt free (ten Grotenhuis et al., 2005).

Larger scale melt distributions are important for extracting melt from the mantle. As erupted melts are in disequilibria with the residue (Spiegelman and Kenyon, 1992; Aharonov et al., 1995; Kelemen et al., 1997), some form of channelization is necessary. Focusing this melt can be driven by reaction (Daines and Kohlstedt, 1994) or stress (Holtzman et al., 2003; King et al. 2009). Seismic studies can detect the increased melt fraction, but are not necessarily capable of uniquely determining the melt distribution. Low seismic velocities below the Mid-Atlantic Ridge have been attributed to high temperatures and up to 5% melt (Dunn et al. 2005). Under Japan, a study combining P and S wave structures by Nakajima et al. (2005) concluded that the melt is in grain boundary tubules at 90 km, thin planar distributions at 65 km, and in larger cracks or dikes at 40 km. This evidence all points to a wide region where melt flows through interconnected tubes in a porous manner, and then gradually evolves into a channel flow mechanism (Spiegelman and Kenyon, 1992; Kelemen et al., 1997). Capillary forces ensure that a small amount (<0.2%) of melt is always retained (Hier-Majumder et al. 2006; Holtzman, 2015).

The presence of melt decreases viscosity of the host rock. At very low stresses and displacements, typical of deformation due to seismic waves, melt enhances elastically accommodated grain boundary sliding (Faul et al., 2004), which can be detected through increased seismic attenuation. At the higher stresses, the effect of melt on plastic deformation mechanisms must be considered. In diffusion creep, melt acts as a rapid diffusion pathway (Cooper and Kohlstedt, 1986; Kohlstedt and Zimmerman, 1996; Takei and Holtzman, 2009). Experiments on olivine with a few percent melt shows an increase in strain rate by a factor of 2-5 relative to nominally melt free samples, but in these partial melt experiments there was no change in other flow law parameters such as stress exponent, grain size exponent, and activation energy (Cooper and Kohlstedt, 1984; 1986). Based on these observations, these authors concluded that strain rate is still limited by grain boundary diffusion along melt-free grain boundaries. In the dislocation creep regime, melt likely enhances the necessary grain boundary accommodation mechanism as well as increasing the shear stress by decreasing the load bearing area of the grain boundary. These combined effects can enhance dislocation creep strain rates by a factor of 1.5-4 at $\phi = 0.03$ (Kohlstedt and Zimmerman, 1996). Although these melts create interconnected networks, even melt that sits in isolated pockets lower the viscosity of the rock (Hustoft et al., 2007). This weakening effect could be key in decoupling the convecting mantle from the overlying plates (Anderson and Sammis, 1970; Naif et al. 2013).

Melt is usually accounted for in flow laws with an empirical exponential expression (Keleman et al., 1997),

$$\dot{\epsilon}_{melt} = \dot{\epsilon}_{no\ melt} * e^{\alpha\phi} = A\sigma^n d^{-p} e^{\alpha\phi}. \quad (1)$$

This empirical factor varies with deformation mechanism. For diffusion creep, $\alpha = 21-26$ (Mei et al. 2002; Zimmerman and Kohlstedt, 2004; Scott and Kohlstedt, 2006), while in dislocation creep $\alpha = 32-45$ (Keleman et al., 1997; Scott and Kohlstedt, 2006). This empirical relationship holds true for melt fractions between two critical values. In diffusion creep, there is a theoretical lower limit, determined by when the melt is no longer interconnected through grain boundaries. This value is dependent on the grain size, but in general is $\phi_{crit, low} = 1-2\%$ (Takei and Holtzman, 2009). Once the melt fraction increases above this critical melt fraction, strain rate would quickly increase. Experiments conducted on samples with a wide range of melt fractions ($\sim 0\% < \phi < 30\%$), showed an increase in strain rate by several orders of magnitude from $\phi = 25\%$ to 30% (Scott and Kohlstedt, 2009). This equation is therefore considered valid for melt fractions $2\% < \phi < 25\%$.

Melt also has several indirect effects on viscosity. The presence of water in olivine is known to make it significantly weaker (Mackwell et al., 1985; Karato et al., 1986; Karato, 1998; Mei et al. 2002). Water can also affect dihedral angle (Yoshino et al. 2007). As H^+ is incompatible in olivine, as soon as melting occurs the water segregates into the melt phase (Karato, 1986; Hirth and Kohlstedt, 2003), making olivine stronger. If the presence of this initial amount of melt does not create a greater weakening effect

than the water content, the mantle might grow stronger once it melts. Water also affects the depth of melting, as it lowers the melting temperature of olivine. In the deep mantle, pressure is too great and temperature too low for melting to occur. However, the change in the solubility of water in mantle minerals at the top of the transition zone can induce melting, creating a low seismic viscosity zone (Revenaugh and Sipkin, 1994; Yoshino et al., 2007).

A second indirect effect of melt on viscosity is due to grain size. Steady state grain size is inversely dependent on melt fraction (Cooper and Kohlstedt, 1984), and the presence of melt limits grain growth kinetics (Hirth and Kohlstedt, 1995; Faul and Scott, 2006; Scott and Kohlstedt, 2006). The average grain size of the mantle is much greater than in experiments, which makes diffusion creep less likely than dislocation creep to occur in the mantle. If the presence of melt decreases the grain size of mantle rocks, deformation in the mantle is more likely to be grain size sensitive.

An experimental constraint on the effect of a very small amount of melt on creep strength is important for understanding the deformation of a large portion of the upper mantle. Experiments on natural olivine + basalt systems are usually conducted on samples fabricated by mechanically mixing basalt glass powders with ground olivine, which is then synthesized into a dense solid. These experiments showed little strain rate enhancement due to melt for $\phi < 5\%$ (Cooper and Kohlstedt, 1986; Hirth and Kohlstedt, 1995; Faul and Jackson, 2007), unlike the prediction of the Takei and Holtzman (2009) theory. Drury and FitzGerald (1996) found a thin glass film on all the

observed grain boundaries of an olivine + pyroxene synthesized rock that had no melt added to it. This glass film was 1-500 nm thick, and only visible with transmission electron microscopy (TEM). If the natural olivine powders contained melt, then previous experiments on nominally melt-free olivine never truly provided a baseline for testing the effect of small amounts of melt. Faul and Jackson (2007) performed TEM analysis of olivine samples created from natural and sol-gel created powders. The sol-gel samples had no sign of melt; all the triple junctions were clean. In the natural samples, not all of the grain boundaries had melt, but melt was clearly present in the rock. In order to be sure of having melt-free samples, one approach is to create olivine powders from high purity chemicals.

4.3 Sample Preparation

To investigate the effect of small amounts of melt on the creep strength of olivine, high-purity, entirely synthetic forsterite was used. There are two ways to create samples with very small amounts of melt. The first is the traditional method of adding a glass phase to the sample, which will be melt at the pressure and temperature conditions of deformation. Faul and Jackson (2007) used sol-gel created olivine of the composition $(\text{Mg}_{0.9}\text{Fe}_{0.1})_2\text{SiO}_4$ with a natural mid-ocean ridge basalt added. However, the addition of this glass also alters the point defect concentration of the olivine by adding a number of impurities; independent of the glass (melt) phase, these impurities will influence viscosity. To isolate the effect of melt alone, a melt in chemical equilibrium with the forsterite is necessary. Therefore, the second method involves

gradually altering the composition of the forsterite by adding an incompatible impurity to induce melting. Drastic changes in the strength of the sample would then be due to the addition of a melt phase and not to a change in sample composition. We decided to take advantage of the fact that the addition of praseodymium to forsterite above the grain boundary solubility limit creates a melt phase. By gradually increasing the amount of this impurity, the melt fraction can be controlled, and the effect of changing composition is minimized.

Samples with a melt phase added were created in a similar way. The forsterite and glass powders were created from high purity nano-powders of $\text{Mg}(\text{OH})_2$, SiO_2 , CaCO_3 , and Al_2O_3 , which were tumbled in plastic bottles with plastic coated iron balls and ethanol for at least 24 h. This slurry was decanted into glass beakers and dried on a hot plate at 60°C , then calcined for 3 h at 1000°C . The glass phase had a pseudo-anorthitic composition: 48 wt% SiO_2 , 12 wt% MgO , 15 wt% CaO , and 25 wt% Al_2O_3 . Pure forsterite is not in equilibrium with this melt. To determine the forsterite composition in equilibrium with this glass phase, pure forsterite was sintered with this glass added. Large, discontinuous grain growth occurred. These large forsterite grains were analyzed to determine the amounts of Al and Ca incorporated. Synthesis of nano-forsterite of the composition 43.4 wt% SiO_2 , 56.3 wt% MgO , 0.2 wt% CaO , and 0.1 wt% Al_2O_3 was created. Figure 3 details the relative compositions of forsterite and the anorthitic glass. Figure 3a is centered on a melt pocket, which is strongly enriched in Ca, Al, and weakly enriched in Si compared to forsterite. Pyroxene grains appear dark in Figure 3a, and are

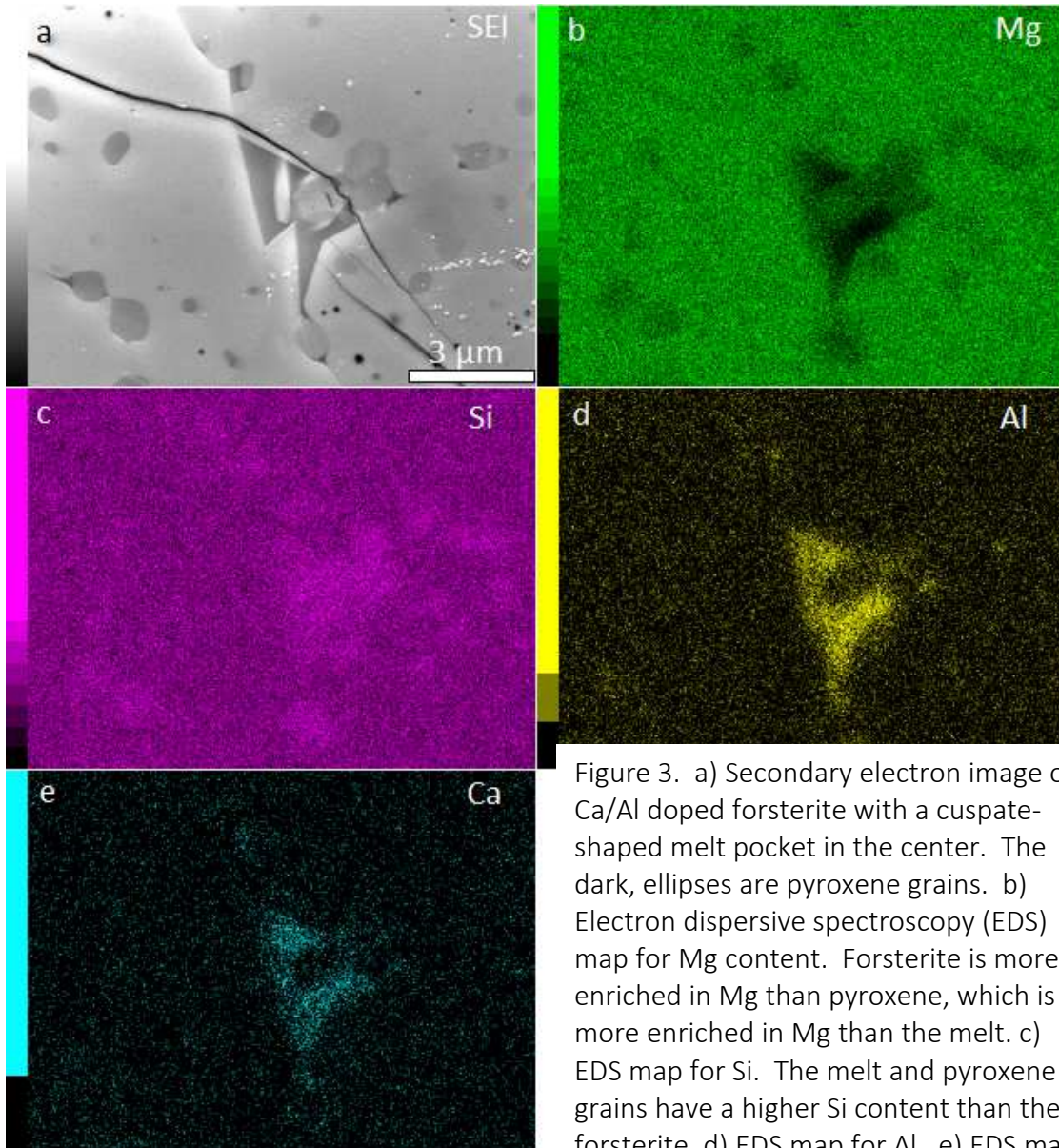


Figure 3. a) Secondary electron image of Ca/Al doped forsterite with a cusped-shaped melt pocket in the center. The dark, ellipses are pyroxene grains. b) Electron dispersive spectroscopy (EDS) map for Mg content. Forsterite is more enriched in Mg than pyroxene, which is more enriched in Mg than the melt. c) EDS map for Si. The melt and pyroxene grains have a higher Si content than the forsterite. d) EDS map for Al. e) EDS map for Ca. The melt phase is enriched in both Al and Ca.

clearly visible in the map for Mg and Si in Figure 3b and c, respectively. The Ca/Al-doped forsterite did not react with the anorthitic glass; the sample remained fine grained.

To mix the glass together with the forsterite, the powders were disaggregated in an agate mortar, then tumbled together in plastic bottle with plastic covered iron beads for ~24 h. A series of samples with different melt fractions were created: 0.0003, 0.001, 0.003, and 0.01. The amount of glass necessary to create a sample with a melt fraction of 0.0003 is below the resolution of the scale used to weigh the powders. A very large batch of forsterite powder was needed to make the mass of glass measurable. Therefore, all of the forsterite for this series was mixed with enough glass to create a 0.03 vol% mixture. After mixing, enough powder to fabricate several samples was removed. The remaining powder was mixed with additional glass powder to bring the glass volume up to 0.1%. This sequence continued up to 1 vol%. These mixtures were again calcined at 1000°C for 3 h.

Samples with Pr induced melting were created in the same fashion as the Pr-doped samples used in the dry diffusion creep study. Samples were created with 0.05, 0.1, and 1 mol% Pr. All samples were shaped into cylinders and vacuum sintered to full density.

One sample was made with the anorthitic glass at a higher melt fraction. This sample, which contained 7 vol% melt, was mixed solely in an agate mortar and was then uniaxially compressed to 100 MPa into a Ni can 2 cm tall and 1 cm in diameter. This Ni can was loaded into a deformation assembly and brought up to 1200°C and 300 MPa in the gas medium rig to densify it. At 1200°C, the glass did not become a melt.

4.4 Deformation Procedure

All deformation experiments were conducted in an Ar-gas pressure medium rig at a confining pressure of 300 MPa. The fully dense cylinders were placed in Ni cans, which were then inserted into an iron jacket, sandwiched between pistons of alumina and zirconia. Samples were deformed in triaxial compression at different constant loads. After deformation, the samples were removed from the assemblies, cut axially, and then polished to examine the microstructure.

Only two samples with Pr-induced melting were deformed. Very large grain sizes for these samples were observed in sintered samples. As we were attempting to determine the effect of melt on diffusion creep, these large grains precluded this possibility. These two deformation experiments were performed at 1100°C for the sample with 0.1 mol% Pr and 1200°C for the sample with 1 mol% Pr.

The high melt fraction sample prepared from the anorthitic glass was deformed at temperatures between 1200°C and 1300°C. The purpose of studying this sample was to confirm the melting point of this glass phase. The sample was brought to 1200°C and 300 MPa and then loaded at a differential stress of 20 MPa. The temperature was then increased at a rate of 0.01°C /s. Once the glass became a melt, the sample deformed more quickly than when the rock was entirely solid. As load was not varied during this experiment, the deformation mechanism could not be determined. An estimate of viscosity is made from this sample, but it is calculated from a single stress-strain rate pair. All other samples with anorthitic glass added were deformed at 1300°C.

4.5 Microstructure of Pr Induced Melt Samples

The addition of Pr above the solubility limit of the grain boundaries creates a melt phase that appears bright white in back scatter electron (BSE) images. This melt phase lies in olivine triple junctions in cusped pockets, similar to basalt pockets in olivine samples (e.g., Hirth and Kohlstedt, 1995). An image analysis of backscattered electron (BSE) micrographs allows an estimate of the melt fraction. Backscattered images are thresholded into binary images in order to distinguish the melt from the olivine. Using the image analysis software ImageJ, the amount of melt was quantified, and the area fraction of the melt was used as an estimate of the melt fraction. The melt phase was a mixture of Pr, Mg, Si, and O. Figure 4 is a BSE image of forsterite with 1 mol% Pr, which creates a melt fraction of $\phi \approx 0.01$. Figure 5 is a BSE image of forsterite with 0.1 mol% Pr and $\phi \approx 0.003$, and 0.05 mol% Pr creates $\phi \approx 0.002$. Rapid grain growth occurred in all

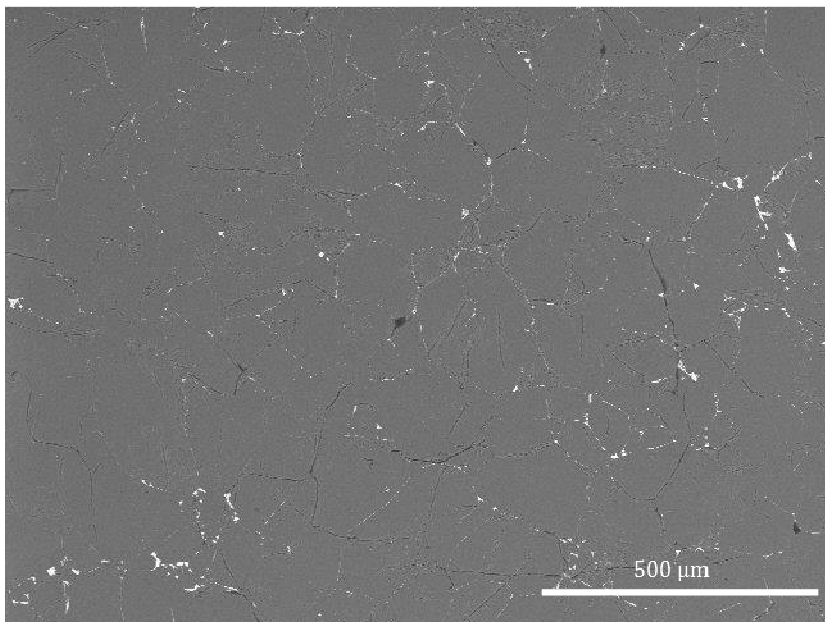


Figure 4. BSE image of a sample of forsterite doped with of 1 mol% Pr. The bright white phase is a Pr rich melt phase.

of these samples, such that even <1 vol% melt is clearly visible. One sample with 1 mol% Pr was vacuum sintered for a much shorter time. Instead of holding for 5 h at 1400°C under vacuum, this sample was heated to 1400°C and then immediately cooled to room temperature. This sample was highly dense, but the grain size was very bimodal. The majority of grains were still sub-micron in size, but the majority of the sample was made up of ~80 μm grains. In an attempt to limit grain

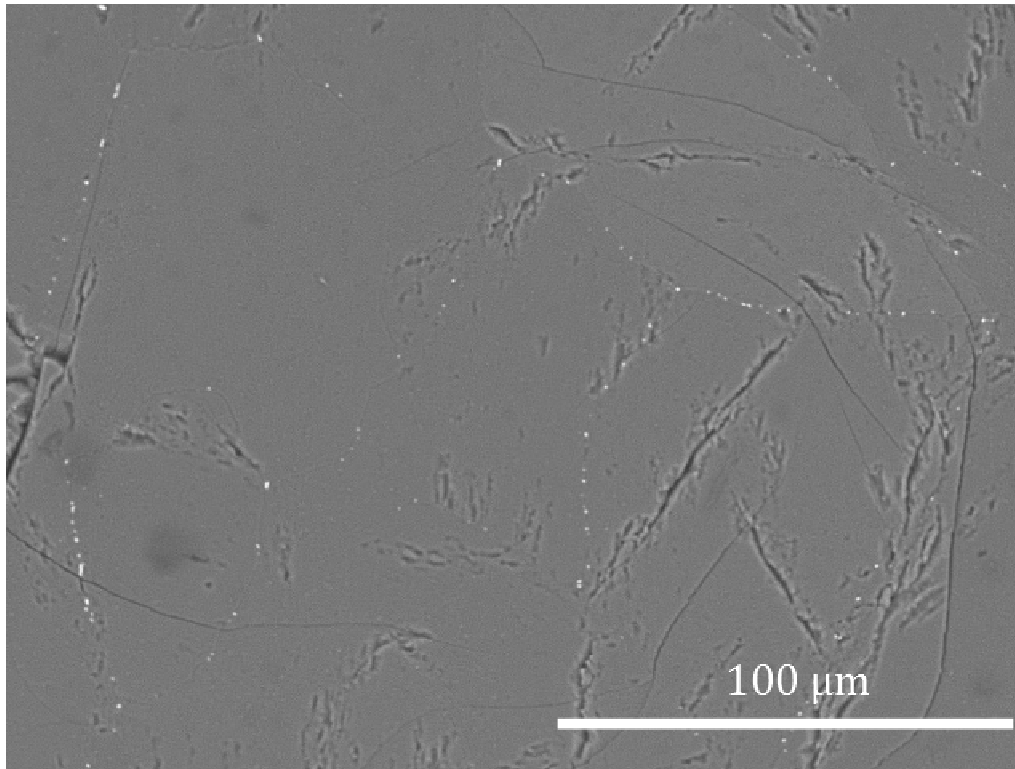


Figure 5. BSE image of image of a sample of forsterite doped with of 0.1 mol% Pr. The bright white phase is a Pr rich melt phase.

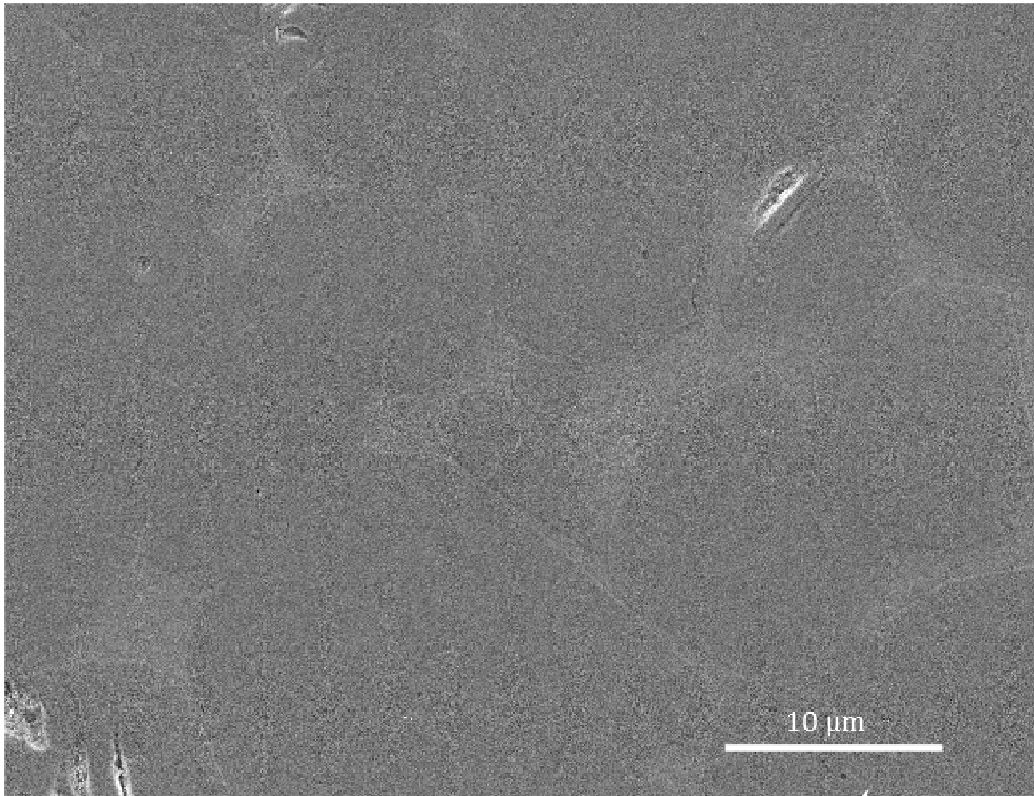


Figure 6. Secondary electron image (SEI) of a Ca/Al-doped forsterite sample with 7 vol% melt. The lighter gray cusped-shaped melt pockets occurred throughout this sample.

growth, a batch of forsterite was doped with enough extra silica to create 5 vol% enstatite as well as with 1 mol% Pr. However, the addition of enstatite did not significantly impede grain growth. This grain growth is in contrast to the previous results, which indicated melt would impede grain growth.

4.6 Microstructure of Anorthitic Melt Samples

The anorthitic glass also appeared as a bright phase in a BSE image due to the Ca in it. The sample created with 7 vol% melt had a large grain size, $7\mu\text{m}$, and large melt

pockets are visible in the secondary electron image (SEI) of Figure 6. Figure 7 is a BSE image of a Ca/Al-doped forsterite sample with 1 vol% melt with a visible melt pocket, an uncommon feature in these samples. Samples with 1 vol% melt had a larger grain size, $d = 5 \mu\text{m}$, than samples with less melt, $d < 2 \mu\text{m}$. Samples with a less than 1 vol% melt did not have any visible melt pockets in SEM images. Examples of the fine grain sizes of the low melt-fraction samples are presented in Figure 8a-c. The onset of abnormal grain growth is evident in the image of a sample with 0.03% melt in Figure 8d. This enhanced

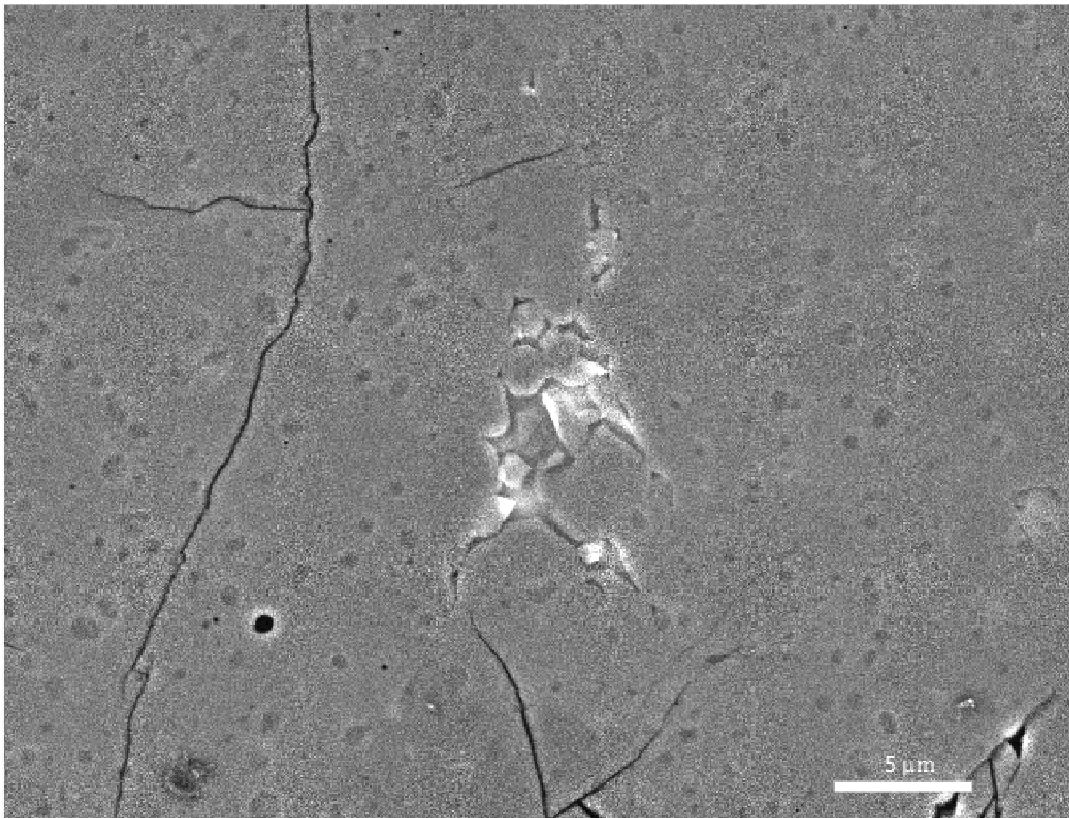


Figure 7. BSE image of sample containing 1 vol% anorthitic melt. The melt pocket in the center is lighter than the surrounding olivine. The dark dots are pyroxene grains.

grain growth with increasing melt fraction confirms the result of our experiments on Pr-doped samples. Melt does not appear to impede grain growth.

4.7 Mechanical Data of Pr Induced Melt Samples

The presence of melt in Pr-doped samples makes them weaker than melt-free samples. Although the extreme grain growth made deformation in a grain size sensitive region unlikely, two samples were deformed to confirm this weakening effect.

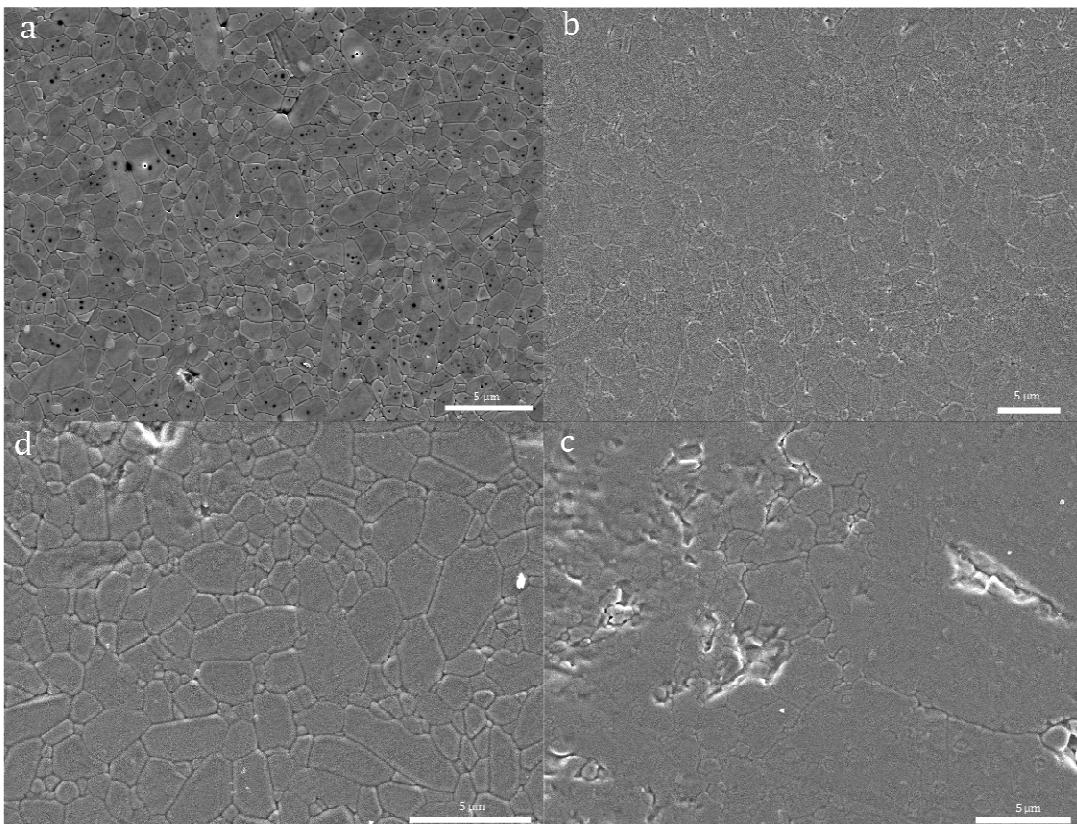


Figure 8. a) Secondary electron image (SEI) of a Ca/Al-doped Fo sample with no added melt. Black circles are pores that were trapped in grains during initial densification. b) SEI of Ca/Al-doped Fo sample with 0.03 vol% melt. c) SEI of Ca/Al-doped Fo samples with 0.1 vol% melt. d) SEI of Ca/Al-doped Fo sample with 0.3 vol% melt. A few abnormally large grains can be seen.

The mechanical data are summarized in Table 1. Both samples exhibited a stress exponent of $n \approx 2$. A sample with 0.1 mol% Pr deformed at 1100°C was stronger than undoped forsterite over the experimental range of stresses. Figure 9 displays this mechanical data as well as the flow laws determined for undoped samples of forsterite and samples of forsterite doped with 0.01 mol% Pr. Extrapolating the fit of this data predicts a transition to the melt-bearing sample being weaker than the undoped forsterite occurring at stresses just above those of the experiment. A sample containing 1 mol% Pr deformed at 1200°C was roughly the same strength as undoped forsterite, as revealed in Figure 10. Both samples were measurably weaker than the samples doped with 0.01 mol% Pr. The sample with 1 mol% Pr, corresponding to $\phi \approx 1\%$, was weaker by a factor of 6 to 9 than the melt-free, Pr-doped sample. The sample with 0.1 mol% Pr, corresponding to $\phi \approx 0.3\%$, was weaker by a factor of 1.3-3.8 than the melt-free, Pr-doped sample. This weakening effect is additional confirmation that the bright white phase present in BSE images of Pr-doped samples is indeed a melt. Although the stress exponent for these experiments is $n \approx 2$, which would indicate a grain size exponent of $p = 2$ according to the dislocation accommodated grain boundary sliding model of Langdon (2006), no grain size correction was made. If it had been made, these samples would be a factor of ~ 2000 weaker than the melt free sample, as the average grain size for the 0.1 mol% Pr sample was 89 μm and for the 1 mol% Pr sample was 84 μm and the undoped and Pr-doped melt free flow laws are plotted for $d = 2 \mu\text{m}$.

Table 1. Compilation of mechanical data for melt bearing Pr-doped Fo samples

Pr content (mol%)	Melt Fraction (%)	Stress (MPa)	Strain Rate (1/s)	Strain %	Temperature (°C)
1	1	116	6.39E-06	1.35	1200
1	1	146	6.75E-06	0.99	1200
1	1	198	8.36E-06	1.91	1200
1	1	260	1.27E-05	1.74	1200
1	1	310	2.11E-05	2.26	1200
1	1	330	5.37E-05	1.23	1200
0.1	0.3	96	3.52E-07	0.02	1100
0.1	0.3	120	1.38E-06	0.07	1100
0.1	0.3	177	1.78E-07	0.14	1100
0.1	0.3	297	3.33E-07	0.88	1100
0.1	0.3	370	2.51E-06	0.60	1100
0.1	0.3	520	5.55E-06	1.23	1100

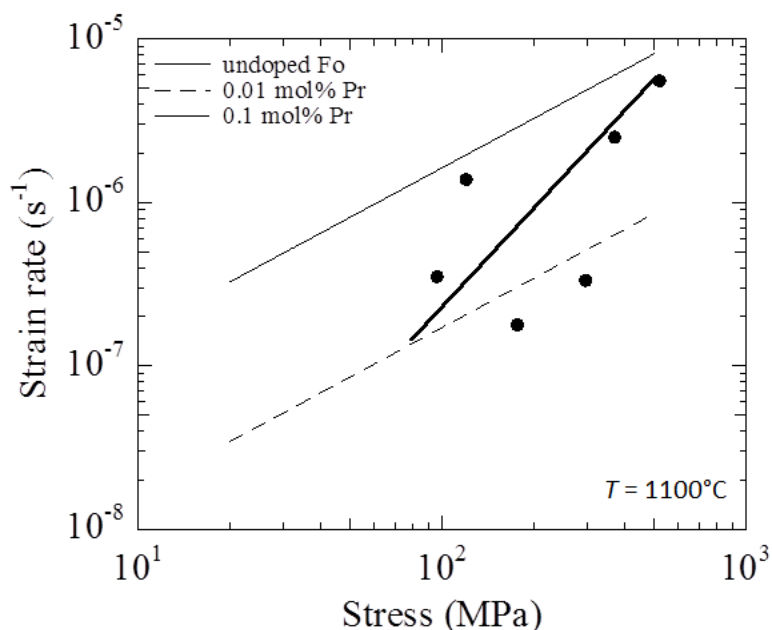


Figure 9. Mechanical data for a forsterite sample doped with 0.1 mol% Pr. The thin solid line represents the diffusion creep flow law established for undoped forsterite in this study, and the dashed line represents the diffusion creep flow law for 0.01 mol% Pr-doped Fo at $d = 2 \mu m$ and $T = 1100^{\circ}C$. The melt bearing Pr-doped sample is weaker than the melt-free sample, but still stronger than undoped Fo.

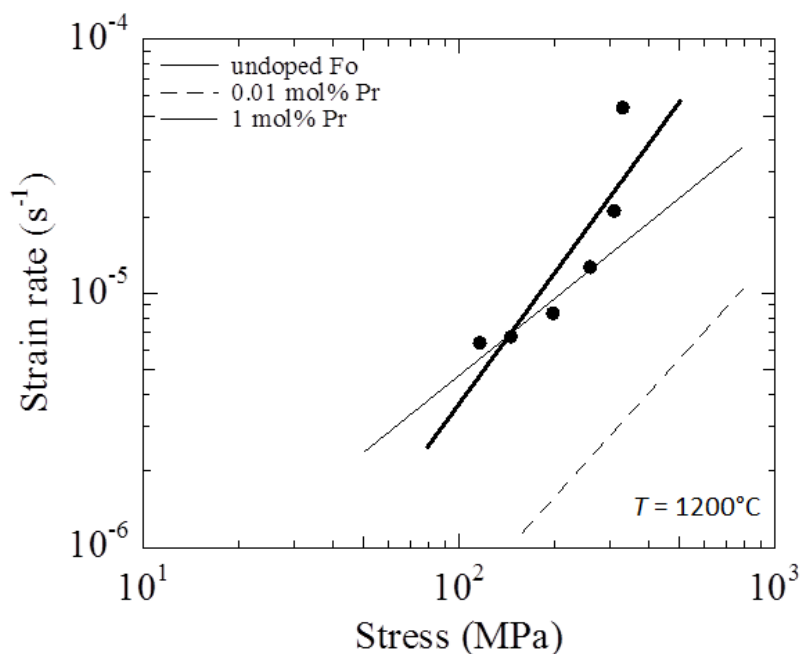


Figure 10. Mechanical data for a forsterite sample doped with 1 mol% Pr. The thin solid line represents the diffusion creep flow law established for undoped Fo, and the dashed line represents the diffusion creep flow law for 0.01 mol% Pr-doped Fo at $d = 2 \mu m$ and $T = 1200^{\circ}C$. The melt bearing Pr-doped sample is weaker than the melt-free sample, and roughly the same strength as the undoped Fo.

4.8 Mechanical Data of Anorthitic Melt Samples

The anorthitic melt also had a weakening effect. The mechanical data of the Ca/Al- doped forsterite with and without anorthitic melt plotted in Figure 11 on a log strain rate vs. log stress scale have a slight curvature that suggests these data lie near the transition between two mechanisms. Data for each melt fraction were fit with a combined flow law with diffusion creep and a power law dependence on stress,

$$\dot{\epsilon} = A_1\sigma + A_n\sigma^n. \quad (2)$$

This fitting resulted in $n \approx 3$, so this combined fit was modified to a portion with $n = 1$

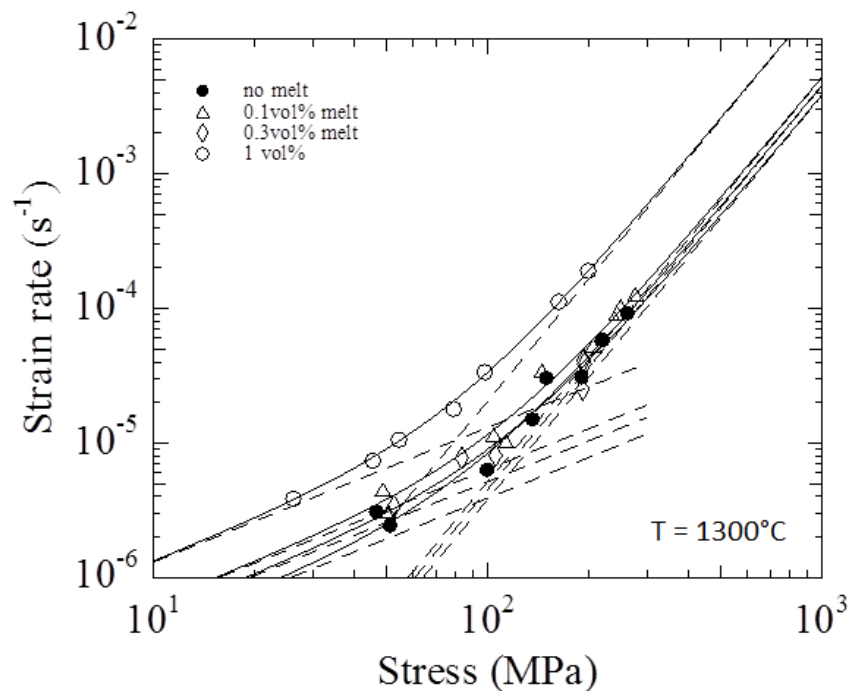


Figure 11. A combined flow law with $n = 1$ and $n = 3$ plotted through the mechanical data for several different melt fraction bearing samples. The data from samples with 0.03 vol% melt could not be fit with this combined flow law and are thus omitted from this graph.

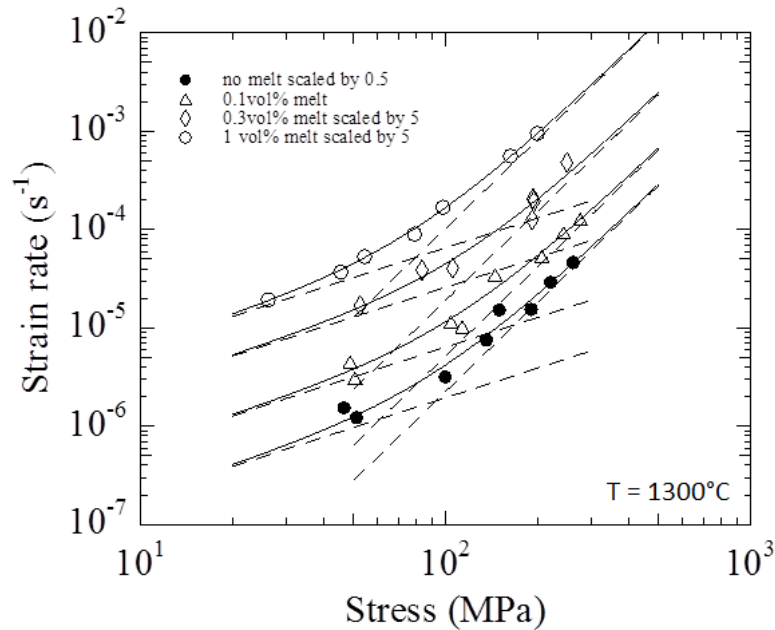


Figure 12. A combined flow law with $n = 1$ and $n = 3$ plotted through the mechanical data for several different melt fraction bearing samples. As the data points from different melt fraction samples plot close together, the data has been scaled to show the combined fit more clearly. See text for additional details.

and a dislocation driven mechanism with $n = 3$ was fit in Figure 11. Because the data overlie each other quite a bit, an expanded view of this fit is in Figure 12. The data from the melt-free samples were scaled by a factor of 0.5, while the data from the samples with 0.3 vol% melt and 1 vol% melt were scaled by a factor of 5. The data from the samples with 0.03 vol% melt, due to the large amount of scatter, could not be fit with this combined flow law, and so it are excluded from these figures. However, all of the data fit reasonably well with a single flow law with $n = 2$. As the grain size variation is not large enough to fit for a grain size exponent, we assume $p = 2$ for Racherger sliding (Langdon, 2006). The mechanical data are summarized in Table 2, and the fit

Table 2. Compilation of mechanical data for anorthitic melt bearing Fo samples.

Melt Fraction (%)	Stress (MPa)	Strain Rate (1/s)	Normalized Strain Rate (1/s)	Strain (%)	Grain Size (μm)
0	46	3.1E-06	1.0E-06	7.2	0.6
0	51	2.4E-06	8.2E-07	1.4	0.6
0	100	6.3E-06	2.1E-06	0.7	0.6
0	136	1.5E-05	5.0E-06	3.6	0.6
0	150	3.0E-05	1.0E-05	3.8	0.6
0	191	3.1E-05	1.0E-05	3.6	0.6
0	221	5.8E-05	2.0E-05	7.9	0.6
0	262	9.2E-05	3.1E-05	3.7	0.6
0.03	11	8.3E-06	3.0E-06	0.7	0.6
0.03	14	3.5E-05	1.3E-05	3.8	0.6
0.03	17	1.8E-04	6.4E-05	12.9	0.6
0.03	30	2.5E-05	9.1E-06	2.2	0.6
0.03	41	1.3E-05	4.8E-06	0.3	0.6
0.03	52	7.2E-05	2.6E-05	4.1	0.6
0.03	56	4.4E-05	1.6E-05	3.7	0.6
0.03	63	1.6E-04	5.9E-05	12.1	0.6
0.03	79	6.0E-05	2.2E-05	3.1	0.6
0.03	84	1.3E-04	4.6E-05	7.8	0.6
0.03	134	1.4E-04	5.1E-05	6.7	0.6
0.03	192	1.8E-04	6.4E-05	8.3	0.6
0.1	49	4.5E-06	5.4E-06	1.2	1.1
0.1	50	3.1E-06	3.7E-06	0.6	1.1
0.1	104	1.1E-05	1.4E-05	1.2	1.1
0.1	113	1.0E-05	1.2E-05	0.5	1.1
0.1	145	3.4E-05	4.2E-05	3.1	1.1
0.1	207	5.3E-05	6.4E-05	3.5	1.1
0.1	244	9.2E-05	1.1E-04	6.8	1.1
0.1	276	1.3E-04	1.5E-04	5.9	1.1
0.3	52	3.4E-06	5.1E-06	1.1	1.2
0.3	84	7.7E-06	1.2E-05	1.5	1.2
0.3	105	8.1E-06	1.2E-05	1.2	1.2
0.3	192	2.5E-05	3.8E-05	2.3	1.2
0.3	194	4.1E-05	6.3E-05	4.5	1.2
0.3	195	3.9E-05	5.9E-05	3.5	1.2
0.3	250	9.6E-05	1.5E-04	4.5	1.2
1	26	3.8E-06	9.6E-05	0.6	5.0
1	45	7.4E-06	1.8E-04	1.8	5.0
1	54	1.1E-05	2.6E-04	1.4	5.0
1	79	1.8E-05	4.5E-04	1.6	5.0
1	81	1.9E-04	4.8E-03	4.0	5.0
1	98	3.4E-05	8.4E-04	1.4	5.0
1	163	1.1E-04	2.8E-03	3.1	5.0
1	200	1.9E-04	4.7E-03	7.0	5.0
7	19	2.4E-05	1.2E-03	31.2	7.1

Melt fraction (%)	A1	Unc in A1 ($\mu\text{m}^3/\text{MPa s}$)	A3	Unc in A3 ($1/\text{MPa}^3 \text{ s}$)	A2	Unc in A2 ($\mu\text{m}^2/\text{MPa}^2 \text{ s}$)
0	3.89E-08	2.72E-08	4.51E-12	5.54E-13	1.21E-09	7.38E-11
0.03					6.04E-09	1.10E-09
0.1	6.37E-08	2.57E-08	5.18E-12	4.49E-13	1.55E-09	6.78E-11
0.3	5.16E-08	1.30E-08	3.81E-12	7.63E-13	1.22E-09	1.35E-10
1	1.30E-07	1.15E-08	2.05E-11	3.73E-13	4.50E-09	1.58E-10

Table 3. Flow law constants for Al/Ca-doped Fo samples. parameters for the different flow laws are summarized in Table 3. Even after normalizing the strain rate to a grain size of $d = 2 \mu\text{m}$, the data from the sample with 0.03 vol % melt plot weaker than all but the data for the sample with 1 vol%, as illustrated in Figure 13. As these samples were created first, if they contained more than 0.03 vol% melt, all the higher melt fraction samples would be enriched by the same amount.

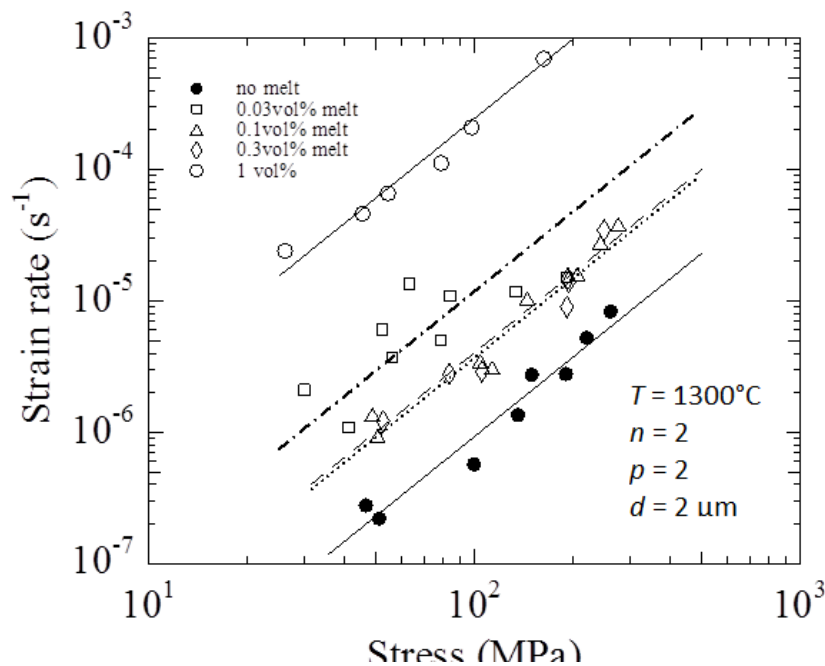


Figure 13. Flow law with $n = 2$, $p = 2$ fit to the data from samples with different melt fractions. Normalizing to $d = 2 \mu\text{m}$ separates out the data so that individual fits are visible. Data from the experiments on samples with 0.03 vol% melt plot anomalously high.

4.9 Discussion

Current flow laws incorporating the weakening effect of melt on viscosity predict an exponential dependence on melt fraction as in Eq. 1, with values of α as low as 21 for diffusion creep and as high as 45 for dislocation creep (Zimmerman and Kohlstedt, 2004; Keleman, 1997). To see if our samples with very small melt fractions conform to these expectations, in Figure 14 we plotted normalized viscosity versus melt fraction for flow laws with $n=1$, $n=3$, and $n=2$ along with the bounds of $\alpha = 21$ and $\alpha = 45$, where normalized viscosity is defined as

$$\eta_{\text{normalized}} = \frac{\dot{\epsilon}_{\text{melt}}}{\dot{\epsilon}_{\text{no melt}}} = e^{-\alpha\phi} \quad (2)$$

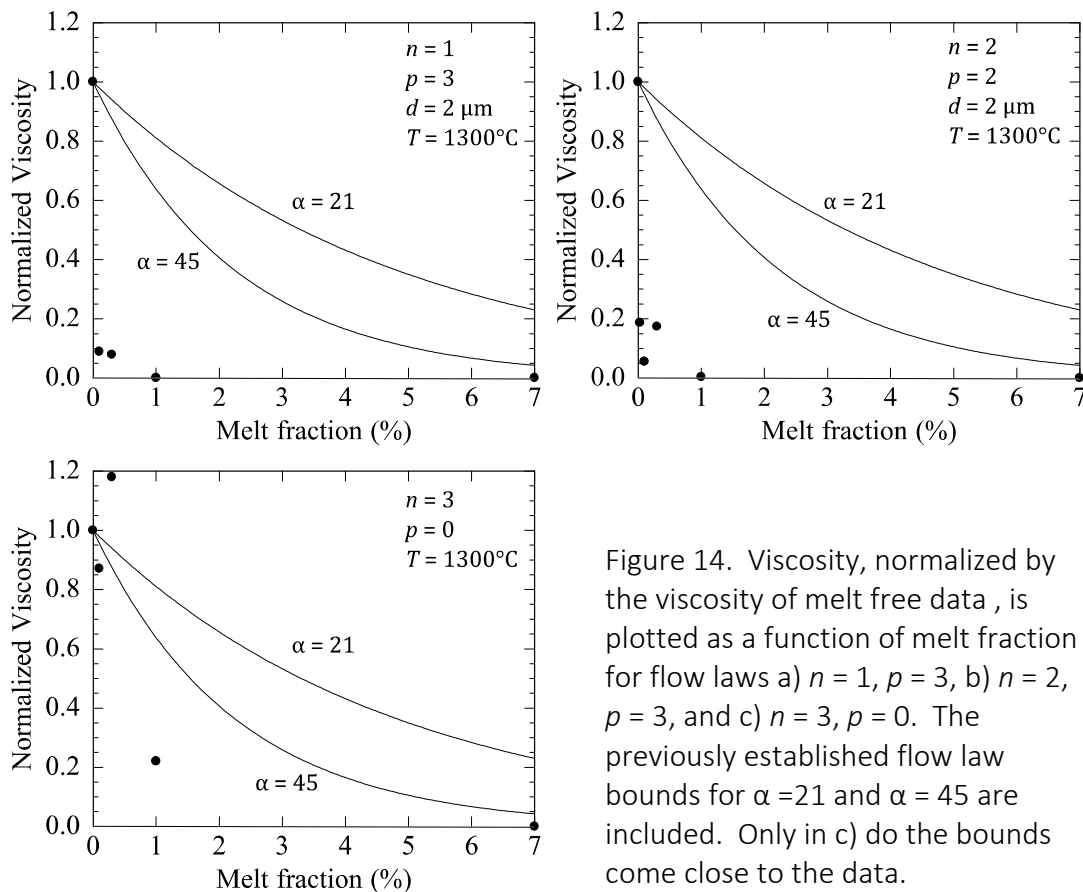


Figure 14. Viscosity, normalized by the viscosity of melt free data, is plotted as a function of melt fraction for flow laws a) $n = 1$, $p = 3$, b) $n = 2$, $p = 3$, and c) $n = 3$, $p = 0$. The previously established flow law bounds for $\alpha = 21$ and $\alpha = 45$ are included. Only in c) do the bounds come close to the data.

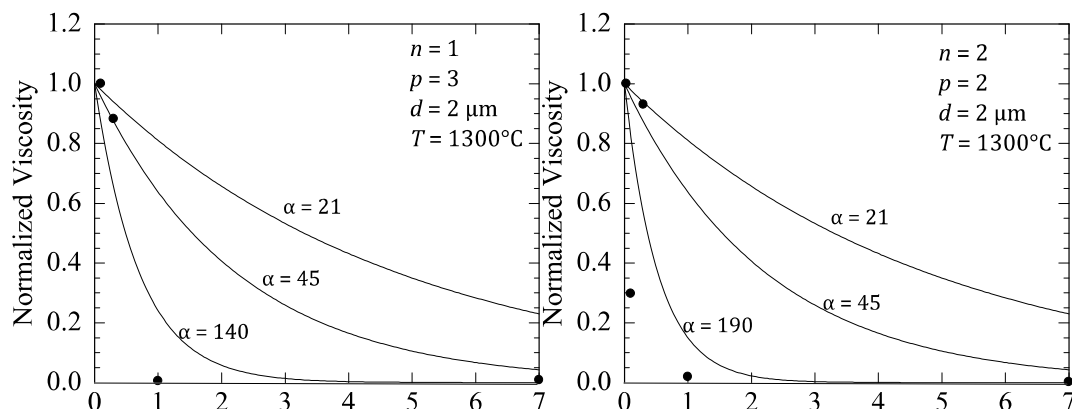


Figure 15. Viscosity normalized by the viscosity of the lowest melt fraction sample, for the case with viscosities derived from a) diffusion creep, $n = 1$, $p = 3$ fits and b) Rachinger sliding $n = 2$, $p = 2$ fits.

In Figure 14a, for $n = 1$, the bounds do not adequately describe the drop in viscosity due to these small amounts of melt. For samples with melt fractions $>0\%$, the bound for $\alpha = 21$ does not do a terrible job encompassing the slope of the data, which argues for the explanation made by Faul and Jackson (2007) that all natural olivines have a small amount of melt. If the melt free samples used for normalization actually contained very small amounts of melt, the normalized viscosities would be higher and would be closer to fitting the existing values of α . In Figure 15, the 0% melt samples were eliminated and the viscosities were normalized by the viscosity of the lowest melt fraction sample. This figure also contains the non-linear least square fit for α . In Figure 15a for the fit using $n = 1$, $p = 3$, the data points at $\phi = 0.01$ and 0.07 lie below the established bounds, which increases the best fit for α to 140 ± 110 . For $n = 2$, $p = 2$ in Figure 15b, the best fit for α is 190 ± 150 . For the fit using $n = 3$ and $p = 0$, the weakening effect of the melt is

less extreme. The scatter in the data is larger, but, within error, the data would fall within the bounds $21 < \alpha < 45$, in Figure 14c.

The decrease in viscosity with increasing melt fraction observed here is not as gradual as predicted in Takei and Holtzman (2009), especially for the fine grain size of our samples. However, these data do support the idea that there is a $\phi_{\text{crit, low}}$, below which there is a dramatic change in strength with a very small change in melt fraction. This behavior indicates that, at the onset of melting in the mantle, the strength of the

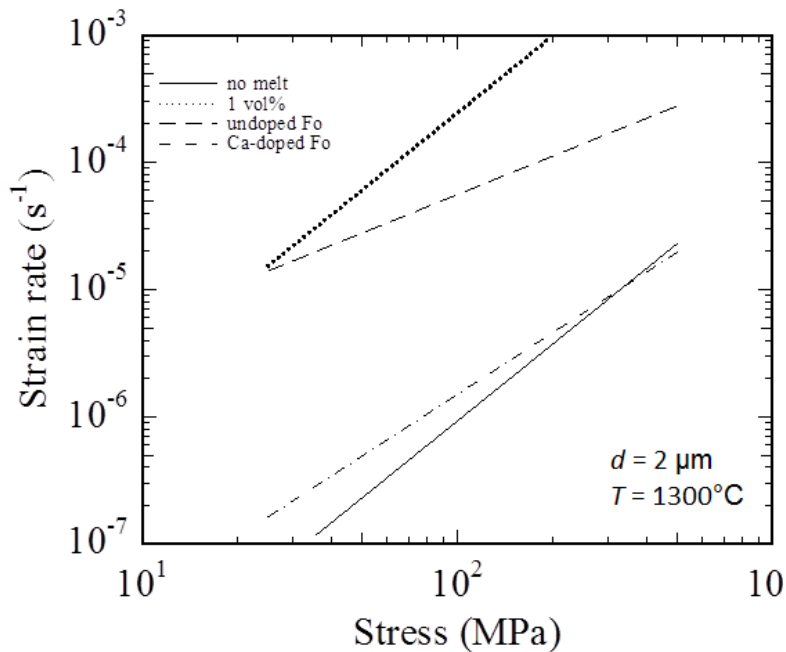


Figure 16. Comparison of the creep strength Ca/Al-doped Fo with 0% melt, Ca/Al-doped Fo with 1% melt, 0.1 mol% Ca-doped Fo, and undoped Fo. The Ca bearing, no melt samples have similar strengths, and the sample with 1% melt is weaker than the other samples.

surrounding rock would decrease by roughly a factor of 5.

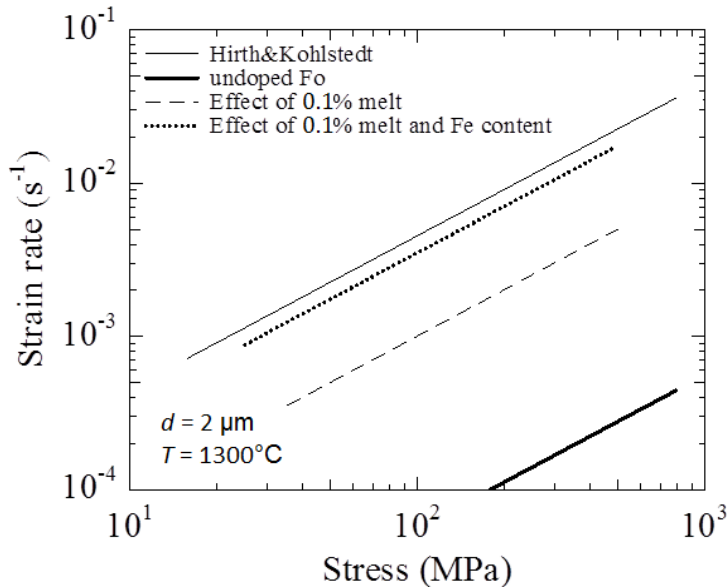


Figure 17. The thin line represents the creep strength of natural San Carlos olivine and the thick line represents the creep strength of high-purity synthetic forsterite. The dashed line represents the weakening effect on forsterite due to 0.3 mol% melt, and the dotted line includes weakening due to melt as well as iron.

It is important to distinguish the effect of changing composition from the effect of adding melt has on creep strength. If the effect of changing trace element concentration on strength was not considered, one would compare the data from samples with 1 vol% melt with the data from samples of undoped forsterite, as in Figure 16. The result would be a very different weakening effect when comparing results from samples with 1 vol% melt with data from melt-free Ca/Al-doped forsterite samples of the same composition. The Ca-doped forsterite samples have a similar strength to the melt-free forsterite with Ca and Al, indicating that the latter is truly melt-free. The effect of composition is not enough on its own to explain the difference in strength between sol-gel and natural olivine samples. If one adds in the effect of melt, natural and pure synthetic samples come into agreement. In a plot of strain rate versus stress, Figure 17 has two solid lines; the thin line represents the data from Hirth and Kohlstedt (1995) for natural olivine, and the thick line represents the purely synthetic forsterite of this study. The effect of 0.1 vol% melt brings the thick line to the dashed line, which is

close but not fully in agreement with natural sample data. The lack of iron in the samples of the study makes them stronger (Zhao et al. 2009). When accounting for the weakening effect of 10 mol% Fe, the dashed line turns into the dotted line, which is in good agreement with Hirth and Kohlstedt. It seems likely, then, that studies of natural samples never had truly melt-free polycrystalline olivine.

Chapter 5: Future Work

5.1 Grain Boundary Sliding

The methodology created for calculating the strain due to grain boundary sliding (GBS) in diffusion creep is valid for measuring strain due to GBS in any deformation mechanism. Dislocation accommodated grain boundary sliding (disGBS) has two sets of empirical flow law variables (n , p , and Q), depending on whether the grain size is larger or smaller than the theoretical sub-grain size. If the deforming sample has a grain size less than the sub-grain size, then $n = 2$, $p = 2$, and Q is equivalent to that of the grain boundary diffusion coefficient for the rate limiting species. If the deforming sample has a grain size greater than the sub-grain size, then $n = 3$, $p = 1$, and Q is equivalent to that of the lattice diffusion coefficient for the rate limiting species (Langdon, 2006). The larger grained samples appear to deform more like dislocation creep, which would mean a great deal of intra-crystalline deformation, while the smaller grain samples appear to deform more like diffusion creep, which would mean the deformation is more localized near the grain boundaries. Being able to confirm this change in deformation would go a long way in explaining the theory behind these different variables.

There are two ways to go about measuring strain due to GBS in the disGBS field. The first method involves scribing lines on the polished surface of a sample, and then filling these lines with a metal that adheres to the surface. A grid of finely spaced lines allow a measure of the deformation within the grains as well as lateral GBS (Quintanilla Termini, 2014), while the established method using atomic force microscopy measures vertical GBS. This method would allow one to distinguish between different

accommodation mechanisms for GBS. In order to deform in the disGBS field, fine grained, high purity forsterite (Fo) would be loaded to the high stress necessary and would undergo a single strain step, as multiple heating and cooling steps would cause fracture. The second method would involve deforming forsterite doped with Pr. Deformation experiments on Pr-doped Fo, showed a transition from diffusion creep to a dislocation driven mechanism at lower stresses than undoped Fo. At these lower stresses, the samples are unlikely to crack. However, as the addition of Pr changes the deformation strength of Fo, one would have to characterize the strain due to GBS in diffusion creep of the doped Fo. The increase in strength of Pr-doped Fo over undoped Fo might be due to a great change in grain boundary viscosity.

A different change in composition which should be considered when characterizing the contribution of grain boundary sliding is a second crystalline phase. Olivine makes up ~60% of the upper mantle, making polyphase deformation is more representative of deformation in the Earth. A number of studies have shown that deformation of a mixture of olivine and pyroxene are weaker than a rock made up of only one (Sundberg and Cooper, 2008; Tasaka et al. 2013). A study of grain boundary sliding on a ceramic of mixed alumina and zirconia showed increased contribution of sliding to the total strain (Clarisse et al., 2000), suggesting that phase boundaries are easier to slide on than grain boundaries. Testing this result in an olivine/pyroxene mixture could help explain the weakness of the mixture over the pure end members.

5.2 Changing Grain Boundary Composition

The grain boundaries have been posited as storage sites for incompatible elements (Hiraga et al., 2004). Although the doped Fo in this study was always stronger than the

undoped Fo, a number of cation impurities should decrease the strength of Fo. In ceramics such as alumina, cations smaller than the lattice site they occupy weaken the ceramic (Yoshida et al. 1998), so cations smaller than Mg^{2+} could cause a weakening effect. A complication in attempting to dope with cations smaller than Mg^{2+} is that none of the cations naturally occur in octahedral coordination. This implies that these smaller cations are likely to sit on the tetrahedrally coordinated Si^{4+} site, which complicates comparison to doping with larger cations. Instead of a change in size to a smaller cation, a change in the charge of the cation could weaken olivine. This study found that a 3+ cation on the 2+ site created an additional strengthening effect. Attempting a 1+ cation on the Mg^{2+} site should have the opposite effect, and would thus make the sample weaker. The only 1+ cation smaller than octahedrally coordinated Mg^{2+} is H^+ (Shannon, 1976), which has been shown in a number of studies to weaken olivine (Mackwell et al., 1985; Karato et al., 1986; Karato, 1998; Mei et al. 2002). Octahedrally coordinated Li^+ is roughly the same size as Mg^{2+} , and Na^+ is roughly the same size as Ca^{2+} . The comparison between undoped or Ca doped Fo, respectively, would allow one to determine the effect of 1+ cations in Mg^{2+} sites. An understanding of these types of impurities will allow experimentalists to more confidently compare results on materials with slightly different compositions.

5.3 Melt

In this study, the presence of small amounts of melt has been shown to have a dramatic effect on the viscosity of olivine. The goal of the experiments in this study was to determine the change in diffusion creep viscosity due to melt, as predicted in Takei and

Holtzman (2009), which necessitates a very fine grain size. Extrapolating to the larger grain sizes of the mantle will result in a change in the effect of the melt. The volume of triple junctions available for melt in samples with a 1 μm grain size is orders of magnitude greater than the volume available for samples with a grain size of 1 mm. A more fundamental understanding of the effect on creep strength of changing grain size in partially molten olivine is necessary before apply the results of this study to the mantle.

A question currently under investigation is how is the very small amount of melt in the mantle extracted rapidly enough to maintain chemical disequilibria (Aharonov et al., 1995; Kelemen et al., 1997). Melt traveling through triple junctions does not move fast enough (Spiegelman and Kenyon, 1992). A number of experiments have studied the development of channels (Holtzman et al. 2003; King et al., 2009) and the alignment of melt pockets (Kohlstedt and Zimmerman, 1996; Pec et al. 2016) at high melt fractions, but no experiments have shown the extraction of melt fractions < 0.01 . As, at high melt fractions, these melt bands do not develop until strains of at least $\epsilon = 1$ (King et al., 2009; Qi et al., 2013), high strain experiments on small melt fraction samples is necessary. Determining whether the small amount of melt in these samples focusses into bands is key to determining the extraction path of melt from the mantle.

Bibliography

- Aharanov, E., J.A. Whitehead, P.B. Kelemen, and M. Spiegelman (1995) Channeling instability of upwelling melt in the mantle, *Journal of Geophysical Research*, **100**, pp. 20433-20450
- Akaogi, M., E. Ito, and A. Navrotsky (1989) Olivine-modified spinel-spinel transitions in the system Mg_2SiO_4 - Fe_2SiO_4 : Calorimetric measurements, thermochemical calculation, and geophysical application, *Journal of Geophysical Research*, **94**, pp. 15671-15685
- Altay, A. & M.A. Gülgün (2003) Microstructural Evolution of Calcium-Doped α -Alumina, *Journal of the American Ceramic Society*, **86**, pp. 623-29
- Anderson, D.L. and C. Sammis (1970) Partial melting in the upper mantle, *Physics of the Earth and Planetary Interiors*, **3**, pp. 41-50
- Andersson, K. G. Borchardt, S. Scherrer, and S. Weber (1989) Self-diffusion in Mg_2SiO_4 (forsterite) at high temperature: A model case study for SIMS analyses on ceramic surfaces, *Fresenius Zeitschrift fuer Analytische Chemie*, **333**, pp. 383-385
- Ashby, M.F. (1972) Boundary Defects, and Atomistic Aspects of Boundary Sliding and Diffusional Creep. *Surface Science*, **31**, pp.498-542
- Ashby, M.F. and R.A. Verrall (1973) Diffusion-Accommodated Flow and Superplasticity. *Acta Metallurgica*, **21** pp. 149-163
- Bai, Q., S.J. Mackwell, and D.L. Kohlstedt (1991) High-Temperature Creep of Olivine Single Crystals 1. Mechanical Results for Buffered Samples, *Journal of Geophysical Research*, **96**, pp. 2441-2463
- Barnhoorn, A., I. Jackson, J.D. FitzGerald, and Y. Aizawa (2007) Suppression of elastically accommodated grain-boundary sliding in high-purity MgO, *Journal of the European Ceramic Society*, **27**, pp. 4697-4703
- Baxter, E.F., P.D. Asimow, and K.A. Farley (2007) Grain boundary partitioning of Ar and He, *Geochimica et Cosmochimica Acta*, **71**, pp. 434-451
- Beattie, P. (1994) Systematics and energetics of trace-element partitioning between olivine and silicate melts: Implications for the nature of mineral/melt partitioning, *Chemical Geology*, **117**, pp. 57-71
- Beere, W. (1978) Stresses and Deformation at Grain Boundaries. *Philosophical Transactions of the Royal Society of London. Series A, Mathematical and Physical Sciences*, **288**, pp 177-195.
- Bell, R.L. and C. Graeme-Barber (1970) Surface and Interior Measurements of Grain Boundary Sliding During Creep, *Journal of Materials Science*, **5**, pp. 933-944
- Bell, R.L., C. Graeme-Barber, and T.G. Langdon (1967) The Contribution of Grain Boundary Sliding to the Overall Strain of a Polycrystal, *Transactions of the Metallurgical Society of AIME*, **239**, pp. 1821-1824

- Berger, A., M. Herwegh, J. Schwarz, B. Pulitz (2011), Quantitative analysis of crystal/grain sizes and their distributions in 2D and 3D, *Journal of Structural Geology*, **33**, pp. 1751-1763
- Boullier, A.M. and Y. Gueguen (1975) SP-Mylonites: Origin of Some Mylonites by Superplastic Flow, *Contributions to Mineralogy and Petrology*, **50**, pp. 93-104
- Braun, M.G., G. Hirth, and E.M. Parmentier (2000) The effects of deep damp melting on mantle flow and melt generation beneath mid-ocean ridges, *Earth and Planetary Science Letters*, **176**, pp.339-356
- Chang, and L.J. Graham (1966) Edge Dislocation Core Structure and the Peierls Barrier in Body-Centered Cubic Iron, *Physica and Status Solidi*, **18**, pp. 99-103
- Chopara, P.N. and M.S. Paterson (1981) The experimental deformation of dunite, *Tectonophysics*, **78**, pp. 453-473
- Clarisse, L., A. Bataille, Y. Pennec, J. Crampon, and R. Duclos (1999) Investigation of grain boundary sliding during superplastic deformation of a fine-grained alumina by atomic force microscopy, *Ceramics International*, **25**, pp. 389-394
- Clarisse, L., F. Petit, J. Crampon, and R. Duclos (2000) Characterization of grain boundary sliding in a fine-grained alumina-zirconia ceramic composite by atomic force microscopy, *Ceramics International*, **26**, pp.295-302
- Cmiral, M., J.D. FitzGerald, U.H. Faul, and D.H. Green (1997) A close look at dihedral angles and melt geometry in olivine-basalt aggregates: a TEM study, *Contributions to Mineralogy and Petrology*, **130**, pp. 336-345
- Cooper, R.F. (1990) Differential Stress-Induced Melt Migration: An Experimental Approach, *Journal of Geophysical Research*, **95**, pp. 6979-6992
- Cooper, R.F. and D.L. Kohlstedt (1984) Solution-precipitation enhanced diffusional creep of partially molten olivine-basalt aggregates during hot-pressing, *Tectonophysics*, **107**, pp. 207-233
- Cooper, R.F. and D.L. Kohlstedt (1986) Rheology and Structure of Olivine-Basalt Partial Melts, *Journal of Geophysical Research*, **91**, pp. 9315-9323
- Daines, M.J. and D.L. Kohlstedt (1994) The transition from porous to channelized flow due to melt/rock reaction during melt migration, *Geophysical Research Letters*, **21**, pp. 145-148
- Dillon, S.J. and M.P. Harmer (2007) Multiple grain boundary transitions in ceramics: A case study of alumina, *Acta Materialia*, **55**, pp. 5247-5254
- Dillon, S.J. and M.P. Harmer (2008) Relating Grain-Boundary Complexion to Grain-Boundary Kinetics I: Calcia-Doped Alumina, *Journal of the American Ceramic Society*, **91**, pp. 2304-2313
- Drury, M.R. and J.D. FitzGerald (1996) Grain boundary melt films in an experimentally deformed olivine-orthopyroxene rock: implications for melt distribution in upper mantle rocks., *Geophysical Research Letters*, **23**, pp. 701-704

- Dunn, R.A., V. Lekic, R.S. Detrick, and D.R. Toomey (2005) Three-dimensional seismic structure of the Mid-Atlantic Ridge (35°N): Evidence for focused melt supply and lower crustal dike injection, *Journal of Geophysical Research*, **110**, B09101, doi:10.1029/2004JB003473.
- Durand G., J. Weiss, V., Lipenkov, J.M. Barnola, G. Krinner, F. Parrenin, B. Delmonte, C. Ritz, P. Duval, R. Roethlisberger, M. Bigler (2006) Effect of impurities on grain growth in cold ice sheets, *Journal of Geophysical Research*, **111**, F01015
- Etheridge, M.A. and J.C. Wilkie (1979) Grainsize Reduction, Grain Boundary Sliding and the Flow Strength of Mylonites, *Tectonophysics*, **58**, pp 159-178
- Evans, A.G. (1978) Microfracture from thermal expansion anisotropy -- I. Single phase systems, *Acta Metallurgica*, **26**, pp. 1845-1853
- Farver, J.R. and R.A. Yund (2000) Silicon diffusion in forsterite aggregates: Implications for diffusion accommodated creep, *Geophysical Research Letters*, **27**, pp. 2337-2340
- Faul, U. H., and I. Jackson (2007), Diffusion creep of dry, melt-free olivine, *Journal of Geophysical Research*, **112**, B04204, doi:10.1029/2006JB004586
- Faul, U.H. (2001) Melt retention and segregation beneath mid-ocean ridges, *Nature*, **410**, pp. 920-923
- Faul, U.H. and D. Scott (2006) Grain growth in partially molten olivine aggregates, *Contributions to Mineralogy and Petrology*, **151**, pp. 101-111
- Faul, U.H. and I. Jackson (2007) Diffusion creep of dry, melt-free olivine, *Journal of Geophysical Research*, **112**, B04204, doi:10.1029/2006JB004586
- Faul, U.H., J.D. Fitz Gerald, and I. Jackson (2004) Shear wave attenuation and dispersion in melt-bearing olivine polycrystals: 2. Microstructural interpretation and seismological implications, *Journal of Geophysical Research*, **109**, B06202, doi:10.1029/2003JB002407
- Fei, H., C. Hegoda, D. Yamazaki, M. Wiedenbeck, H. Yurimoto, S. Shcheka, and T. Katsura (2012) High silicon self-diffusion coefficient in dry forsterite, *Earth and Planetary Science Letters*, **345-348**, pp. 95-103
- Fliervoet, T.F. and S.H. White (1995) Quartz deformation in a very fine grained quartz-feldspathic mylonite: a lack of evidence for dominant grain boundary sliding deformation, *Journal of Structural Geology*, **17**, pp. 1095-1109
- Garapic, G., U.H. Faul, and E. Brisson (2013) High-resolution imaging of melt distribution in partially molten upper mantle rocks: evidence for wetted two-grain boundaries, *Geochemistry, Geophysics, Geosystems*, **14(3)**, pp. 556-566
- Gates, R.S. and R.N. Stevens (1974) The Measurement of Grain Boundary Sliding in Polycrystals. *Metallurgical Transactions*, **5**, pp 505-510
- Ghosh, A.K. and R. Raj (1981) Grain Size Distribution Effects in Superplasticity, *Acta Metallurgica*, **29**, pp 607-616
- Gifkins, R.C. (1977) The Effect of Grain Size and Stress Upon Grain-Boundary Sliding, *Metallurgical Transactions A*, **8A**, pp 1507-1517

- Gillet, P., P. Richet, F. Guyot, and G. Fiquet (1991) High-Temperature Thermodynamic Properties of Forsterite, *Journal of Geophysical Research*, **96**, pp. 11805-11816
- Goetze, C. (1978) The Mechanisms of Creep in Olivine, *Philosophical Transactions of the Royal Society of London. Series A, Mathematical and Physical Sciences*, **288**, pp. 99-119
- Goldsby, D.L. and D.L. Kohlstedt (2001) Superplastic deformation of ice: Experimental observations, *Journal of Geophysical Research*, **106**, pp. 11017-11030
- Gordon, R.S. (1973) Mass transport in the diffusional creep of ionic solids, *Journal of the American Ceramic Society*, **56**, pp. 147-152
- Green, T.H. (1981) Experimental evidence for the role of accessory phases in magma genesis, *Journal of Volcanology and Geothermal Research*, **10**, pp. 405-422
- Gülgün, M.A., R. Voytovych, I. Maclaren, and M. Rühle (2002) Cation Segregation in an Oxide Ceramic with Low Solubility: Yttrium Doped α -Alumina, *Interface Science*, **10**, pp.99-110
- Han, J. & D. Kim (1998) Determination of three-dimensional grain size distribution by linear intercept measurement, *Acta Materialia*, **46**, pp. 2021-2028
- Hansen, L.N., M.E. Zimmerman, A.M. Dillman, and D.L. Kohlstedt (2012) Strain localization in olivine aggregates at high temperature: A laboratory comparison of constant-strain-rate and constant-stress boundary conditions, *Earth and Planetary Science Letters*, **333-334**, pp. 134-145
- Hansen, L.N., M.E. Zimmerman, and D.L. Kohlstedt (2011) Grain boundary sliding in San Carlos olivine: Flow law parameters and crystallographic-preferred orientation, *Journal of Geophysical Research*, **116**, pp. B08201
- Haugstad, Greg (2012) Atomic Force Microscopy: Understanding Basic Modes and Advanced Applications. Hoboken (USA): Wiley. Chapter 4 Topographic Imaging; pp 137-186
- Heilbronner, R & S. Barrett (2014) Image Analysis in Earth Sciences: Microstructures and Textures of Earth Materials. Berlin(Germany): Springer. Chapter 11 2-D Grain Size Distributions; pp. 187-199
- Hermann, J., H.S.C. O'Neill, and A.J. Berry (2005) Titanium solubility in olivine in the system TiO₂-MgO-SiO₂: no evidence for an ultra-deep origin of Ti-bearing olivine, *Contributions to Mineralogy and Petrology*, **148**, pp. 746-760
- Herring, C. (1950) Diffusional viscosity of a polycrystalline solid, *Journal of Applied Physics*, **21**, pp. 437-445
- Hier-Majumder, S. and A. Courtier (2011) Seismic signature of small melt fraction atop the transition zone, *Earth and Planetary Science Letters*, **308**, pp. 334-342
- Hier-Majumder, S., Y. Ricard, and D. Bercovici (2006) Role of grain boundaries in magma migration and storage, *Earth and Planetary Science Letters*, **248**, pp. 735-749
- Hiraga, T. and D.L. Kohlstedt (2007) Equilibrium interface segregation in the diopside-forsterite system I: Analytical techniques, thermodynamics, and segregation characteristics, *Geochimica et Cosmochimica Acta*, **71**, pp. 1266-1280

- Hiraga, T. and D.L. Kohlstedt (2009) Systematic distribution of incompatible elements in mantle peridotite: importance of intra-and inter-granular melt-like components, *Contributions to Mineralogy and Petrology*, **158**, pp. 149-167
- Hiraga, T., C. Tachibana, N. Ohashi, S. Sano (2010), Grain growth systematics for forsterite ± enstatite aggregates: Effect of lithology on grain size in the upper mantle, *Earth and Planetary Science Letters*, **291**, pp 10-20
- Hiraga, T., I.M. Anderson, D.L. Kohlstedt (2004) Grain boundaries as reservoirs of incompatible elements in the Earth's mantle, *Nature*, **427**, pp 699-703
- Hiraga, T., I.M. Anderson, M.E. Zimmerman, S. Mei, and D.L. Kohlstedt (2002) Structure and chemistry of grain boundaries in deformed, olivine + basalt and partially molten lherzolite aggregates: evidence of melt-free grain boundaries, *Contributions to Mineralogy and Petrology*, **144**, pp. 163-175
- Hiraga, T., M.M. Hirschmann, and D.L. Kohlstedt (2007) Equilibrium interface segregation in the diopside-forsterite system II: Applications of interface enrichment to mantle geochemistry, *Geochimica et Cosmochimica Acta*, **71**, pp. 1281-1289
- Hiraga, T., T. Miyazaki, M. Tasaka, and H. Yoshida (2010) Mantle superplasticity and its self-made demise, *Nature*, **468**, pp. 1091-1094
- Hirsch, L.M. and T.J. Shankland (1993) Quantitative olivine-defect chemical model: insights on electrical conduction, diffusion, and the role of Fe content, *Geophysical Journal International*, **114**, pp. 21-35
- Hirth, G. and D.L. Kohlstedt (1995) Experimental constraints on the dynamics of the partially molten upper mantle: Deformation in the diffusion creep regime, *Journal of Geophysical Research*, **100**, pp. 1981-2001
- Hirth, G. and D.L. Kohlstedt (1996) Water in the oceanic upper mantle: implications for rheology, melt extraction and the evolution of the lithosphere, *Earth and Planetary Science Letters*, **144**, pp. 93-108
- Hirth, G. and D.L. Kohlstedt (2003) Rheology of the Upper Mantle and the Mantle Wedge: A View from the Experimentalists, in *Inside the Subduction Factory* (ed J. Eiler), American Geophysical Union, Washington, D. C., doi: 10.1029/138GM06
- Holtzman, B.K. (2015) Questions on the existence, persistence, and mechanical effects of a very small melt fraction in the asthenosphere, *Geochemistry, Geophysics, Geosystems*, **17**, pp. 470-484
- Holtzman, B.K., N.J. Groebner, M.E. Zimmerman, S.B. Ginsberg, and D.L. Kohlstedt (2003) Stress-driven melt segregation in partial molten rocks, *Geochemistry Geophysics Geosystems*, **4(5)**
- Houlier, B. M. Cheraghmakani, and O. Jaoul (1990) Silicon diffusion in San Carlos olivine, *Physics of the Earth and Planetary Interiors*, **62**, pp. 329-340
- Hustoft, J., T. Scott, and D.L. Kohlstedt (2007) Effect of metallic melt on the viscosity of peridotite, *Earth and Planetary Science Letters*, **260**, pp. 355-360

- Ikuhara, Y., H. Yoshida, and T. Sakuma (2001) Impurity effects on grain boundary strength in structural ceramics, *Materials Science and Engineering*, **A319-321**, pp. 24-30
- Jackson, I., U.H. Faul, and R. Skelton (2014) Elastically accommodated grain-boundary sliding: New insights from experiment and modeling, *Physics of the Earth and Planetary Interiors*, **228**, pp. 203-210
- Johnson, D. Lynn (1969) New Method of Obtaining Volume, Grain Boundary, and Surface Diffusion Coefficients from Sintering Data, *Journal of Applied Physics*, **40**, pp. 192-200
- Johnson, W.C. (1970) Grain Boundary Segregation in Ceramics, *Metallurgical Transactions A*, **8A**, pp. 1413-1422
- Karato, S.I. (1986) Does partial melting reduce the creep strength of the upper mantle, *Nature*, **319**, pp. 309-310
- Karato, S.I., and H. Jung (1998) Water, partial melting and the origin of the seismic low velocity and high attenuation zone in the upper mantle, *Earth and Planetary Science Letters*, **157**, pp. 193-207
- Karato, S.I., M.S. Paterson, and J.D. FitzGerald (1986) Rheology of synthetic olivine aggregates: influence of grain size and water, *Journal of Geophysical Research: Solid Earth*, **91(B8)**, pp. 8151-8176
- Karato, S.I., S. Zhang, and H-R. Wenk (2005) Superplasticity in Earth's Lower Mantle: Evidence from Seismic Anisotropy and Rock Physics, *Science*, **270**, pp. 458-461
- Kawakatsu, H., P. Kumar, Y. Takei, M. Shinohara, T. Kanazawa, E. Araki, and K. Suyehiro (2009) Seismic Evidence for Sharp Lithosphere-Asthenosphere Boundaries of Oceanic Plates, *Science*, **324**, pp. 499-502
- Kublinski, P., D. Wolf, S.R. Phillpot, and H. Gleiter (1999) Self-diffusion in high-angle fcc metal grain boundaries by molecular dynamics simulation, *Philosophical Magazine A*, **79**, pp. 2735-2761
- Kelemen, P.B., G. Hirth, N. Shimizu, M. Spiegelman, and H.J.B. Dick (1997) A review of melt migration processes in the adiabatically upwelling mantle beneath oceanic spreading ridges, *Philosophical Transactions: Mathematical, Physical, and Engineering Sciences*, **355**, pp. 283-318
- Kelly, A. and G.W. Groves (1970) Crystallography and Crystal Defects. Longman Group Ltd., Chichester, pp. 356-357
- King, D.S.H, M.E. Zimmerman, and D.L. Kohlstedt (2009) Stress-driven Melt segregation in Partially Molten Olivine-rich Rocks Deformed in Torsion, *Journal of Petrology*, **51**, pp. 21-42
- Kohlstedt, DL and M.E. Zimmerman (1996) Rheology of partially molten mantle rocks, *Annual Reviews of Earth and Planetary Science*, **24**, pp. 41-62
- Kottada R.S. and A.H. Chokshi (2007) Grain Boundary Sliding during Diffusion and Dislocation Creep in a Mg-0.7 Pct Al Alloy, *Metallurgical and Materials Transactions A*, **38A**, pp. 1743-1749

- Kroeger, F.A. and H.J. Vink (1956) Relations between the Concentrations of Imperfections in Crystalline Solids, *Solid State Physics*, **3**, pp. 307-435
- Langdon, T.G (1994) A Unified Approach to Grain Boundary Sliding in Creep and Superplasticity, *Acta Metallurgica Materialia*, **42**, pp. 2437-2443
- Langdon, T.G. (1972) The Effect of Surface Configuration on Grain Boundary Sliding, *Metallurgical Transactions*, **3**, pp. 797-801
- Langdon, T.G. (2006) Grain boundary sliding revisited: Developments in sliding over four decades, *Journal of Material Science*, **41**, pp. 597-609
- Langmuir, C.H., E.M. Klein, and T. Plank (1993) Petrological systematics of mid-ocean ridge basalts: Constraints on melt generation beneath ocean ridges, Mantle flow and melt generation at mid-ocean ridges, pp. 183-280
- Langmuir, C.H., J.F. Bender, A.E. Bence, G.N. Hanson, and S.R. Taylor (1977) Petrogenesis of basalts from the FAMOUS area: Mid-Atlantic Ridge, *Earth and Planetary Science Letters*, **36**, pp. 133-156
- Lifshitz, I.M. (1963) On the theory of diffusion-viscous flow of polycrystalline bodies, *Soviet Physics Journal of Experimental and Theoretical Physics*, **17**, pp. 1349-1367
- Mackwell, S.J., D.L. Kohlstedt, and M.S. Paterson (1985) The role of water in the deformation of olivine single crystals, *Journal of Geophysical Research: Solid Earth*, **90(B13)**, pp. 11319-11333
- McKenzie, D. (1989) Some remarks on the movement of small melt fractions in the mantle, *Earth and Planetary Science Letters*, **95**, pp. 53-72
- McKenzie, D. (2000) Constraints on melt generation and transport from U-series activity ratios, *Chemical Geology*, **162**, pp.81-94
- McLean, D. (1957) Grain Boundaries in Metals, Oxford University Press, Oxford
- McNee K.R., G.W. Greenwood, and H. Jones (2001) Microstructural Evidence for Diffusional Creep in Copper Using Atomic Force Microscopy, *Scripta Materialia*, **44**, pp. 351-357
- Mei, S. and D.L. Kohlstedt (2000) Influence of water on plastic deformation of olivine aggregates 1. Diffusion creep regime, *Journal of Geophysical Research*, **105**, pp. 21457-21469
- Mendelson, M. I. (1969) Average Grain Size in Polycrystalline Ceramics, *Journal of the American Ceramic Society*, **52**, pp. 443-446
- Mimurada, J., M. Nakano, K. Sasaki, Y. Ikuhara, and T. Sakuma (2001) Effect of Cation Doping on the Superplastic Flow in Yttria-Stabilized Tetragonal Zirconia Polycrystals, *Journal of the American Ceramic Society*, **84**, pp. 1817-1821
- Mullins, W.W. (1957) Theory of Thermal Grooving, *Journal of Applied Physics*, **28**, 333
- Nabarro, F.R.N (1948) Deformation of crystals by the motion of single ions, Report of a Conference on Strength of Solids (Bristol). The Physical Society, pp. 75-90

- Nagahara, H., I. Kushiro, and B. O. Mysen (1994) Evaporation of olivine: Low pressure phase relations of the olivine system and its implication for the origin of chondritic components in the solar nebula, *Geochimica et Cosmochimica Acta*, **58**, pp. 1951-1963
- Naif, S., K. Key, S. Constable, and R.L. Evans (2013) Melt-rich channel observed at the lithosphere-asthenosphere boundary, *Nature*, **495(7441)**, pp. 356-359
- Nakajima, J., Y. Takei, and A. Hasegawa (2005) Quantitative analysis of the inclined low-velocity zone in the mantle wedge of northeastern Japan: A systematic change of melt-filled pore shapes with depth and its implications for melt migration, *Earth and Planetary Science Letters*, **234**, pp. 59-70
- Ni, H., H. Keppler, and H. Behrens (2011) Electrical conductivity of hydrous basaltic melts: implications for partial melting in the upper mantle, *Contributions to Mineralogy and Petrology*, **162**, pp. 637-650
- Oxburgh, E. R. (1964) Petrological evidence for the presence of amphiboles in the upper mantle and its petrogenetic and geophysical implications, *Geological Magazine*, **101**, pp. 1-11
- Pec, M., A. Quintanilla Terminel, B. Holtzman, M. Zimmerman, and D. Kohlstedt (2016) Grain-scale alignment of melt in sheared partially molten rocks: implications for viscous anisotropy, Geophysical Research Abstracts, 18 EGU 2016
- Precigout, J. and G. Hirth (2014) B-type olivine fabric induced by grain boundary sliding, *Earth and Planetary Science Letters*, **395**, pp. 231-240
- Qi, C., Y.H. Zhao, and D.L. Kohlstedt (2013) An experimental study of pressure shadows in partially molten rocks, *Earth and Planetary Science Letters*, **382**, pp. 77-84
- Quintanilla Terminel, A. (2014) Strain Heterogeneity during Creep of Carrara Marble (PhD Thesis) Retrieved from <http://hd.handle.net/1721.1/95556>
- Raj, R. (1975) Transient Behavior of Diffusion-Induced Creep and Creep Rupture. *Metallurgical Transactions A*, **6A**, pp. 1499-1509
- Raj, R. and M.F. Ashby (1971) On Grain Boundary Sliding and Diffusional Creep, *Metallurgical Transactions*, **2**, pp 1113-1127
- Revenaugh, J. and S.A. Sipkin (1994) Seismic evidence for silicate melt atop the 410-km mantle discontinuity, *Nature*, **369(6480)**, pp. 474-476
- Sahay, S.S. and G.S. Murty (2001) Uncertainty in separating the strain contributions of sliding and diffusion in diffusional creep, *Scripta Materialia*, **44(5)**, pp. 841-845
- Schmid, S.M., J.N. Boland, and M.S. Paterson (1977) Superplastic Flow in Finegrained Limestone, *Tectonophysics*, **43**, pp. 257-291
- Scott, T. and D.L. Kohlstedt (2006) The effect of large melt fraction on the deformation behavior of peridotite, *Earth and Planetary Science Letters*, **216**, pp. 177-187
- Shannon, R.D. (1976) Revised Effective Ionic Radii and Systematic Studies of Interatomic Distances in Halides and Chalcogenides, *Acta Crystallographica*, **32**, pp. 751-767
- Shen, Y. and Forsyth, D.W. (1995) Geochemical constrains on initial and final depths of melting beneath mid-ocean ridges, *Journal of Geophysical Research: Solid Earth*, **100(B2)**, 2211-2237

- Spandler, C., H. St. C. O'Neill, and V.S. Kamenetsky (2007) Survival times of anomalous melt inclusions from element diffusion in olivine and chromite, *Nature*, **447**, pp. 303-306
- Spiegelman, M. and P. Kenyon (1992) The requirements for chemical disequilibrium during magma migration, *Earth and Planetary Science Letters*, **109**, pp. 611-620
- Sundberg, M., G. Hirth, and P.B. Kelemen (2010) Trapped Melt in the Josephine Peridotite: Implications for Permeability and Melt Extraction in the Upper Mantle, *Journal of Petrology*, **51**, pp. 185-200
- Swain, M.V. and B.K. Atkinson (1978) Fracture Surface Energy of Olivine, *Pure and Applied Geophysics*, **116**, pp. 866-872
- Takei, Y. and B.K. Holtzman (2009) Viscous constitutive relations of solid-liquid composites in terms of grain boundary contiguity: 2. Compositional model for small melt fractions, *Journal of Geophysical Research*, **114**, B06206, doi:10.1029/2008JB005851
- Takei, Y. and S. Hier-Majumder (2009) A generalized formulation of interfacial tension driven fluid migration with dissolution/precipitation, *Earth and Planetary Science Letters*, **288**, pp. 138-148
- Tasaka, M., T. Hiraga, and M.E. Zimmerman (2013), Influence of mineral fraction on the rheological properties of forsterite + enstatite during grain-size-sensitive creep: 2. Deformation experiments, *Journal of Geophysical Research: Solid Earth*, **118**, 3991-4012
- ten Grotenhuis, S., M.R. Drury, C.J. Peach, and C.J. Spiers (2004) Electrical properties of fine-grained olivine: Evidence for grain boundary transport, *Journal of Geophysical Research*, **109**, B06203, doi:10.1029/2003JB002799
- ten Grotenhuis, S., M.R. Drury, C.J. Spiers, and C.J. Peach (2005) Melt distribution in olivine rocks based on electrical conductivity measurements, *Journal of Geophysical Research*, **110**, B12201, doi:10.1029/2004JB003462
- von Bargen, N. and H.S. Waff (1986) Permeabilities, interfacial areas and curvatures of partially molten systems: results of numerical computations of equilibrium microstructures, *Journal of Geophysical Research*, **91**, pp. 9261-9276
- von Mises, R. (1913) Mechanik der festen Koerper im plastisch deformablen Zustand, *Nachrichten von der Gesellschaft der Wissenschaften zu Goettingen, Mathematisch-Physikalische Klasse*, **1**, pp. 582-592
- Waff, H.S. and U.H. Faul (1992) Effects of Crystalline Anisotropy on Fluid Distribution in Ultramafic Partial Melts, *Journal of Geophysical Research*, **97**, pp. 9003-9014
- Wakai, F., T. Nagano, and T. Iga (1997) Hardening in Creep of Alumina by Zirconium Segregation at the Grain Boundary, *Journal of the American Ceramics Society*, **80**, pp.2361-2366
- Walte, N.P., P.D. Bons, and C.W. Passchier (2005) Deformation of melt-bearing systems- insight from in situ grain-scale analogue experiments, *Journal of Structural Geology*, **27**, 1666-1679

- Wark, D.A., C.A. Williams, E.B. Watson, and J.D. Price (2003) Reassessment of pore shapes in microstructurally equilibrated rocks, with implications for the permeability of the upper mantle, *Journal of Geophysical Research*, **108(B1)**, 2050, doi:10.1029/2001JB001575
- Warren, J.M. and G. Hirth (2006) Grain size sensitive deformation mechanisms in naturally deformed peridotites, *Earth and Planetary Science Letters*, **248**, pp. 438-450
- Watson, E. B., J.M. Brenan, and D.R. Baker (1991) Distribution of fluids in the continental mantle, in *Continental Mantle*, ed.M. Menzies, Oxford Univ. Press, Oxford, pp. 111–125
- Wirth, R. (1996) Thin amorphous films (1-2 nm) at olivine grain boundaries in mantle xenoliths from San Carlos, Arizona, *Contributions to Mineralogy and Petrology*, **124**, pp. 44-54
- Wolf, D. (2001) High-temperature structure and properties of grain boundaries: long-range vs. short-range structural effects, *Current Opinions in Solid State and Materials Science*, **5**, pp. 435-443
- Yoshida, H. and T. Sakuma (1998) Transient creep associated with grain boundary sliding in fine-grained single-phase Al₂O₃, *Journal of Materials Science*, **33**, pp. 4879-4885
- Yoshida, H., S. Hashimoto, and T. Yamamoto (2005) Dopant effect on grain boundary diffusivity in polycrystalline alumina, *Acta Materialia*, **53**, pp. 433-440
- Yoshida, H., Y. Ikuhara, and T. Sakuma (2001) Transient creep in fine-grained polycrystalline Al₂O₃ with Lu³⁺ ion segregation at the grain boundaries, *Journal of Materials Research*, **16**, pp. 716-720
- Yoshino, T., M. Laumonier, E. Mclsaac, and T. Katsura (2010) Electrical conductivity of basaltic and carbonatite melt-bearing peridotites at high pressures: Implications for melt distribution and melt fraction in the upper mantle, *Earth and Planetary Science Letters*, **295**, pp. 593-602
- Yoshino, T., Y. Nishihara, and S. Karato (2007) Complete wetting of olivine grain boundaries by a hydrous melt near the mantle transition zone, *Earth and Planetary Science Letters*, **256**, pp. 466-472
- Yoshino, T., Y. Takei, D. A. Wark, and E. B. Watson (2005), Grain boundary wetness of texturally equilibrated rocks, with implications for seismic properties of the upper mantle, *Journal of Geophysical Research*, **110**, B08205, doi:10.1029/2004JB003544
- Zhao, Y-H., M.E. Zimmerman, and D.L. Kohlstedt (2009) Effect of iron content on the creep behavior of olivine: 1. Anhydrous conditions, *Earth and Planetary Science Letters*, **287**, pp. 229-240
- Zimmerman, M.E. and D.L. Kohlstedt (2004) Rheological Properties of Partially Molten Lherzolite, *Journal of Petrology*, **45**, pp. 275-298